

# Quantum random walks in waveguide lattices

Dissertation

zur Erlangung des akademischen Grades  
*doctor rerum naturalium* (Dr. rer. nat.)

vorgelegt dem Rat der Physikalisch-Astronomischen Fakultät  
der Friedrich-Schiller-Universität Jena

von Dipl. Phys. Robert Keil,  
geboren am 25.07.1984 in Jena



1. Gutachter: Prof. Dr. rer. nat. Stefan Nolte, Friedrich-Schiller-Universität Jena
2. Gutachter: Prof. Dr. rer. nat. Carsten Rockstuhl, Friedrich-Schiller-Universität Jena
3. Gutachter: Prof. Dr. Michael Withford, Macquarie University, Sydney, Australien

Tag der Disputation: 10. September 2013



# Contents

|          |  |           |
|----------|--|-----------|
| <b>1</b> | <b>Introduction</b>  | <b>3</b>  |
| <b>2</b> | <b>Fundamentals</b>  | <b>7</b>  |
| 2.1      | Field quantisation in a waveguide . . . . .                          | 7         |
| 2.1.1    | Hamiltonian of the electromagnetic field . . . . .                   | 7         |
| 2.1.2    | Quantisation of the oscillator . . . . .                             | 9         |
| 2.2      | Non-classical light evolution in waveguide lattices . . . . .        | 11        |
| 2.2.1    | Coupled waveguide lattices . . . . .                                 | 11        |
| 2.2.2    | Quantum path interference - The Hong-Ou-Mandel effect . . . . .      | 14        |
| 2.2.3    | Photon pairs in waveguide lattices . . . . .                         | 16        |
| 2.3      | Waveguide inscription . . . . .                                      | 20        |
| 2.4      | Generation and detection of indistinguishable photon pairs . . . . . | 23        |
| <b>3</b> | <b>Classical Characterisation of Quantum Interference</b>            | <b>26</b> |
| 3.1      | Photon pairs in a product state . . . . .                            | 26        |
| 3.2      | Photon pairs in an entangled state . . . . .                         | 31        |
| <b>4</b> | <b>Quantum random walk in two lateral dimensions</b>                 | <b>35</b> |
| 4.1      | Photon correlations in intersecting waveguide arrays . . . . .       | 35        |
| 4.2      | Direct measurement on a photonic chip . . . . .                      | 40        |
| 4.2.1    | Lattice interfacing and polarisation control . . . . .               | 40        |
| 4.2.2    | Observation of a two-dimensional quantum walk . . . . .              | 44        |
| <b>5</b> | <b>Glauber-Fock lattices</b>   | <b>55</b> |
| 5.1      | Displaced Fock states and their classical emulator . . . . .         | 56        |
| 5.2      | Photon correlations without shift-invariance . . . . .               | 63        |
| <b>6</b> | <b>Entangled photons in disordered lattices</b>                      | <b>72</b> |
| 6.1      | Waveguide lattices with uniform coupling disorder . . . . .          | 74        |
| 6.2      | Anderson localisation of entangled photons . . . . .                 | 79        |

|   |            |
|---|------------|
| <b>7 Conclusion and Outlook</b>                       | <b>88</b>  |
| <b>References</b>                                     | <b>93</b>  |
| <b>A Appendix</b>                                     | <b>105</b> |
| A.1 Derivation of the intensity correlation . . . . . | 105        |
| A.2 Inequality for distinguishable photons . . . . .  | 106        |
| <b>Acknowledgements</b>                               | <b>108</b> |
| <b>Zusammenfassung</b>                                | <b>110</b> |
| <b>Ehrenwörtliche Erklärung</b>                       | <b>111</b> |
| <b>Lebenslauf</b>                                     | <b>112</b> |

# 1 Introduction

In his seminal work of 1905, Albert Einstein provided a thermodynamic explanation for the random motion of microscopic particles dispersed in a fluid [1], which had been independently observed by Jan Ingenhousz<sup>1</sup> in 1785 and the botanist Robert Brown in 1827 [2]. Einstein was able to show that randomly impinging molecules of the fluid drive the motion of the particles, which depart from their initial position and follow a random trajectory. The associated Gaussian probability distribution of the particle position has a standard deviation broadening with the square root of evolution time. This phenomenon of diffusion is a prototype of a classical random walk. Such processes are ubiquitous in natural and man-made environments with examples ranging from the path of foraging animals [3] and population statistics of species [4] to fluctuations in commodity prices [5,6] - underlying potentially more complex probability distributions. A common feature of all classical random walks is that they are in principle deterministic processes, meaning that if all parameters driving the process were determined, the exact trajectory would be known.

A fundamentally different behaviour arises in the realm of quantum mechanics. As long as no measurement is conducted, the exact position of a single quantum is unknown. Instead, according to the prevalent Kopenhagen interpretation, its wavefunction evolves coherently over time, occupying a superposition of all possible locations. This leads to the notion of a quantum random walk (QRW), in which the ‘quantum walker’ simultaneously undergoes a superposition of multiple trajectories. This concept is equally applicable for a series of discrete time steps [7] as well as a continuous-time evolution [8]. The inherent indeterminism of quantum mechanics has a tremendous impact on the motion of the particles. For example, the probability distribution of a single particle subjected to an isotropic, stationary and homogeneous QRW on a line expands linearly in time, much faster than in the classical Brownian motion scenario [9,10].

QRWs are known to govern many natural as well as artificial transport processes, such as the energy transport in photosynthetic complexes [11] or spin-excitation transfer in ferromagnets [12,13]. Moreover, they are considered as universal for quantum computa-

---

<sup>1</sup>a Dutch physician better known for the discovery of photosynthesis

tion, meaning that any envisioned task of a quantum computer can be equally solved by a QRW [14].

There exists a large number of physical implementations of single-particle QRWs on a variety of platforms, including nuclear magnetic resonance [15,16], trapped neutral atoms [17] or ions [18,19] as well as photons in fiber loops [20] or cascades of spatial beam displacers [21]. As the probability amplitude of a single particle evolves according to wave mechanics, it is naturally also possible to perform a single particle QRW with classical light waves [22]. In fact, the very first QRW was implemented on coupled frequency modes of laser light in a resonator [23]. More recent classical realisations employed beam splitter cascades [24] or coupled waveguide lattices [25].

In particular the latter system offers many beneficial properties for the observation of continuous-time QRWs. A waveguide lattice is a discrete set of single-mode optical waveguides which are mutually coupled via their evanescent fields<sup>2</sup> [26–28]. Each waveguide represents a possible state of the quantum walker and its guided light amplitude corresponds to the probability amplitude of the walker occupying that state. The temporal evolution of the walker is mapped to the spatial propagation of the light. Hence, the QRW can be investigated in a static setting, with the possibility to freely control the ‘time scale’ of the walk by an appropriate choice of the lattice parameters. Light in waveguides is intrinsically insensitive to environmental influences and alignment issues, thus coherence can be maintained over large length scales as required for the multi-path interferences driving the QRW. Moreover, as no collapse of the wavefunction occurs for classical light, the intensity can be monitored throughout the entire evolution process in a single experiment [29]. Finally, a high degree of control over the lattice properties can be achieved by several established fabrication techniques [30–35].

The classical wave regime is left behind, however, as soon as multiple particles are involved. Moreover, in absence of additional degrees of freedom allowing for a distinction of the particles, their exchange symmetry will inevitably start to play a role. The QRW of two indistinguishable photons in a one-dimensional (1D) uniform, nearest-neighbour coupled lattice of waveguides was first proposed in 2009 [36] and experimentally realised shortly thereafter [37]. Due to their bosonic exchange statistics, the two photons do not evolve independently. Instead, all the possible paths the pair may take interfere with each other. This quantum path interference causes the positions of the particles to be mutually

---

<sup>2</sup>Here, the term ‘lattice’ implies merely discreteness; it is commonly used for periodic as well as aperiodic waveguide configurations.



---

correlated. Such correlated QRWs span a Hilbert space which grows exponentially with the number of quanta [37,38]. Therefore, the intricate correlations of a photon pair could, in principle, be exploited for resource-efficient quantum information processing, encoding much more information per photon than single photon schemes.

If one scales the dimensions of the state space beyond the case of a pair on a uniform 1D-graph, the potential of the system for quantum information applications will be even further enhanced. The most obvious way to achieve this is to increase the number of photons in the system. However, the controlled generation of multiphoton states faces considerable practical challenges due to the limited scalability of the photon sources. Currently, the record is held by an eight-photon state, implemented by tremendous experimental effort [39].

An alternative route is the extension of the waveguide lattice towards more complex graphs, offering larger Hilbert spaces with the same amount of photons. One can either investigate 1D arrays with non-uniform properties, thus establishing the transverse position as a degree of freedom, or turn to two-dimensional (2D) networks. The idea behind the latter option is that  $M$  indistinguishable particles in a 1D lattice involve the same complexity as a single-particle in  $M$  spatial dimensions [38]. Conversely, two spatial dimensions provide the same complexity as the twofold number of walkers in a single dimension [40–42].

While these approaches mitigate the need for more than two photons, they bring about new challenges on their own. Most importantly, one requires a fabrication technique which is capable to precisely assemble waveguides in up to two spatial dimensions in a permanent fashion. The direct waveguide inscription in transparent materials by ultra-short laser pulses [32,33] has developed into a rather mature technology which offers these capabilities. The feasibility of laser-written evanescently coupled waveguides for quantum path interferences [43–49] and even 1D QRWs [50,51] has been demonstrated in several experiments over the last years. Therefore, the laser waveguide inscription lends itself as the method of choice.

The second challenge is that the performance of the waveguide systems should be characterised after the fabrication step with as little effort as possible. However, running an actual correlated QRW on a large lattice is not a trivial endeavour, as a multitude of waveguide channels has to be interfaced with photon sources and detection devices, and a certain measurement time is needed in order to obtain sufficient photon counting statistics [37]. Therefore, a classical characterisation technique which allows to catch the essential features of the expected QRW seems highly desirable. Indeed, such a technique

has been employed in the original correlated QRW proposal, albeit with a certain bias in the estimation of the photon correlations [36].

In this thesis, several possible strategies towards QRWs with increased complexities are pursued. To this end, 1D waveguide lattices with spatially dependent coupling properties as well as 2D networks are devised. Correlated QRWs of indistinguishable photon pairs in these structures are investigated via numerical calculations and their experimental implementations performed in cooperation with the Universities of Bristol and Central Florida are presented. Moreover, a novel characterisation technique is developed and applied, which simulates the photon correlations with classical light in an unbiased fashion, thereby overcoming the above mentioned challenge.

Following a recapitulation of the theoretical foundations for the evolution of photon pairs in waveguide lattices, the laser inscription technique as well as the technologies required for photon generation and detection in chapter 2, the achievements of this work are presented in four main chapters. Chapter 3 introduces the classical characterisation technique which is subsequently employed in other parts of this thesis. The fourth chapter presents the investigation of QRWs in a 2D waveguide lattice, whereas the two remaining chapters treat 1D systems beyond the uniform configuration. Chapter 5 covers so-called Glauber-Fock lattices with a judiciously engineered coupling distribution and the final chapter deals with disordered lattices entailing a random variation of the coupling across the lattice. The thesis concludes with a brief summary of the results and an outlook to further developments in the field.

# 2 Fundamentals

## 2.1 Field quantisation in a waveguide

If optics enters the regime of single quanta, the electromagnetic field can no longer be treated classically. In this section it will be reiterated how the quantisation of an electromagnetic field arises via the equivalence of the classical field-Hamiltonian and the Hamiltonian of a classical harmonic oscillator. Along these lines, it is shown how the real and imaginary parts of the quantised electric field translate into the position and momentum operator of the quantised oscillator and how the oscillator eigenstates count the number of photons in the field.

In the literature this derivation is usually presented in the context of plane waves propagating in free space [52–55]. However, as this work is concerned with light guided in single-mode optical waveguides, this approach will be adopted for the field quantisation in an isolated single-mode waveguide and then later generalised to a system of several weakly coupled waveguides.

### 2.1.1 Hamiltonian of the electromagnetic field

The first step towards a quantum description of the light field is the determination of the Hamiltonian for a classical electromagnetic field in a waveguide. The starting point are Maxwell's equations in the frequency domain for source-free electric and magnetic fields  $\mathbf{E}(\mathbf{r}, \omega)$  and  $\mathbf{B}(\mathbf{r}, \omega)$  in an isotropic dielectric medium with permittivity  $\epsilon(\mathbf{r}, \omega)$  [56]:

$$\nabla \times \mathbf{E}(\mathbf{r}, \omega) = i\omega \mathbf{B}(\mathbf{r}, \omega) \quad (2.1a)$$

$$\nabla \times \mathbf{B}(\mathbf{r}, \omega) = -i\frac{\omega}{c^2} \mathbf{E}(\mathbf{r}, \omega) \quad (2.1b)$$

$$\nabla \cdot \mathbf{B}(\mathbf{r}, \omega) = 0 \quad (2.1c)$$

$$\nabla \cdot [\epsilon(\mathbf{r}, \omega) \mathbf{E}(\mathbf{r}, \omega)] = 0, \quad (2.1d)$$

with angular frequency  $\omega$  and  $c = (\epsilon_0 \mu_0)^{-\frac{1}{2}}$  denoting the speed of light. In the course of this work, only monochromatic fields will be of interest. For convenience, the argument

$\omega$  is henceforth omitted in all functions. Nevertheless, the following derivation of the classical Hamiltonian will be equally valid for arbitrary spectra.

A dielectric waveguide has a permittivity profile which depends on the transverse coordinates  $(x, y)$ , but is invariant along the longitudinal direction  $z$ :  $\epsilon(\mathbf{r}) = \epsilon + \Delta\epsilon(x, y)$ ,  $\epsilon$  denoting the permittivity of the surrounding bulk material. It is assumed that the waveguide is weakly guiding, i.e., it has a shallow profile  $\Delta\epsilon(x, y) \ll \epsilon$ .<sup>1</sup> Then the Eqs. (2.1a), (2.1b) and (2.1d) can be combined to the Helmholtz equation for the electric field:

$$\left[ \nabla^2 + \frac{\omega^2}{c^2} \epsilon(x, y) \right] \mathbf{E}(\mathbf{r}) = 0. \quad (2.2)$$

A second assumption is that the waveguide is so weakly guiding that it supports only one bound mode with eigenvalue  $\gamma$  as solution of Eq. (2.2):

$$\mathbf{E}(\mathbf{r}) = E_0(x, y) e^{i\gamma z} \mathbf{e}(x, y), \quad (2.3)$$

with transverse amplitude  $E_0(x, y)$  and a normalised polarisation vector  $\mathbf{e} \cdot \mathbf{e} = 1$ . For weak guiding the transverse components of this mode are dominating<sup>2</sup>, i.e.,  $\mathbf{e} \cdot \mathbf{e}_z \approx 0$ . In the following,  $\gamma$  will always be treated as a real number, i.e., the waveguide is assumed to be passive and lossless. The associated magnetic field follows from Eq. (2.1a) and is also primarily oriented in a transverse direction:

$$\mathbf{B}(\mathbf{r}) = \frac{\gamma}{\omega} E_0(x, y) e^{i\gamma z} \mathbf{e}(x, y) \times \mathbf{e}_z. \quad (2.4)$$

To calculate the total energy contained in the electromagnetic field one requires the real parts of the fields  $\mathbf{E}_r = \frac{1}{2}(\mathbf{E} + \text{c.c.})$  and  $\mathbf{B}_r = \frac{1}{2}(\mathbf{B} + \text{c.c.})$ :

$$\begin{aligned} H &= \frac{1}{2} \int d^3\mathbf{r} \left[ \epsilon_0 \epsilon(x, y) \mathbf{E}_r(\mathbf{r}) \cdot \mathbf{E}_r(\mathbf{r}) + \frac{1}{\mu_0} \mathbf{B}_r(\mathbf{r}) \cdot \mathbf{B}_r(\mathbf{r}) \right] \\ &= \frac{1}{8} \int d^3\mathbf{r} \left\{ \epsilon_0 \epsilon(x, y) [\mathbf{E}(\mathbf{r}) + \text{c.c.}]^2 + \frac{1}{\mu_0} [\mathbf{B}(\mathbf{r}) + \text{c.c.}]^2 \right\}. \end{aligned}$$

Substituting with Eqs. (2.3) and (2.4) yields:

$$H = \frac{1}{8} \int d^3\mathbf{r} \left[ \epsilon_0 \epsilon(x, y) \mathbf{e} \cdot \mathbf{e} + \frac{\gamma^2}{\mu_0 \omega^2} (\mathbf{e} \times \mathbf{e}_z)^2 \right] [E_0(x, y) e^{i\gamma z} + \text{c.c.}]^2.$$

---

<sup>1</sup>More strictly speaking, the condition is  $|\nabla\epsilon(x, y)| \ll \lambda^{-1}\epsilon(x, y)$ , with  $\lambda = 2\pi c\omega^{-1}$  as the wavelength of the field. If this condition is met,  $\nabla \cdot \mathbf{E} \approx 0$  will follow from Eq. (2.1d). See Fig. 2.1(a) for a typical permittivity profile.

<sup>2</sup>As  $|\frac{\partial\mathbf{E}}{\partial z}| = \gamma|\mathbf{E}| \gg |\frac{\partial\mathbf{E}}{\partial x}|, |\frac{\partial\mathbf{E}}{\partial y}|$  for weakly guided modes (see again Fig. 2.1(a) for a typical example), the condition  $\nabla \cdot \mathbf{E} \approx 0$  can only be satisfied for  $|E_z| \ll |E_x|, |E_y|$ .

The scalar products of the polarisation vectors are unity  $\mathbf{e} \cdot \mathbf{e} = (\mathbf{e} \times \mathbf{e}_z)^2 = 1$  and the permittivity profile can be treated as nearly constant within the integral  $\epsilon(x, y) \approx \epsilon$ . Furthermore, the transverse electric field amplitude can be decomposed into its real and imaginary parts:

$$E_0(x, y) \equiv \omega q(x, y) + ip(x, y). \quad (2.5)$$

With that one obtains for the Hamiltonian:

$$H = \frac{1}{8} \left( \epsilon_0 \epsilon + \frac{\gamma^2}{\mu_0 \omega^2} \right) \int d^3 \mathbf{r} \{ [\omega q(x, y) + ip(x, y)] e^{i\gamma z} + \text{c.c.} \}^2.$$

All rapidly oscillating terms vanish upon longitudinal integration:  $\int dz e^{\pm 2i\gamma z} = 0$ . Moreover, the eigenvalue of the weakly guided mode can be approximated with the wavenumber in the bulk medium  $\gamma \approx \frac{\omega}{c} \sqrt{\epsilon}$ , so one ends up with:

$$H = \frac{\epsilon_0 \epsilon L}{2} \iint dx dy [\omega^2 q^2(x, y) + p^2(x, y)],$$

with  $L$  denoting the length of the waveguide. Finally, the introduction of the integrals of the transverse fields  $Q^2 \equiv \sqrt{\epsilon_0 \epsilon L} \iint dx dy q^2(x, y)$  and  $P^2 \equiv \sqrt{\epsilon_0 \epsilon L} \iint dx dy p^2(x, y)$  yields

$$H = \frac{1}{2} (\omega^2 Q^2 + P^2), \quad (2.6)$$

revealing the formal correspondence to the Hamiltonian of a classical harmonic oscillator with conjugated position and momentum variables  $Q$  and  $P$ , unit mass and frequency  $\omega$ .

### 2.1.2 Quantisation of the oscillator

Now one can proceed entirely analogous to the quantisation of a harmonic oscillator. The conjugated variables are replaced by operators  $\hat{Q}$  and  $\hat{P}$ , required to satisfy the commutation relation

$$[\hat{Q}, \hat{P}] = i\hbar. \quad (2.7)$$

It is convenient to introduce the ladder operators [52]:

$$\begin{aligned} \hat{a} &\equiv \sqrt{\frac{1}{2\hbar\omega}} (\omega\hat{Q} + i\hat{P}) \\ \hat{a}^\dagger &\equiv \sqrt{\frac{1}{2\hbar\omega}} (\omega\hat{Q} - i\hat{P}), \end{aligned} \quad (2.8)$$

which according to (2.7) satisfy the commutator relation:

$$[\hat{a}, \hat{a}^\dagger] = 1. \quad (2.9)$$

From a comparison of Eqs. (2.5) and (2.8) it is evident that the operator  $\hat{a}$  is essentially the operator of the electric field. This will be an important notion in chapter 5. With the ladder operators the Hamiltonian (2.6) becomes for the quantised field:

$$\hat{H} = \hbar\omega \left( \hat{a}^\dagger \hat{a} + \frac{1}{2} \right). \quad (2.10)$$

This Hamiltonian has a semi-infinite set of eigenstates  $\{|n\rangle\}_{n=0}^\infty$ , so-called number states or Fock states [57], which have an equidistant energy spectrum separated by integer multiples of  $\hbar\omega$ :

$$\hat{H} |n\rangle = \hbar\omega \left( \hat{a}^\dagger \hat{a} + \frac{1}{2} \right) |n\rangle = \hbar\omega \left( n + \frac{1}{2} \right) |n\rangle.$$

As Einstein reasoned in another of his *annus mirabilis* publications, the light field is composed of single quanta [58] - termed photons - of energy  $\hbar\omega$ . With this in mind, the following interpretation is apparent: The Fock state  $|n\rangle$  has  $n$  quanta in the waveguide mode and the number operator  $\hat{n} = \hat{a}^\dagger \hat{a}$  counts this number. The ladder operators  $\hat{a}$  and  $\hat{a}^\dagger$  are also referred to as annihilation and creation operator, respectively, as their action on an eigenstate literally destroys or generates a photon:

$$\begin{aligned} \hat{a} |n\rangle &= \sqrt{n} |n-1\rangle \\ \hat{a}^\dagger |n\rangle &= \sqrt{n+1} |n+1\rangle. \end{aligned} \quad (2.11)$$

The ground state  $|0\rangle$  containing no photons is referred to as the vacuum state. Fig. 2.1**(b)** illustrates the eigenstates of the oscillator, their equidistant energy spectrum and the action of the ladder operators.

Note that the quantisation demonstrated in this section can be applied to a multi-mode and/or polychromatic field in the same way. One merely has to consider a set of operators  $\hat{a}_k$  and propagation constants  $\gamma_k = \frac{\omega_k}{c} \sqrt{\epsilon}$  for the components and express the Hamiltonian as a sum or integral of the single-mode contributions [53,55]. Such a multi-mode extension can also be made for a system with several single-mode guides, which is what will be used in the next section.

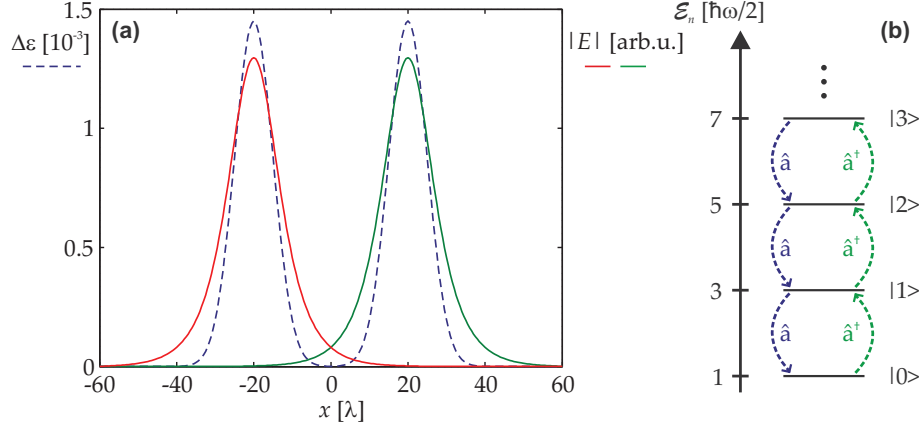


**Figure 2.1:** (a) Cross-section through a Gaussian permittivity profile (blue dashed line) of 2 weakly guiding waveguides with a width (standard deviation of the Gaussian) of 5 wavelengths  $\lambda$  and a separation of  $40\lambda$ . The red and green solid lines show the numerically calculated field magnitudes of these single-mode guides. The bulk permittivity is  $\epsilon = 2.1$  as in fused silica. (b) Energy ladder  $\mathcal{E}_n$  of the oscillator eigenstates and their response to the operators  $\hat{a}^{(\dagger)}$ .

## 2.2 Non-classical light evolution in waveguide lattices

Now a system of  $N$  single mode waveguides is considered. In the first part of this section, the Hamiltonian of the general system and the Heisenberg equation of motion governing its evolution are introduced. This is followed by a solution of the special case  $N = 2$ , leading to the famous Hong-Ou-Mandel effect and the associated quantum path interference [59], which is at the origin for the correlated behaviour of multi-particle QRWs. In the final part, the formal expressions for the relevant observables of two-photon QRWs in arbitrary lattices are presented and illustrated by the pertinent example of a uniform 1D array.

### 2.2.1 Coupled waveguide lattices

The total Hamiltonian of the multi-waveguide system will be the sum of the Hamiltonians (2.10) of the individual guides. In general the waveguides can be different from one another, supporting modes with different propagation constants  $\gamma_k$ . The total Hamiltonian can then be written as:

$$\hat{H} = \hbar \sum_{k=1}^N \omega_k \left( \hat{a}_k^\dagger \hat{a}_k + \frac{1}{2} \right) = \frac{\hbar c}{n_0} \sum_{k=1}^N \gamma_k \left( \hat{a}_k^\dagger \hat{a}_k + \frac{1}{2} \right),$$

with  $n_0 = \sqrt{\epsilon}$  denoting the refractive index of the surrounding bulk medium. This Hamiltonian describes a set of waveguides which are isolated or infinitely far away from each other. However, each waveguide supports one mode with a transverse field, decaying exponentially away from its centre. So in a system with finite extension, these exponential

tails overlap to a certain degree with the other waveguides (see Fig. 2.1(a) for an example of two identical guides). In the tight-binding or coupled-mode approximation [26, 60] one assumes that this overlap is small enough not to distort the profiles and the propagation constants of the individual modes. If this approximation holds the waveguide modes get pairwise coupled and the Hamiltonian of the system becomes [61, 62]:

$$\hat{H} = \frac{\hbar c}{n_0} \sum_{k=1}^N \left[ \gamma_k \left( \hat{a}_k^\dagger \hat{a}_k + \frac{1}{2} \right) + \sum_{l=1}^N C_{k,l} \hat{a}_k^\dagger \hat{a}_l \right]. \quad (2.12)$$

The coupling strength between the mode fields  $E_{0,k}$  and  $E_{0,l}$  of guides  $k$  and  $l$  is

$$C_{k,l} \propto \iint dx dy E_{0,k}(x, y) E_{0,l}^*(x, y) [\Delta\epsilon(x, y) - \Delta\epsilon_l(x, y)], \quad (2.13)$$

with  $\Delta\epsilon_l$  denoting the permittivity profile of guide  $l$  [26, 63–65]. Note that in the tight-binding limit the evanescent coupling strength is always real and obeys the generic symmetry  $C_{k,l} = C_{l,k}$  [64]. Therefore, the Hamiltonian (2.12) is always Hermitian.

The field operators of one and the same mode obey the commutator relation (2.9), whereas they commute among different modes:

$$[\hat{a}_k, \hat{a}_l^\dagger] = \delta_{k,l}. \quad (2.14)$$

Of course also

$$[\hat{a}_k, \hat{a}_l] = [\hat{a}_k^\dagger, \hat{a}_l^\dagger] = 0 \quad (2.15)$$

holds for all  $k$  and  $l$ .

The number of photons in the waveguides is now tracked by the Fock states  $|n_1, \dots, n_N\rangle$ , with  $n_k$  as the photon number in guide  $k$ , obeying:

$$\begin{aligned} \hat{a}_k |n_1, \dots, n_k, \dots, n_N\rangle &= \sqrt{n_k} |n_1, \dots, n_k - 1, \dots, n_N\rangle \\ \hat{a}_k^\dagger |n_1, \dots, n_k, \dots, n_N\rangle &= \sqrt{n_k + 1} |n_1, \dots, n_k + 1, \dots, n_N\rangle. \end{aligned} \quad (2.16)$$

In this notation all photons are assumed to be indistinguishable from each other<sup>3</sup>. The Fock states are orthogonal, satisfying

$$\langle n_1, \dots, n_N | m_1, \dots, m_N \rangle = \delta_{n_1, m_1} \dots \delta_{n_N, m_N}.$$

---

<sup>3</sup>Indistinguishability means that there is no physical quantity besides their spatial position in which the photons differ, so in particular they must have the same frequency, polarisation and overlap temporally. In this work indistinguishability is always assumed if not stated otherwise.



The evolution of the system is best described in the Heisenberg picture, where the states remain invariant, but the operators  $\hat{a}_k^{(\dagger)}$  evolve. This evolution is governed by the Heisenberg equation

$$i\hbar \frac{d}{dt} \hat{a}_m^\dagger = i \frac{\hbar c}{n_0} \frac{d}{dz} \hat{a}_m^\dagger = [\hat{a}_m^\dagger, \hat{H}],$$

where instead of a temporal evolution, a propagation along the longitudinal coordinate  $z$ , being related to  $t$  by the phase velocity  $\frac{c}{n_0}$ , is considered [36]. Evaluating this commutator for the Hamiltonian (2.12) and using the commutators (2.14),(2.15) yields the equations of motion for the creation operators:

$$i \frac{d}{dz} \hat{a}_m^\dagger(z) + \gamma_m \hat{a}_m^\dagger(z) + \sum_{k=1}^N C_{k,m} \hat{a}_k^\dagger(z) = 0.$$

The adjoint operators  $\hat{a}_m(z)$  can be obtained from complex conjugation.

Usually, the waveguides have very similar propagation constants  $\gamma_m = \gamma_0 + \beta_m$ , with the average value  $\gamma_0$ . It is therefore convenient to switch to a reference frame which is co-propagating with  $\gamma_0$ , thereby separating rapid phase oscillations from the coupling dynamics. One can further introduce  $\hat{b}_k^\dagger \equiv \hat{a}_k^\dagger e^{-i\gamma_0 z}$  and absorb the detunings  $\beta_m$  into the coupling matrix  $\tilde{C}_{k,l} \equiv \beta_k \delta_{k,l} + C_{k,l}$  to obtain:

$$i \frac{d}{dz} \hat{b}_m^\dagger(z) + \sum_{k=1}^N \tilde{C}_{k,m} \hat{b}_k^\dagger(z) = 0. \quad (2.17)$$

These will be the equations of motion to be solved for all problems this work is concerned with. The properties of the system, which can be an arbitrary arrangement of single-mode tight-binding waveguides, are always encoded in the coupling matrix  $\tilde{C}$ .

Note that the assumption about passive and lossless waveguides made earlier is crucial to conserve the commutator (2.14). However, due to the transformation to the moving frame, any *global* loss (i.e., a positive imaginary part of  $\gamma_0$ ) is compensated by the choice of the operators  $\hat{b}_k^{(\dagger)}$  which still satisfy  $[\hat{b}_k, \hat{b}_l^\dagger] = \delta_{k,l}$ . Hence, global losses have no impact on the evolution dynamics and can, in principle, be removed by normalisation. This will be a useful property in context of the propagation losses in laser-written waveguide lattices (see chapter 2.3). A formal treatment of non-uniform loss distributions is possible [66], but beyond the scope of this work.

For most problems it will be important to determine the expectation value of the photon number distribution, i.e., the average photon number in the individual channels, at a

given position  $z$ :

$$\bar{n}_k(z) \equiv \langle \hat{n}_k(z) \rangle = \left\langle \hat{b}_k^\dagger(z) \hat{b}_k(z) \right\rangle \quad (2.18)$$

for all  $k = 1, \dots, N$ . Here  $\langle \cdot \rangle$  denotes the expectation value of an operator with respect to the state of the system.

If more than one identical photon is present in the system at a time the two-photon-correlation function [36]

$$\Gamma_{k,l}(z) \equiv \left\langle \hat{b}_k^\dagger(z) \hat{b}_l^\dagger(z) \hat{b}_l(z) \hat{b}_k(z) \right\rangle \quad (2.19)$$

is another important quantity, as it relates to the joint probability of finding one photon in guide  $k$  and one in  $l$  at the same time via  $P_{k,l} = \frac{1}{1+\delta_{k,l}} \Gamma_{k,l}$ . Note that  $\Gamma_{k,l} = \Gamma_{l,k}$  follows directly from (2.15). These correlations will be highly non-trivial for indistinguishable photons as soon as several paths lead to the same result. A quantum path interference will occur as will be illustrated by a simple example in the next section.

## 2.2.2 Quantum path interference - The Hong-Ou-Mandel effect

The most basic coupled waveguide system consists of two identical waveguides coupled with strength  $C_{1,2} = C$ . For such a directional coupler the equations of motion (2.17) can be analytically solved:

$$\hat{b}_{1/2}^\dagger(z) = \hat{b}_{1/2}^\dagger(0) \cos(Cz) + i\hat{b}_{2/1}^\dagger(0) \sin(Cz). \quad (2.20)$$

For convenience, the argument (0) for the operators at the input of the lattice will from now on always be omitted.

For a single photon input to channel 1:

$$|\Psi_1\rangle \equiv \hat{b}_1^\dagger |0, 0\rangle = |1, 0\rangle,$$

one finds for the average photon number (2.18) in that waveguide:

$$\begin{aligned} \bar{n}_1(z) &= \left\langle \left[ \hat{b}_1^\dagger \cos(Cz) + i\hat{b}_2^\dagger \sin(Cz) \right] \left[ \hat{b}_1 \cos(Cz) - i\hat{b}_2 \sin(Cz) \right] \right\rangle \\ &= \left\langle \hat{b}_1^\dagger \hat{b}_1 \right\rangle \cos^2(Cz) + \left\langle \hat{b}_2^\dagger \hat{b}_2 \right\rangle \sin^2(Cz) + \left[ i \left\langle \hat{b}_2^\dagger \hat{b}_1 \right\rangle \cos(Cz) \sin(Cz) + \text{c.c.} \right] \\ &= \cos^2(Cz). \end{aligned}$$

In the last step it has been exploited that the annihilation of the vacuum state yields zero (cf. (2.16)), so that  $\left\langle \hat{b}_2^\dagger \hat{b}_2 \right\rangle = \langle 1, 0 | \hat{b}_2^\dagger \hat{b}_2 | 1, 0 \rangle = 0 = \left\langle \hat{b}_2^\dagger \hat{b}_1 \right\rangle$ . Similarly, one finds  $\bar{n}_2(z) = \sin^2(Cz) = 1 - \bar{n}_1(z)$ . So the photon probability distribution oscillates between

the two waveguides with period  $\frac{\pi}{C}$  (see Fig. 2.2(a)), just in the same way as classical light [26]. This does not come unexpected since the probability amplitude of a single photon evolves always as the light amplitude of a classical wave [67].

A particularly interesting case is the propagation over a quarter of a period  $z = \frac{\pi}{4C}$ , where the single photon has equal probabilities of  $\frac{1}{2}$  to occupy either waveguide at the output. From now on a coupler of this length is simply referred to as ‘50/50 coupler’. If two identical photons are launched simultaneously into the coupler, one in each channel, the input state is the product state:

$$|\Psi_{1,2}^{(p)}\rangle \equiv \hat{b}_1^\dagger \hat{b}_2^\dagger |0, 0\rangle = |1, 1\rangle.$$

The average photon number at the output of the 50/50 coupler is now  $\bar{n}_1\left(\frac{\pi}{4C}\right) = \bar{n}_2\left(\frac{\pi}{4C}\right) = 1$ , so on average one photon will be detected in each channel, as one might expect from the symmetry of the system. However, one finds for the correlation function (2.19) via (2.16) and the commutators (2.15) the interesting result:

$$\Gamma_{1,1}^{(p)}\left(\frac{\pi}{4C}\right) = \Gamma_{2,2}^{(p)}\left(\frac{\pi}{4C}\right) = 1; \quad \Gamma_{1,2}^{(p)}\left(\frac{\pi}{4C}\right) = 0.$$

This means that the probability for the two photons occurring together is  $P_{1,1} = P_{2,2} = \frac{1}{2}$  for each waveguide, but they *never* occur in different waveguides. This is a direct consequence of their indistinguishability as one cannot tell which photon went which way. More specifically, there are two possible paths which would lead to a coincident detection in channels 1 and 2: both photons could remain in their initial waveguide or they could swap sides. As there is a phase factor of  $i$  imposed upon the coupling (cf. (2.20)), these two paths interfere destructively. Hence, the output state is no longer a product state of the type (2.16), but the path-entangled state [53, 68, 69]

$$|\Psi_{\text{out}}\rangle = \frac{i}{2} (|2, 0\rangle + |0, 2\rangle). \quad (2.21)$$

This is a representative of the important  $N00N$  states which are the  $N$ -photon states with a maximal degree of entanglement [70].

Such a quantum path interference stands in stark contrast to the behaviour of classical or distinguishable particles. If the two photons were distinguishable, they would just propagate independently from another, obeying binomial statistics and resulting in the output correlations [71]:  $\Gamma_{1,1}^{(d)}\left(\frac{\pi}{4C}\right) = \Gamma_{2,2}^{(d)}\left(\frac{\pi}{4C}\right) = \Gamma_{1,2}^{(d)}\left(\frac{\pi}{4C}\right) = 0.5$ , with equal probabilities for the photons to leave the coupler together or in different waveguides.

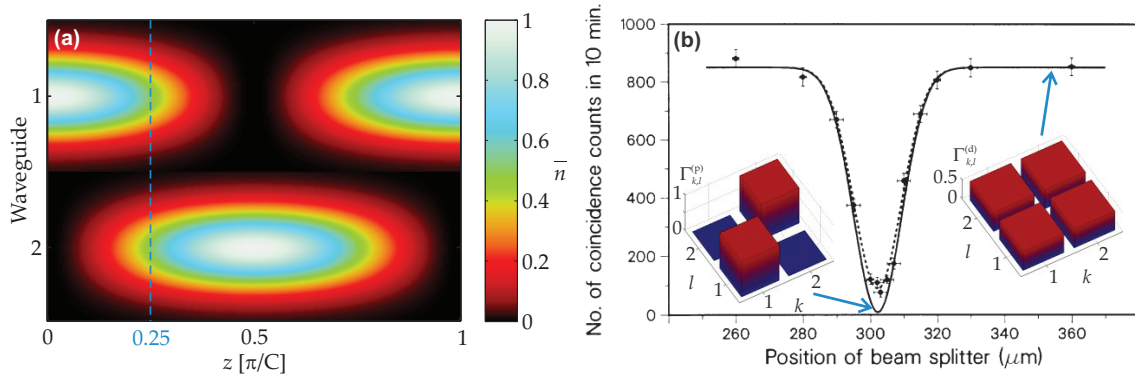


**Figure 2.2:** (a) Evolution of the average photon number in a directional coupler for a single photon launched into guide 1. The dashed line indicates the propagation distance at which the device acts as a 50/50 coupler. To illustrate the spatial distribution of the photons within a typical waveguide, the discrete values  $\bar{n}$  have been multiplied with a Gaussian mode profile. (b) The original Hong-Ou-Mandel dip from [59] for two photons launched into the input ports of a 50/50 beamsplitter. For distinguishable photons, coincidences between the two output ports occur, corresponding to non-vanishing off-diagonal entries in the correlation matrix (right inset). The left inset shows the correlation matrix for indistinguishable photons, where no coincidences occur.

The observation of quantum path interference was first made by Hong, Ou and Mandel in their landmark experiment on a balanced beamsplitter [59], which is the bulk-optic equivalent of a 50/50 coupler. They used pairs of identical photons with a wavepacket duration of about 100fs. Hence, when they made their wavepackets overlap in time, a nearly perfect destructive quantum interference could be measured in the coincidence rate (corresponding to  $\Gamma_{1,2}^{(p)}$ ), whereas a relative delay of the wavepackets made the photons distinguishable, preventing any quantum interference and therefore leading to a higher coincidence rate. The resulting curve, the famous Hong-Ou-Mandel-dip, is shown in Fig. 2.2(b), together with the correlation matrices for perfectly distinguishable and indistinguishable photons.

This quantum interference of indistinguishable photons is the key phenomenon for the understanding of this work. In the following chapters, the simple '50/50 coupler' will be replaced by gradually more complex arrangements of waveguides, offering an increased number of paths for the photon pair and, therefore, exhibiting more intricate correlation effects.

### 2.2.3 Photon pairs in waveguide lattices

Returning to the general lattice of  $N$  waveguides, as governed by Eq. (2.17), one finds that there is no analytic solution for this general case. Nevertheless, the evolution of the

operators can be formally expressed as the exponential of the coupling matrix:

$$\hat{b}_m^\dagger(z) = \sum_k U_{m,k}(z) \hat{b}_k^\dagger, \quad U_{m,k} \equiv \left( e^{iz\tilde{\mathcal{C}}} \right)_{m,k}. \quad (2.22)$$

Due to the symmetry of the coupling matrix,  $\mathbf{U}$  is always unitary<sup>4</sup>. By its definition,  $U_{m,k}(z)$  can also be interpreted as the probability amplitude for a photon injected in guide  $k$  to be detected in channel  $m$  after propagation over the distance  $z$ . This gets most evident when considering the single-photon input state on guide  $k$ :

$$|\Psi_k\rangle = \hat{b}_k^\dagger |\emptyset\rangle \equiv \hat{b}_k^\dagger |0, \dots, 0\rangle = |0, \dots, 1_{(k)}, \dots, 0\rangle,$$

with  $n_{(k)}$  denoting  $n$  photons in guide  $k$ . Its expected photon number distribution can be obtained by substituting (2.22) into (2.18):

$$\bar{n}_m(z) = |U_{m,k}(z)|^2. \quad (2.23)$$

As in the directional coupler, this is identical to the intensity distribution of a classical beam of light injected into site  $k$ .

There are two types of two-photon input states under investigation in this work. One is the product state of one photon being launched into waveguide  $k$ , the other in guide  $l$ , which has been encountered in the previous chapter:

$$\left| \Psi_{k,l}^{(p)} \right\rangle = \hat{b}_k^\dagger \hat{b}_l^\dagger |\emptyset\rangle \equiv \hat{b}_k^\dagger \hat{b}_l^\dagger |0, \dots, 0\rangle = |0, \dots, 1_{(k)}, \dots, 1_{(l)}, \dots, 0\rangle, \quad (2.24)$$

for  $k \neq l$ . The other interesting configuration is a path-entangled state with the photons being initiated together at *either* of the two waveguides, as it can be produced from a waveguide coupler (2.21), potentially involving a phase shift  $\phi$ :

$$\left| \Psi_{k,l}^{(e,\phi)} \right\rangle = \frac{1}{2} \left[ \left( \hat{b}_k^\dagger \right)^2 + e^{i\phi} \left( \hat{b}_l^\dagger \right)^2 \right] |\emptyset\rangle = \frac{1}{\sqrt{2}} \left( |0, \dots, 2_{(k)}, \dots, 0\rangle + e^{i\phi} |0, \dots, 2_{(l)}, \dots, 0\rangle \right), \quad (2.25)$$

again with  $k \neq l$ . The configuration  $k = l$ , corresponding to both photons being always initialised in a single waveguide, is rather trivial: As both photons start at the same position with identical evolution dynamics, no quantum path interference can arise and the photons will propagate independently from each other through the system.

For both types of two-photon input states one finds the following solution for the mean

---

<sup>4</sup>The numerical calculation of this matrix exponential is straightforwardly possible for systems of up to a few thousand waveguides.

photon number, again by substituting (2.22) into (2.18):

$$\bar{n}_m(z) = |U_{m,k}(z)|^2 + |U_{m,l}(z)|^2. \quad (2.26)$$

This is the incoherent sum of the average photon numbers for single photon inputs in channels  $k$  and  $l$  (see Eq. (2.23)). Hence, quantum path interference is never visible in the average photon number, regardless of the nature of the input state. In contrast, the correlation does depend on the input state and reveals this interference. One finds for the product state (2.24) [36]:

$$\Gamma_{m,n}^{(p)}(z) = |U_{m,k}(z)U_{n,l}(z) + U_{m,l}(z)U_{n,k}(z)|^2, \quad (2.27)$$

which clearly depends on the phases of  $U$  and can no longer be decomposed into single photon contributions. The correlation of the entangled state (2.25) yields [72]:

$$\Gamma_{m,n}^{(e,\phi)}(z) = |U_{m,k}(z)U_{n,k}(z) + e^{-i\phi}U_{m,l}(z)U_{n,l}(z)|^2. \quad (2.28)$$

To elucidate these quantities by an example, an infinite<sup>5</sup> one-dimensional (1D) lattice of identical waveguides ( $\beta_m = 0$ ) with uniform nearest-neighbour coupling  $C_{m-1,m} = C$  is now considered. As the directional coupler, this is a system which can be solved analytically. One finds that the evolution matrices are governed by Bessel functions of the first kind  $U_{m,k} = i^{m-k}J_{m-k}(2Cz)$  [26].

Fig. 2.3(a) shows the resulting mean photon number distribution for a single photon being launched into the central waveguide. One can clearly identify two ballistic lobes within which the photon is most likely to occur. These lobes are a characteristic feature of the discrete diffraction occurring in such a waveguide array [26–28]. Intriguingly, the evolution pattern spreads linearly upon propagation, just as expected for the probability distribution in a single-particle QRW [10]. As mentioned earlier, it turns out that the evolution of a single photon<sup>6</sup> in a waveguide array is a spatial implementation of a continuous-time QRW on a 1D graph [25].

From Eq. (2.26) one expects the average photon number for two photons to be merely the incoherent sum of the single photon excitations. Indeed, if two neighbouring channels are excited with any of the input states (2.24),(2.25), the two propagation patterns add

---

<sup>5</sup>Infinity means here that the physical array is so large, that the boundaries have no significant influence on the photon evolution.

<sup>6</sup>Or a classical beam of light, which exhibits the same dynamics

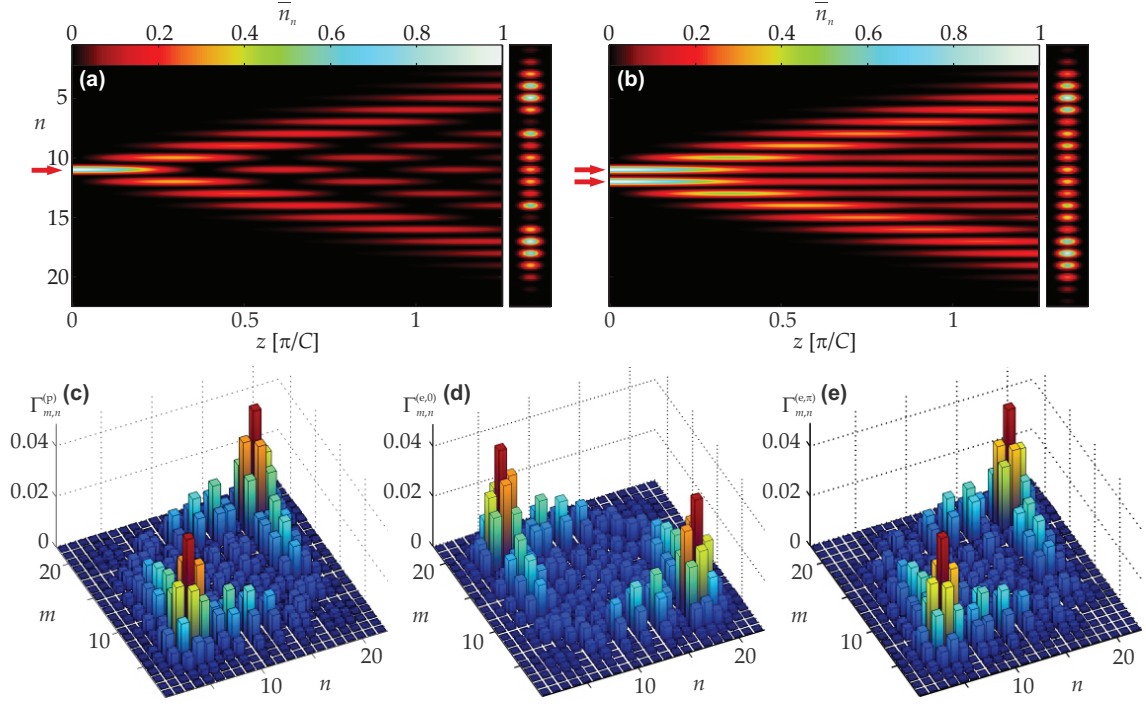


**Figure 2.3:** (a) Evolution and output distribution of the average photon number in a planar lattice of 22 waveguides and length  $1.25\pi/C$  for a single photon launched into the central guide no. 11. (b) Same as (a), but for two photons launched into the adjacent channels 11 and 12. The output images are normalised to their peak values and the red arrows indicate the input positions. (c) Correlation function for the product state  $|\Psi_{11,12}^{(p)}\rangle$ . (d),(e) Correlation functions for the entangled state  $|\Psi_{11,12}^{(e,\phi)}\rangle$  with (d)  $\phi = 0$  and (e)  $\phi = \pi$ .

incoherently (Fig. 2.3(b)).

However, the two-photon correlation for the product state at the output of the lattice exhibits a clear signature of quantum interference, as shown in Fig. 2.3(c): There are pronounced peaks on the main diagonal of the matrix corresponding to large probabilities for both photons to occupy the same lobe. In contrast, there is almost zero probability for the photons to propagate in different lobes, as heralded by the absence of anti-diagonal peaks<sup>7</sup>. This behaviour, which is reminiscent of the conjoint occurrence of the photons in the channels of the 50/50 coupler (2.21), is referred to as (spatial) ‘photon bunching’.

These evolution patterns of two-photon states have no direct classical equivalent and represent an implementation of a QRW of 2 correlated particles [36, 37].

The correlation of the entangled state depends strongly on the relative phase between the two input channels. For the symmetric state with  $\phi = 0$ , one finds strong anti-diagonal peaks, but almost no peaks on the main diagonal (Fig. 2.3(d)), meaning that

<sup>7</sup>In this particular example  $\Gamma_{5,5} = \Gamma_{18,18} \gg \Gamma_{5,18}$ , etc..

the two photons exhibit ‘antibunching’, i.e., they tend to occupy different lobes. On the other hand, for the antisymmetric state  $\phi = \pi$  (Fig. 2.3(e)) a bunching behaviour can be observed again, which is very similar to the correlation pattern of the product state.

In all cases there is also a correlation between the lobes and the inner parts of the evolution pattern: If one photon is detected in an even(odd)-numbered inner channel for the input states  $|\Psi^{(p)}\rangle$  or  $|\Psi^{(e,\pi)}\rangle$ , the other must propagate in the lower(upper) ballistic lobe, and vice versa for  $|\Psi^{(e,0)}\rangle$ .

As outlined in the introduction, a major goal of this work is the realisation of waveguide lattices supporting more intricate photon pair trajectories, either by introducing a non-uniform distribution of couplings or detunings to a 1D lattice, or by exploiting the second spatial dimension. These strategies necessitate a fabrication technique which allows a precise control of the parameters of the waveguide lattice as well as the ability to assemble the waveguides in two dimensions. The direct waveguide inscription by ultrashort laser pulses into glass represents such a technique and will be explained in the next section.

## 2.3 Waveguide inscription

Optically transparent media, such as fused silica glass, exhibit an energy gap between their valence and conduction bands which is much larger than the energy of a photon from the visible or near-infrared spectral range. Therefore, they do not absorb light under normal circumstances. However, at very high light intensities, field ionisation as well as multiphoton absorption processes can occur in which the (cumulative) energy of the photons is large enough to bridge the gap. Together with onsetting avalanche ionisation, recombination and restructuring processes, this can lead to a permanent modification of the material’s refractive index [73].

In case of fused silica and an illumination wavelength of  $\lambda_{\text{in}} = 800 \text{ nm}$  intensities in the order of  $10^{17} \text{ Wm}^{-2}$  are required to achieve this [32]. Such an intensity can be obtained by focussing laser pulses with pulse durations in the order of  $\tau \sim 100 \text{ fs}$  and pulse energies in the order of  $E_p \sim 100 \text{ nJ}$  onto spot diameters of a few  $\mu\text{m}$ . Commercial amplified femtosecond laser system can routinely deliver such pulse parameters.

For all experiments presented in this work a Coherent Mira/RegA oscillator/amplifier system is employed delivering pulses with  $\lambda_{\text{in}} = 800 \text{ nm}$ ,  $\tau \approx 150 \text{ fs}$  and  $E_p \approx 250 \text{ nJ}$  at a repetition rate of  $100 \text{ kHz}$ . The pulses are focussed using a  $20\times$ -objective (numerical aperture  $NA = 0.35$ ). In order to fabricate waveguides, a glass chip is moved continuously on a translation stage (Aerotech) under illumination, resulting in elongated waveguides (see



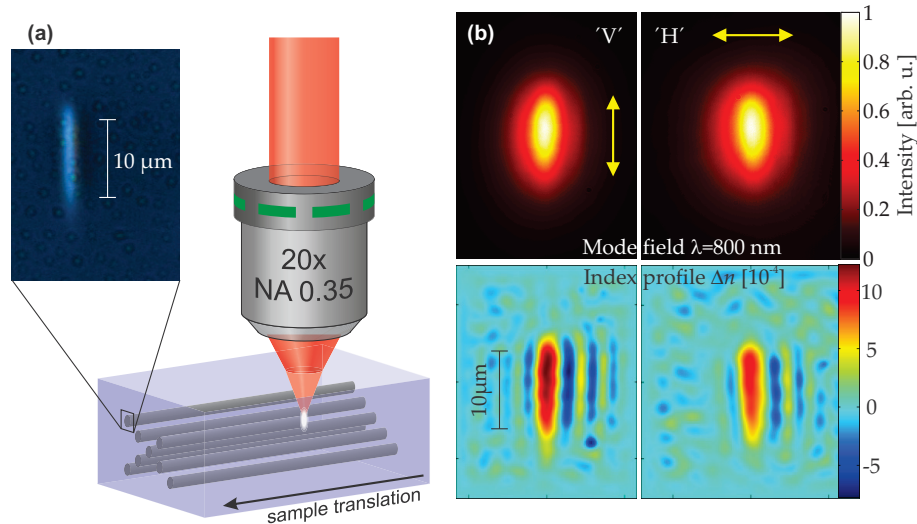


**Figure 2.4:** (a) Direct inscription of waveguide arrays by femtosecond laser pulses. The inset shows a phase-contrast microscope image of a waveguide’s end face. (b) Top: Typical mode profiles at  $\lambda = 800$  nm for the two orthogonal linear polarisations ‘H’ and ‘V’. The arrows indicate the direction of the electric field  $\mathbf{e}$ . Bottom: Associated refractive index profiles which are calculated from the mode profiles.

Fig. 2.4(a)). The laser pulses are polarised linearly and perpendicularly to the writing direction. The maximum waveguide length feasible with the employed positioning system is 10 cm. The translation velocity  $v_0$  controls the amount of energy deposited per unit length, and thereby the propagation constant  $\gamma$  of the waveguide: The slower the inscription, the more energy is deposited and the larger  $\gamma$  [33]. Here, velocities between 1 and  $1.8 \text{ mm s}^{-1}$  are typically used. The process can be repeated several times after a transverse shift of the sample in order to produce 2D waveguide arrays of arbitrary shape<sup>8</sup>. As governed by (2.13), the coupling strength  $C$  between two guides depends on the overlap of the waveguide modes, which can also be controlled by the writing velocity, as well as by the waveguide separation. Usually the latter option is preferable in order to tune  $\gamma$  and  $C$  independently<sup>9</sup>. One finds an exponential dependence between the waveguide separation and  $C$  over a large range of parameters [75] (see chapters 5.1 and 6.1 for details).

As visible from the inset of Fig. 2.4(a), the waveguides exhibit an elliptical cross-section of about  $10 \times 2 \mu\text{m}^2$ . Moreover, anisotropic stress fields are induced during the inscription

<sup>8</sup>The working distance of the employed microscope objective is large enough to allow waveguide inscription in the entire volume of the 1 mm thick glass samples. Note that the writing depth with minimum focal radius is  $170 \mu\text{m}$ , as this is the cover glass thickness for which the microscope objective is designed [74]. A variation of depth leads to slightly changing waveguide properties due to spherical aberrations. However, this effect is insignificant for the employed low- $NA$  objective and the dimensions of the waveguide lattices in this work [33].

<sup>9</sup>If different writing velocities are used for the waveguides within a lattice, the impact on  $\gamma$  is usually much larger than on  $C$ .

process [76]. For these reasons, the waveguide modes are no longer polarisation degenerate, as they would be in circular guides of isotropic material. Instead, the waveguide supports two modes with linear orthogonal polarisations oriented along the major principal axis of the ellipse (termed ‘V-polarisation’) and perpendicular to it (‘H-polarisation’). Fig. 2.4**(b)** displays exemplary intensity profiles of these modes for waveguides fabricated with the parameters  $\tau = 170$  fs,  $E_p = 300$  nJ,  $v_0 = 1.5$  mm s<sup>-1</sup> and the associated refractive index profiles  $\Delta n = \frac{\Delta\epsilon}{2n_0}$ ,<sup>10</sup> which can be calculated via inversion of the Helmholtz equation (2.2) [77].

In the given example the refractive index contrast is approximately  $10^{-3}$  and the propagation constants of the modes (with respect to the bulk) are in the order of  $500$  m<sup>-1</sup> at  $\lambda = 800$  nm. The birefringence, i.e., the difference between the propagation constants of the two modes, has been measured in another sample with comparable fabrication parameters to be  $\gamma_V - \gamma_H \approx 60$  m<sup>-1</sup>. Hence, a phase shift of  $\pi$  between the two polarisation modes can be expected for a propagation length of about 5 cm. Therefore, the input polarisation of photons should always be chosen as either ‘V’ or ‘H’, as any superposition state would change considerably during a propagation on this length scale. This will be crucial for photon-pair experiments as discussed in chapters 4.2 and 6.2.

One can further notice from Fig. 2.4**(b)** that also the modal shape depends on polarisation, it is typically wider for ‘H’. Therefore the coupling, governed by the overlap to neighbouring waveguide modes, is usually larger for ‘H’ than for ‘V’. Hence, one has to choose a particular polarisation when designing specific distributions of the coupling constant in a waveguide lattice. Some promising approaches towards waveguides with polarisation independent coupling will be discussed in the outlook at the end of this thesis.

The propagation loss of laser-written waveguides depends on the fabrication parameters and the exact type of the glass used. Typical values for the parameter range used in this work are  $0.7 \dots 1.1$  dBcm<sup>-1</sup> at  $\lambda = 800$  nm, with the lowest losses of  $0.5$  dBcm<sup>-1</sup> obtained for inscribing the waveguide twice. As discussed earlier, losses are uncritical as long as they are equal among all waveguides<sup>11</sup>. They merely reduce the arrival probabilities and correlations of the photons globally, but do not alter their distribution.

For interfacing waveguide arrays with photon sources and detectors (see the following section for details), it is often necessary to include curved waveguide segments on a chip. Such a bending necessarily involves additional losses [78]. Again, the severity of these losses depends strongly on the fabrication parameters, the material and the waveguide trajectory. Generally speaking, bending radii in the order of 1 m are bearable for most

---

<sup>10</sup> $n_0 = 1.45$  for fused silica

<sup>11</sup>Of course, they should be small enough to still allow appreciable signals in an experiment.

experiments in laser-written waveguides.

## 2.4 Generation and detection of indistinguishable photon pairs

To understand what the crucial aspects in designing waveguide devices for single-photon experiments are, a brief excursion to the commonly employed methods of photon pair generation and detection is required.

The most widely used process for the generation of photon pairs is spontaneous parametric down-conversion (SPDC) [63, 79], a nonlinear optical process, which converts a pump photon of frequency  $\omega_p$  into signal and idler photons with frequencies  $\omega_s$  and  $\omega_i$ , satisfying energy conservation  $\omega_p = \omega_s + \omega_i$ . To harness the required second-order nonlinearity<sup>12</sup>, birefringent crystalline materials with non-centrosymmetric unit cell are employed. Momentum conservation (phase matching) allows only certain directions for the participating wavevectors  $\mathbf{k}_p$ ,  $\mathbf{k}_s$  and  $\mathbf{k}_i$ , depending on the frequencies, the refractive indices and the orientation of the nonlinear crystal, as well as the photon polarisation. There is a manifold of solutions to the energy and momentum conservation. Of particular interest for the generation of indistinguishable photons is the so-called type-I phase matching, where the pump photon is extraordinarily polarised, while the signal and idler photons are both identically polarized in the ordinary direction (see Fig. 2.5(a)) [59]. For certain angles between the optical axis of the crystal and the pump beam  $\Theta$ , the degenerate case  $\omega_s = \omega_i = \omega_p/2$  is possible. In this configuration photons of identical frequency and polarisation are emitted into a cone with opening angle  $\phi_s + \phi_i = 2\phi_s$  around the pump direction, as shown in Fig. 2.5(b) [80]. Due to the momentum conservation, the two photons are always directed at opposite points of the cone. Hence, selecting two such points by apertures and connecting them to polarisation-maintaining optical fibers provides a source for pairs of indistinguishable photons<sup>13</sup>. The frequency conversion is a spontaneous process, so the photon pairs are obtained at random times with a rate depending on numerous parameters, such as pump beam intensity in the crystal, the nonlinearity and phase-matching as well as the size of the apertures.

The devices of choice for single photon detection are reverse-biased silicon avalanche

<sup>12</sup>In a second-order nonlinear optical process, the polarisation response of the medium is proportional to the second power of the electric field.

<sup>13</sup>For a finite length of the crystal, the phase matching condition is not sharp, hence the photons have a certain spectral width. Usually, this is further confined by interference filters, down to a few nm. This also determines the temporal width of the photon wavepackets to the order of  $\sim 100$  fs for  $\lambda_s = \lambda_i \approx 800$  nm.

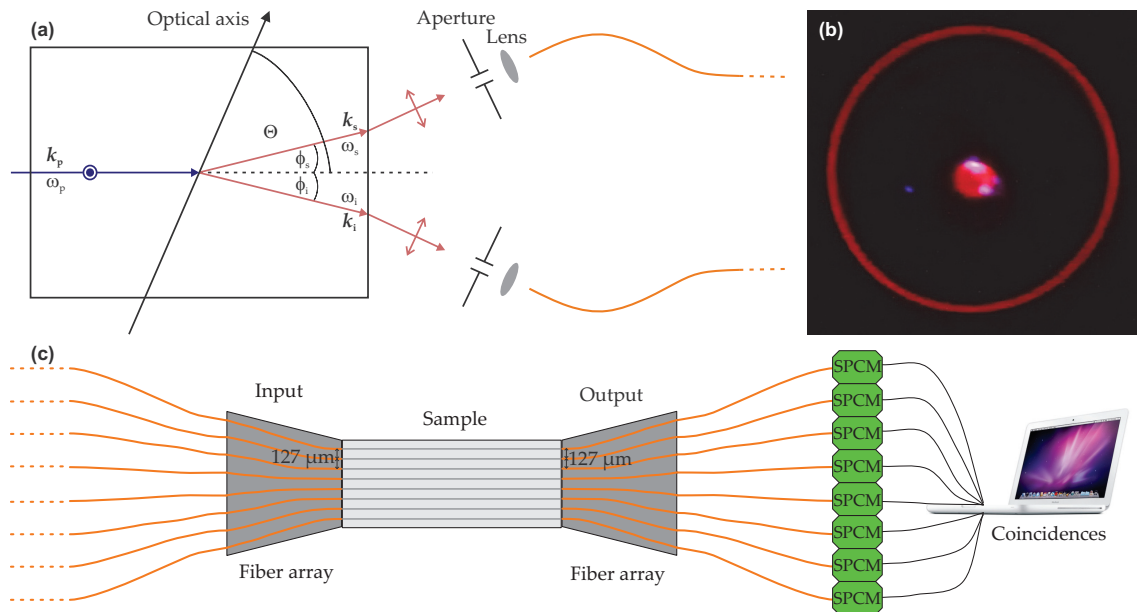


**Figure 2.5:** Generation and detection of photon pairs and their interfacing with waveguide lattices. **(a)** SPDC in a type-I phase matched nonlinear crystal. A pump photon with extraordinary polarisation (perpendicular to the plane) is converted to signal and idler photons with ordinary (parallel) polarisation which are collected by optical fibers. **(b)** Measured intensity distribution behind a  $\text{BiB}_3\text{O}_6$ -crystal pumped by a 100 mW continuous wave laser with  $\lambda_p = 407.5$  nm and phase matching adjusted to the degenerate case  $\lambda_s = \lambda_i = 815$  nm. The outer ring shows the cross-section through the cone of signal and idler photons with an opening angle of  $14.4^\circ$  after refraction at the crystal endface and the central part belongs to residual pump light passing a bandpass filter, which suppresses the pump light by six orders of magnitude. **(c)** Schematic illustration of the interfacing between the glass sample containing the waveguide lattice and optical fibers coming from the source and going to SPCMs. Images are taken from [80].

photo diodes, in which a large voltage is applied against the current transmitting direction of their pn-junction. Upon absorption of a photon within the depletion region, an electron-hole pair is generated, separated and swept across the junction. If the voltage is large enough, the charge carriers are accelerated to sufficient energies to generate yet more carriers by impact ionisation. This process sustains itself, triggering an avalanche of carriers which can be detected as a macroscopic current [81, 82]. As a single photon suffices to start an avalanche, the photon number incident on the detector at a given time can naturally not be resolved. Such reverse-biased avalanche diodes together with all the required electronics are commercially available as single photon counting modules (SPCMs), often fed by optical fibers. SPCMs are bucket detectors, i.e., they are spatially non-resolving. Hence, one detector is required for each optical mode under investigation.

A fused silica sample containing laser-written waveguides can be interfaced on both sides with the fibers coming from the photon source and leading to the detectors. This is done

most conveniently by attaching the fibers to commercial fiber-arrays, which transversally align up to eight individual fiber cores on a line with a pitch of  $127\ \mu\text{m}$ . These fiber arrays must then be connected to the end faces of the waveguide lattice, as illustrated in Fig. 2.5(c). To do so, the waveguide chip has to start with a 1D array with a waveguide spacing of  $127\ \mu\text{m}$ . However, typical separations between evanescently coupled waveguides at  $\lambda \approx 800\ \text{nm}$  are in the order of  $15 \dots 30\ \mu\text{m}$  and the waveguide lattice is not always in a 1D geometry. To overcome this problem, the planar, widely spaced arrangement of waveguides at the input and output faces has to be mapped to the geometry of the particular lattice under investigation with its smaller separations by curved waveguide segments [37, 71]. The curved segments of the individual guides may vary in length, which has to be compensated by an external delay of the input photons to ensure temporal overlap in the lattice. As mentioned in the previous section, such curvatures necessarily imply additional losses, which tend to become severe for laser-written waveguides with bending radii below about  $\sim 1\ \text{m}$ . This ultimately limits the number of waveguides which can be brought together in a lattice and connected to fiber arrays on the maximum processable glass chip length of  $10\ \text{cm}$ .

# 3 Classical Characterisation of Quantum Interference

The considerable effort of photon pair generation, detection and interfacing with the waveguide lattice presented in the previous chapter is a seriously limiting factor to the lattice design as well as to the speed at which a lattice can be characterised after its fabrication. In contrast, if an investigation of the QRW with classical light was possible, these constraints would be substantially relaxed.

In this chapter it will be shown that the quantum path interference of indistinguishable photon pairs, as characterised by the two-photon correlation function (2.19) introduced in the previous chapter, can be effectively simulated with classical light interference. Instead of a single quantum experiment, a series of measurements with coherent states of light (i.e., laser beams) is employed to obtain a classical correlation function having an expectation value which is identical to the quantum correlation for any waveguide lattice. This is particularly useful, as it provides a practical procedure for a characterisation of a given waveguide array regarding its expected impact on the evolution of two-photon states without the above mentioned issues. The basic version of this experimental procedure can be applied to the emulation of product states of the type (2.24) and is presented in the first section. A refined technique applicable to path-entangled states (2.25) is introduced in the section thereafter.

## 3.1 Photon pairs in a product state

As in chapter 2.2.3, arbitrary waveguide lattices are considered with the evolution of the ladder operators governed by (2.17) and the general solution (2.22). The aim is to find a procedure which allows a classical characterisation of the quantum path interference of the product state  $|\Psi_{k,l}^{(p)}\rangle$ .

The evolution of a classical light field in such a system is governed by the same type of equation, only the ladder operators are replaced by  $z$ -dependent discrete modal amplitudes

$\{b_n\}_{n=1}^N$  [26, 63, 65]:

$$i \frac{d}{dz} b_m(z) + \sum_{k=1}^N \tilde{C}_{k,m} b_k(z) = 0. \quad (3.1)$$

Of course, this equation is solved by the same matrix exponentials  $U$  as in (2.22).

If a single waveguide  $k$  is excited with intensity  $I_0$ , i.e., the initial condition is  $b_m(0) = \sqrt{I_0} \delta_{m,k}$ , one obtains for the intensity distribution at a given position  $z$ :

$$I_m^k(z) = |b_m(z)|^2 = I_0 |U_{m,k}(z)|^2. \quad (3.2)$$

Now consider two waveguides  $k$  and  $l$  being excited with equal intensity  $I_0$  and a certain relative phase  $\Phi$ :  $b_m(0) = \sqrt{I_0} (\delta_{m,k} + \delta_{m,l} e^{i\Phi})$ . Clearly, the output light distribution will depend on this phase, due to classical wave interference:

$$I_m^{k,l}(z, \Phi) = I_0 |U_{m,k}(z) + U_{m,l}(z) e^{i\Phi}|^2. \quad (3.3)$$

Note that there is no relative phase between the individual photons in the quantum case, as Fock states have no well-defined phase [53, 54]. On the other hand, there is no quantum path interference in the classical case.

Nonetheless, the quantum correlation  $\Gamma_{m,n}^{(p)}$  of (2.27), describing the quantum path interference of the two-photon product state, can be emulated with a series of classical measurements. To this end, one measures the output intensity distribution for a series of random settings of  $\Phi$ . Then, the phase averaged intensity correlation

$$\Gamma_{m,n}^{(\text{int})}(z) \equiv I_0^{-2} \langle I_m^{k,l}(z, \Phi) I_n^{k,l}(z, \Phi) \rangle_{\Phi}, \quad (3.4)$$

can be calculated from this data, with  $\langle \cdot \rangle_{\Phi}$  denoting the average over all phase realisations. With (3.3) and the fact that all terms with a phase factor vanish upon averaging one finds [36]

$$\Gamma_{m,n}^{(\text{int})} = |U_{m,k} U_{n,l} + U_{m,l} U_{n,k}|^2 + |U_{m,k} U_{n,k}|^2 + |U_{m,l} U_{n,l}|^2, \quad (3.5)$$

where the argument  $z$  has been, and will be henceforth, omitted for the sake of clarity. This intensity correlation is used in [36] to characterise the two-photon correlation function of the product state. Clearly, it is biased by the last two terms, which contain the output intensities from the single waveguides excitations (3.2). However, subtracting these terms from the intensity correlation overcomes this bias, yielding exactly the same expression as given by (2.27):

$$\Gamma_{m,n}^{(c)} \equiv \Gamma_{m,n}^{(\text{int})} - I_0^{-2} (I_m^k I_n^k + I_m^l I_n^l) = \Gamma_{m,n}^{(p)}. \quad (3.6)$$

Hence, the quantum correlation function of the product state can, in principle, be obtained by a series of intensity measurements for coherent excitation of the waveguide array, independently of the particular geometry of the lattice [62]. In other words, the quantum path interference of two indistinguishable photons can be emulated by classical light interference. One just requires a larger number of measurements.

However, one should not misunderstand this result in a sense that the entire dynamics of the quantum system and the classical light were the same. Only the expectation values of the two-photon coincidence  $\Gamma_{m,n}^{(p)}$  and the classical phase-averaged intensity correlation  $\Gamma_{m,n}^{(c)}$  are identical. Higher moments, such as their variances, are different for both methods [62]. In that sense the quantum interference of photon pairs is merely *emulated* by classical light interference, even though both correlation functions are identical. Besides that, only a finite number of phases can be realised in an actual experiment, therefore the averaging required to obtain the result (3.5) will usually not be perfect.

Nonetheless, the ability to investigate quantum interference in waveguide lattices without the complications of having to use single-photon sources and detectors should be a useful one, which is why a procedure for such classical experiments is outlined next and illustrated in Fig. 3.1.

First, one has to launch a light beam subsequently into the targeted sites  $k$  and  $l$  of the waveguide array and monitor the output intensity distribution in order to obtain the terms for single-guide excitation in Eq. (3.6). This is done by focussing a laser beam onto the front face of the array and image its output face onto a camera (see solid line in

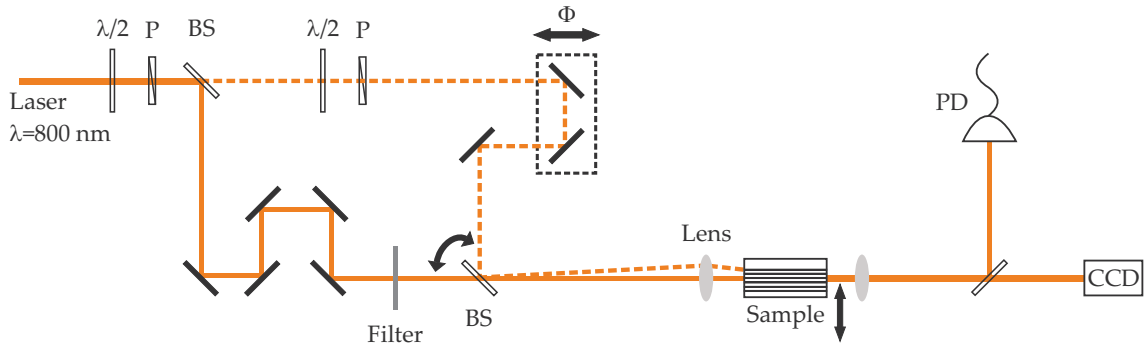


**Figure 3.1:** Experimental setup for the classical characterisation of quantum interference. Two beam splitters (BS) form a Mach-Zehnder interferometer with a variable delay line to control  $\Phi$ . The position of the sample is adjusted to select the input channel for the beam travelling through the interferometer arm shown as solid line, whereas a tilt of the combining (thin) BS selects the input waveguide for the other beam (dashed line). The power of the two beams is monitored after the sample by a photodiode (PD) and adjusted by an attenuation filter, polarisers (P) and half-wave plates, to accommodate for different input coupling efficiencies.



Fig. 3.1).

The two-channel input is realised in a Mach-Zehnder setup with one arm having a variable delay to adjust the relative phase  $\Phi$  as well as polarisers and half-wave plates to control the power in each beam independently. The input channels of the two beams can be chosen separately by tilting the combining beam splitter which leads to a lateral shift on the sample's front face. However, the tilted phase front of the beam as well as lens astigmatism arising from its off-optical-axis alignment lead to a reduced overlap with the waveguide mode, thereby reducing the input coupling efficiency. To some extent, this can be compensated by adjusting the power of the beams, but there is an ultimate limit for the experimentally feasible separation between the two input guides mainly depending on the input lens. For the employed microscope objectives with  $NA \sim 0.1$  this is in the order of  $100 \dots 200 \mu\text{m}$ , corresponding to typically  $\sim 5 \dots 10$  waveguides in a nearest-neighbour coupled lattice.

To measure the intensity correlation (3.4) with this setup one has to align the two beams onto the input channels  $k$  and  $l$ , choose a series of random phase settings and record the output intensities for each phase, ensuring that both input waveguides are always excited with the same amplitude. In practice, the particular value of the phase does not matter, so one can simply apply a random displacement to the delay at each step. In this setup an adjustable mechanical table with a positioning precision of about  $\sim 5 \mu\text{m}$  was used, which gives independent, random phase values for each displacement ( $\lambda \approx 800 \text{ nm}$ ).

This experimental method will be applied in chapters 4.1 and 5.2.

In the following, it is briefly discussed how the finite number of random phases in an actual measurement will affect the result. To this end, the homogeneous 1D-array of Fig. 2.3 from the previous chapter is revisited. To simulate a measurement following the classical scheme,  $\Gamma_{m,n}^{(c)}$  is evaluated according to Eq. (3.6) for a uniform distribution of  $S$  independent phases on the interval  $[0, 2\pi]$ . Fig. 3.2(a) displays an exemplary classical correlation for  $S = 20$  and otherwise perfect conditions. A comparison to the quantum correlation (Fig. 2.3(c)) shows a close agreement, especially in the fine structure of the correlation map and in the absence of any off-diagonal peaks. The only notable difference are the individual heights of the bunching-peaks on the main diagonal.

To proceed from this rather heuristic observation to a quantitative statement, a statistical simulation with an ensemble of 10,000 realisations of  $S$  random phases is conducted. A useful quantity for measuring the deviations from the true quantum correlation is the mean square error

$$\mathcal{E}_{m,n}^{\text{MS}} \equiv \left\langle \left( \Gamma_{m,n}^{(c)} - \Gamma_{m,n}^{(p)} \right)^2 \right\rangle_{\text{E}},$$

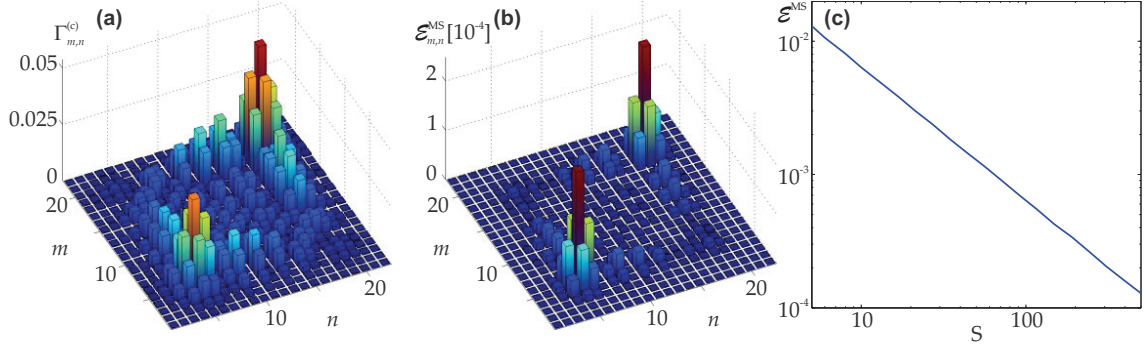


**Figure 3.2:** Intensity correlation for the emulation of product states in a 1D array with a finite number of phase realisations. The same lattice and input state as in Fig. 2.3(c) are considered. (a) Calculated correlation  $\Gamma_{m,n}^{(c)}$  for averaging over 20 random phases. (b) Distribution of the mean-square error, obtained by averaging over 10,000 sets of 20 random phases in a statistical simulation. (c) Overall mean-square error in dependence of the number of phases. Again 10,000 sets have been used for each datapoint.

with  $\langle \cdot \rangle_E$  denoting the average with respect to the ensemble of random phase sets. The mean square error for  $S = 20$  is shown in Fig. 3.2(b), corroborating the previous observation: Errors occur mostly where the correlation function has large values, but the zeros are practically unaffected. Here this means that the on-diagonal peaks are affected by the finite number of phases, whereas the absence of off-diagonal peaks is not.

One finds that the distribution of the mean square error is independent of  $S$ , merely its magnitude changes. To illustrate this dependence, the total mean square error

$$\mathcal{E}^{MS} \equiv \sum_{m,n=1}^N \mathcal{E}_{m,n}^{MS}$$

is plotted against  $S$  in Fig. 3.2(c). From this graph it is evident that the overall error  $\sqrt{\mathcal{E}^{MS}}$  scales with the inverse of the square root of  $S$ :  $\sqrt{\mathcal{E}^{MS}} \propto S^{-1/2}$ . For  $S = 20$ , the relative error is in the range of a few percent:  $\sqrt{\mathcal{E}^{MS}} / \sum_{m,n} \Gamma_{m,n}^{(p)} = \sqrt{\mathcal{E}^{MS}} / 2 \approx 0.03$ .

It is important to note that these errors are of purely random nature. The reason is that the expectation value of the classical correlation function is always equal to the quantum correlation, regardless of how many phases are used for the average:  $\langle \Gamma_{m,n}^{(c)} \rangle_E = \Gamma_{m,n}^{(p)}$ . Therefore, the finite number of phase realisations does not bias the emulator.

So far, this classical characterisation is restricted to quantum correlations arising from product states being input to the lattice. However, as it will be outlined in the following section, it is even possible to obtain the quantum correlation of path-entangled input states, which are highly nonclassical by their very nature, by purely classical measurements.

## 3.2 Photon pairs in an entangled state

In this section, the procedure presented above will be extended, in order to emulate the quantum path interference of entangled input states.

One can expand the expression for the quantum correlation of the entangled state (2.28) to:

$$\begin{aligned}\Gamma_{m,n}^{(e,\phi)} &= |U_{m,k}U_{n,k}|^2 + |U_{m,l}U_{n,l}|^2 + (U_{m,k}U_{n,k}U_{m,l}^*U_{n,l}^*e^{i\phi} + \text{c.c.}) \\ &= I_0^{-2} (I_m^k I_n^k + I_m^l I_n^l) + (U_{m,k}U_{n,k}U_{m,l}^*U_{n,l}^*e^{i\phi} + \text{c.c.}),\end{aligned}\quad (3.7)$$

where the first two terms correspond again to products of classical intensities from single-waveguide excitation. As explained before these intensities can be directly measured. One is left with the task of finding a classical expression for the last term.

This interference term depends on the phases of  $U$ , which can clearly not be extracted from single-waveguide input intensity measurements. A similar problem arises in classical interferometry, where the phase information of an optical system cannot be obtained unambiguously with a single optical mode. The solution there is to overlap two optical modes with several well-defined relative phases [83]. Here, such a phase-stepping scheme is employed to retrieve the phase information of the waveguide lattice. To this end, the output intensities  $I_m^{k,l}(\Phi_j)$  for a two-channel excitation of guides  $k$  and  $l$  (see eq. (3.3)) and a set of 4 fixed relative phases

$$\left\{ \Phi_j = \frac{1}{2} (j\pi - \phi) \right\}_{j=0}^3 \quad (3.8)$$

are required, assuming that the phase  $\phi$  of the quantum state is known. From this data one can calculate a modulated intensity correlation:

$$\Gamma_{m,n}^{(\text{int},\phi)} \equiv \frac{1}{4I_0^2} \sum_{j=0}^3 (-1)^j I_m^{k,l}(\Phi_j) I_n^{k,l}(\Phi_j). \quad (3.9)$$

A lengthy, but straightforward calculation shows that (see Appendix A.1 for details)

$$\Gamma_{m,n}^{(\text{int},\phi)} = U_{m,k}U_{n,k}U_{m,l}^*U_{n,l}^*e^{i\phi} + \text{c.c.}, \quad (3.10)$$

which is precisely the third term of (3.7). Hence, the correlation function of the path-entangled photon pair and the classical expression

$$\Gamma_{m,n}^{(c,\phi)} \equiv I_0^{-2} (I_m^k I_n^k + I_m^l I_n^l) + \Gamma_{m,n}^{(\text{int},\phi)} = \Gamma_{m,n}^{(e,\phi)} \quad (3.11)$$

are identical. Again this quantity is obtained by purely classical measurements and it allows the determination of the expectation value of the two-photon coincidence. Therefore, the quantum interference of path-entangled photon pairs is emulated by six classical intensity measurements.

The main difference to the previous scheme is that instead of random phases, well-determined phase settings are required. In principle, the same setup as shown in Fig. 3.1 can be employed, however the phase  $\Phi$  has to be precisely controlled and stabilised. On the other hand, such a phase control offers the benefit that much fewer measurements are needed than for the phase-averaging method.

As long as the phase control is perfect, the identity (3.11) holds. However, in an actual experiment, the precision of the phases will be limited, therefore the classical correlation will only serve as an estimator of its quantum counterpart. To model such random phase errors, a Gaussian distribution of the phases  $\Phi_j$  is considered with mean values as given in (3.8) and a standard deviation of  $\sigma_\Phi$ .

Figs. 3.3(a),(b) show a calculation of the intensity correlation  $\Gamma_{m,n}^{(c,\phi)}$  in the 1D waveguide array considered in Fig. 2.3 for the symmetric ( $\phi = 0$ ) and antisymmetric ( $\phi = \pi$ ) input states and a phase error of  $\sigma_\Phi = 0.02\pi$ . This phase error corresponds to a path-length precision of  $\lambda/100$ .<sup>1</sup> The classical result and the corresponding quantum correlations (Figs. 2.3(d),(e)) are practically equal, miniscule differences between some elements of the matrices are barely noticeable. Hence, the classical method recovers the quantum correlation almost perfectly on this level of phase precision.

It should be noted, that systematic phase errors, e.g., due to a lack of positioning accuracy in a setup, also influence the optical emulation. Any offset of the phases will be equivalent to a shift in the quantum phase  $\phi$  (see Eq. (3.8)). Therefore, the resulting classical correlations will be affected. However, the same phase errors will be prevalent in experimental realisations of the quantum state  $|\Psi^{(e,\phi)}\rangle$ , which also require controlled phase shifts of some kind, with the same impact on the correlation function. Hence, systematic phase errors in the classical procedure do not add any uncertainties to the correlations which are not present in the quantum states themselves.

To analyse the impact of phase precision on the method more quantitatively, a statistical simulation is conducted for an ensemble of random phases  $\Phi_j$ . The difference to the investigation in the previous section is that in this case the number of phases is fixed to four, whereas the phase values are randomly deviating from (3.8). Here, it is helpful to

---

<sup>1</sup>Positioning precisions in the nm-range can be achieved by piezoelectric actuators.

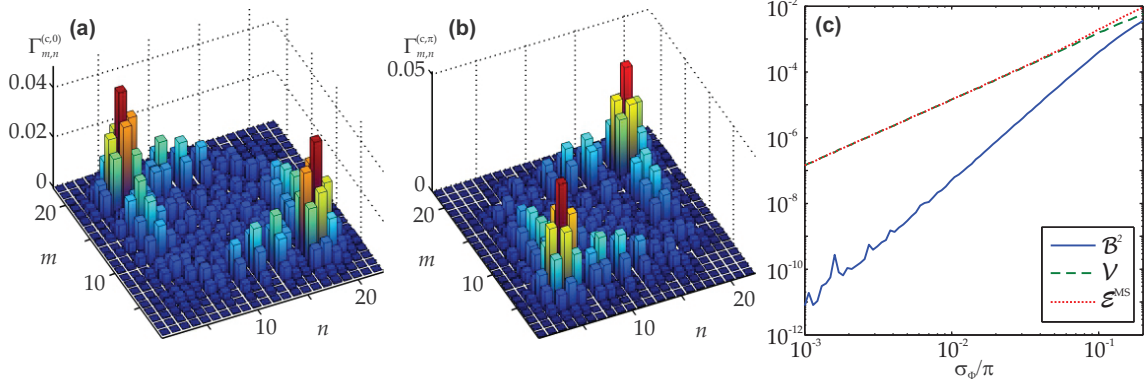


**Figure 3.3:** Intensity correlation for emulation of path-entangled quantum states in a 1D array. The same lattice and input states as in Figs. 2.3(d),(e) are considered. **(a)** Calculated correlation for the symmetric state  $\phi = 0$  and phase error  $\sigma_\Phi = 0.02\pi$ . **(b)** Same for the antisymmetric state  $\phi = \pi$ . **(c)** Statistical simulation of the precision and the accuracy of the method for  $\phi = \pi$  in dependence of  $\sigma_\Phi$ . 10,000 realisations of the phases have been used for each datapoint.

make a distinction between systematic and random errors in the correlations. The total bias square

$$\mathcal{B}^2 \equiv \sum_{m,n=1}^N \left( \langle \Gamma_{m,n}^{(c,\phi)} \rangle_{\text{E}} - \Gamma_{m,n}^{(e,\phi)} \right)^2$$

sums over all squared deviations between the expectation value of the classical correlation and the quantum correlation to be estimated. For perfect phase control the two correlations coincide and  $\mathcal{B} = 0$ . Otherwise,  $\mathcal{B}$  accounts for systematic errors of the scheme which are introduced by phase imprecisions and, thereby, measures the accuracy of the method. Similarly, a total variance can be defined as

$$\mathcal{V} \equiv \sum_{m,n=1}^N \left\langle \left( \Gamma_{m,n}^{(c,\phi)} - \langle \Gamma_{m,n}^{(c,\phi)} \rangle_{\text{E}} \right)^2 \right\rangle_{\text{E}},$$

which measures the spread of the classical correlation around its expectation value, accounting for random errors induced by phase imprecision. Hence,  $\mathcal{V}$  measures the precision of the scheme. The previously encountered mean square error  $\mathcal{E}^{\text{MS}} = \mathcal{B}^2 + \mathcal{V}$  accounts for both types of errors. All three quantities were evaluated within the interval  $0.001\pi \leq \sigma_\Phi \leq 0.2\pi$  via statistical simulations with 10,000 realisations of the phases  $\Phi_j$  for each value of  $\sigma_\Phi$ . The result is plotted for the antisymmetric input state in Fig. 3.3(c), very similar curves are obtained for the symmetric input state. Several statements can be deduced from this graph:

1. For  $\sigma_\Phi \rightarrow 0$ , all errors vanish and the classical method yields exactly the quantum correlation, as required by eq. (3.11).

2. As evident from the slopes of the curves, the bias scales quadratically with phase errors  $\mathcal{B} \propto \sigma_\Phi^2$ , whereas the standard deviation grows only linearly  $\sqrt{\mathcal{V}} \propto \sigma_\Phi$ .
3. For  $\sigma_\Phi \lesssim 0.1\pi$  the overall error of the classical method is dominated by random errors. Consequently inaccuracies play a minor role in this regime, leaving the classical estimator practically unbiased.
4. In the previously considered example  $\sigma_\Phi = 0.02\pi$  one has a relative precision of about  $\sqrt{\mathcal{V}} / \sum_{m,n} \Gamma_{m,n}^{(e,\pi)} = \sqrt{\mathcal{V}}/2 \approx 4 \cdot 10^{-3}$  and a relative accuracy one order of magnitude below that:  $\mathcal{B}/2 \approx 4 \cdot 10^{-4}$ . This corroborates the previous observation from Fig. 3.3(a),(b) that the quantum correlation is estimated very well by the classical scheme at this level of phase precision.

Hence, the classical correlation will lend itself as a very precise and accurate estimator of the correlation matrix, if the experimental setup introduced in the previous section is enhanced to state-of-the-art phase precision levels. However, this is beyond the scope of this work and left as a promising route for future research.

Furthermore, if such a degree of phase control is reached, the classical method for finding the correlation function of product states, introduced in the previous section, can also be simplified from random phase averaging to six measurements in a similar manner<sup>2</sup>.

---

<sup>2</sup>One just has to replace the phase-averaged correlation  $\Gamma_{m,n}^{(\text{int})}$  in Eq. (3.6) by a simplified version of the intensity correlation (3.9), without the modulation factor  $(-1)^j$  and with the fixed phases  $\Phi_j = j\pi/2$ .

# 4 Quantum random walk in two lateral dimensions

As discussed in the introduction and chapter 2.2.3, quantum walks in uniform, planar lattices exhibit a rather limited complexity. They allow merely two directions of propagation, as determined by the two ballistic lobes (cf. Fig. 2.3(a)). A 2D graph, on the other hand, supports a far greater variety of paths for each photon. Hence, a correlated QRW on a 2D graph can occupy a substantially larger Hilbert space than its 1D counterpart, for a given number of photons. Moreover, several physical processes map directly to a QRW on a 2D network. Examples include wave communication between parties of unknown position [84], topological phases in 2D [85] and, if decoherence effects from the environment are included, energy transport in photosynthetic complexes [11, 86].

Therefore, it is of great interest to study correlated QRWs on non-planar geometries. An intersection of two 1D-arrays, forming an X-shaped junction, is considered as a prototype for a 2D-graph in this chapter. In the first part the correlations of photon pairs, which can arise in such a system, are investigated theoretically and by the classical measurements introduced in the previous chapter. The second part then deals with experiments on the single-photon level conducted in cooperation with the University of Bristol. For those measurements a single-photon compatible waveguide chip is required imposing special constraints on design and fabrication.

## 4.1 Photon correlations in intersecting waveguide arrays

The geometric structure of the system under consideration is illustrated in Fig. 4.1(a). Two planar arrays of 7 identical waveguides intersect at their central lattice sites, resulting in a 2D graph with 13 nodes, labelled as indicated in the figure. The nearest-neighbour coupling  $C$  is assumed to be uniform in all branches. Due to the relative proximity of the guides adjacent to the centre, their cross-coupling cannot be neglected and is therefore included as a second-order coupling  $\kappa$  into the analysis. In agreement with the experimen-

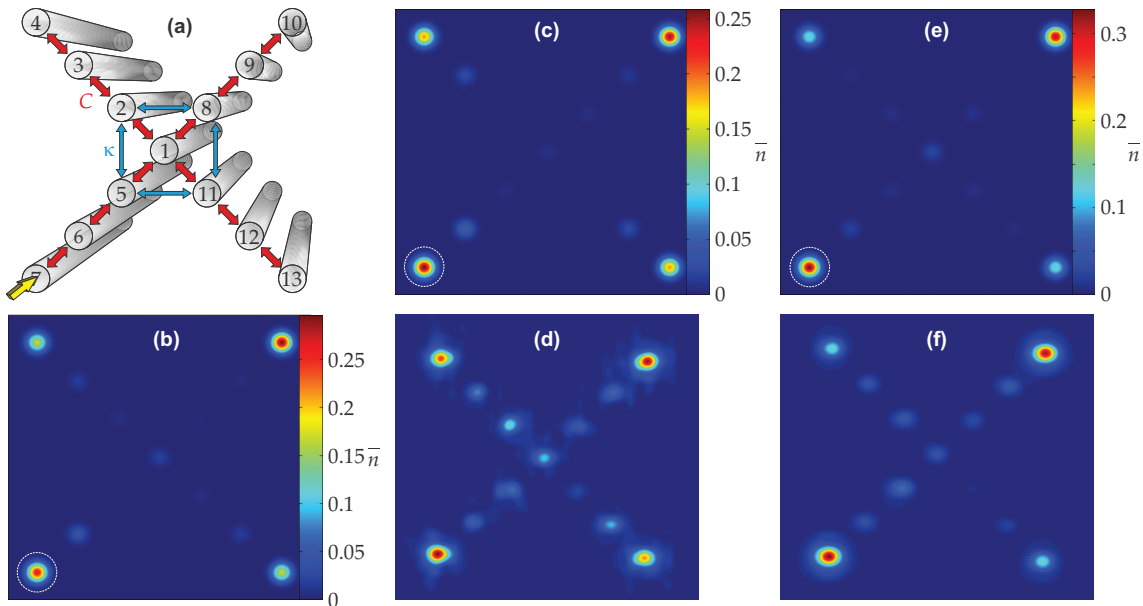


**Figure 4.1:** Single-photon dynamics in an X-junction of waveguide arrays. **(a)** Structure of the lattice with nearest neighbour-coupling  $C$  and second-order coupling  $\kappa$ . **(b)** Calculated mean photon number distribution at  $z = 1.37\pi/C$  for an excitation of the lower left corner (guide no. 7, white circle; arrow in **(a)**) and  $\kappa = 0.22C$ . **(c)** Same as **(b)**, but with a detuning of the central guide  $\beta_1 = -0.9C$ . **(d)** Measured output intensity distribution in the experimental realisation of the lattice from **(c)**. **(e,f)** As **(c,d)**, but with a positive detuning  $\beta_1 = 0.7C$ . The experimental images have the same colormap as the theoretical data and are normalised to their respective peak intensity.

tal conditions, a value of  $\kappa = 0.22C$  is used for all calculations; any further higher-order couplings are neglected.

If one of the corner waveguides is excited, the photon couples ballistically towards the centre where it is scattered into all 4 branches. Note that there is usually a significant reflection back into the input branch, as the intersection distorts the periodicity of the array, hence constituting a defect. After a certain propagation distance, the lobes reach the corners and the photon is most likely localised in one of the four outermost waveguides. For the size of the system considered here, such a distribution is reached at  $z \approx 1.4\pi/C$  (see Fig. 4.1**(b)**). Due to the second-order coupling  $\kappa$ , the symmetry between the three non-input branches is broken, resulting in non-identical output probabilities in the termini. Specifically, less amplitude is diverted into the side branches ( $\bar{n}_4 = \bar{n}_{13} \approx 0.17$ ) than in the forward and backward direction ( $\bar{n}_{10} \approx 0.30$  and  $\bar{n}_7 \approx 0.26$ ). Interestingly, this distribution can be influenced by a detuning of the central waveguide  $\beta_1$ . One finds that a modest detuning towards lower propagation constants increases the amplitude in the side branches, whereas a positive detuning decreases it. Fig. 4.1**(c)** shows the output distribution for  $\beta_1 = -0.9C$ , with enhanced probability for the side branches ( $\bar{n}_4 = \bar{n}_{13} \approx 0.19$



and  $\bar{n}_7 \approx \bar{n}_{10} \approx 0.25$ ). For the opposite sign of detuning  $\beta_1 = 0.7C$ , the coupling into the side branches is reduced ( $\bar{n}_4 = \bar{n}_{13} \approx 0.13$  and  $\bar{n}_7 \approx \bar{n}_{10} \approx 0.32$ ), as visible in Fig. 4.1(e). In the latter scenario, it is most likely that the photon either remains in its input branch or moves to the forward branch. The 2D character of the graph therefore becomes less pronounced than in the case of negative detuning, as there is a lower probability for the photon to leave its initial plane. In this sense, the propagation constant of the inner waveguide can be employed to tune the effective dimensionality of the X-junction.

In order to test this feature in an experiment, two such X-lattices were implemented by the laser-writing technique (see chapter 2.3). A 10 cm long lattice has been inscribed with a writing velocity of  $1.67 \text{ mm s}^{-1}$  and an inter-waveguide spacing of  $30 \mu\text{m}$ . The detunings of the central waveguide were obtained by inscribing the inner guide with  $1.5 \text{ mm s}^{-1}$  in the positively detuned case and  $1.83 \text{ mm s}^{-1}$  for the negative detuning. Subsequently, a single H-polarised laser beam ( $\lambda = 786 \text{ nm}$ ) was focussed into the corner waveguide no. 7 and the output intensities were recorded with a CCD camera (one arm of the interferometer setup shown in Fig. 3.1 was used). Figs. 4.1(d) and (f) show the measured intensity distributions for a negative and a positive central detuning, respectively. As mentioned earlier, normalised classical intensity distributions are identical to the probability distribution for a single photon. In this sense, the observed patterns match the expected photon distributions very closely, with  $C = 0.43 \text{ cm}^{-1}$ ,  $\kappa = 0.22C$  and  $\beta_1 = -0.9C(0.7C)$  being the best-fit parameters to the experimental data. Hence, the strength of connection between the input and the side branches can indeed be controlled by a variation of the refractive index of the central waveguide.

In the next step, the correlation of the two-photon product state  $|\Psi_{7,10}^{(p)}\rangle$  is investigated for an excitation of two opposite corners. The paths of both photons meet in all four corners, which promises a rich quantum path interference.

The expected photon number distribution  $\bar{n}$  in case of a negative detuning is shown in Fig. 4.2(a). As for any configuration, it is the incoherent sum of the distributions from the two single excitations (cf. Fig. 4.1(c)). On average, about 0.5 (0.4) photons will be detected in the corners of the input(side) branches. However, the photon correlation  $\Gamma_{m,n}^{(p)}$  (Fig. 4.2(b)) exhibits some remarkable features. The red peaks belong to guides 7 and 10, i.e., to the corner waveguides of the input branches, whereas the green peaks occur at the side-branch corners 4 and 13. There are practically no correlations at all between these two planes<sup>1</sup>, so the photons are either both in the input branches or the side branches. This is reminiscent of the Hong-Ou-Mandel effect and the correlations in a 1D-array (see

<sup>1</sup>That is,  $\Gamma_{4,7}^{(p)} \ll \Gamma_{4,4}^{(p)}, \Gamma_{7,7}^{(p)}$ , etc.

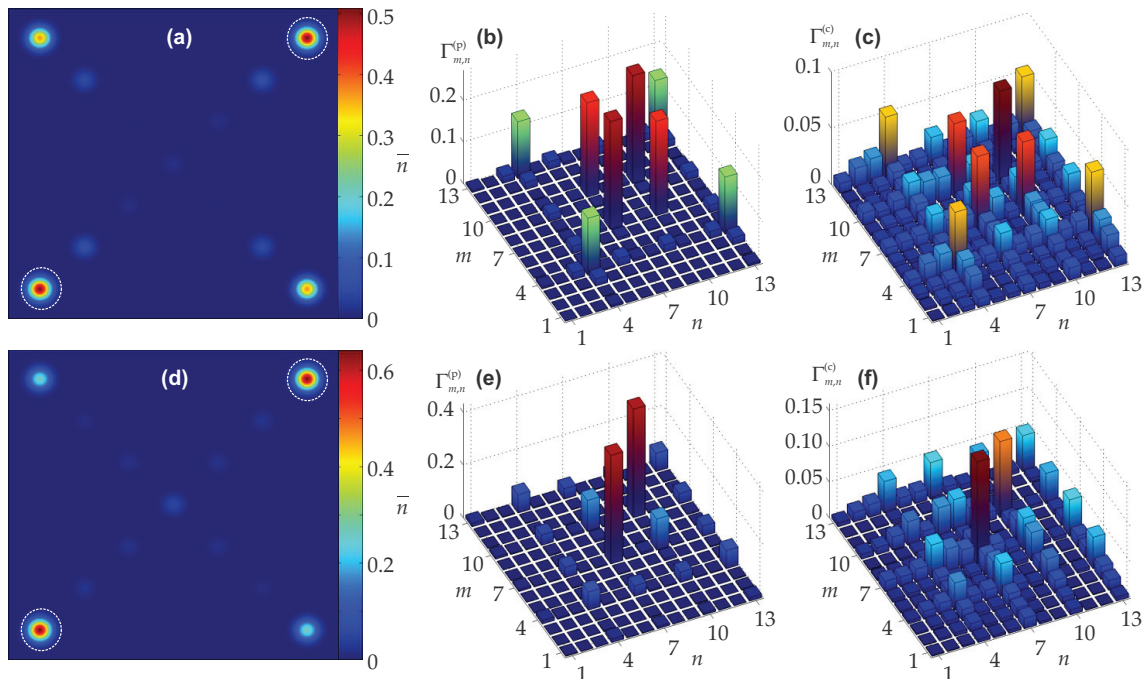


**Figure 4.2:** Two-photon evolution in the X-junction. (a) Calculated average photon number distribution at  $z = 1.37\pi/C$  for  $\beta_1 = -0.9C$  and input of the product state  $|\Psi_{7,10}^{(p)}\rangle$ . (b) Associated two-photon correlation. (c) Correlation from a classical measurement, averaged over 59 random phases. (d-f) Same as (a-c) for a positive detuning  $\beta_1 = 0.7C$  and 63 random phases. As before  $\kappa = 0.22C$ .

left inset in Fig. 2.2(b) and Fig. 2.3(c)). On the other hand, the photons evolve independently within each plane, as evident from the even height of the peaks. Hence, they behave like distinguishable particles (cf. right inset in Fig. 2.2(b)) on their plane but are highly entangled across the planes. Such a composite behaviour is not encountered in uniform 1D arrays and a direct consequence of the 2D-geometry.

As introduced in chapter 3.1, the correlation function of product states can be classically estimated by an excitation of the lattice with two laser beams and a series of intensity measurements with random relative phases. About 60 such measurements were performed (again  $\lambda = 786$  nm) with the full interferometric setup (Fig. 3.1) and the intensities from single waveguide excitation were deducted from the phase-averaged correlation, according to Eq. (3.6). The result of this procedure is displayed in Fig. 4.2(c), clearly reproducing the major peaks and their relative heights. One notes an increased level of background compared to the ideal quantum result. This can be attributed to light leaving the sample in one of the inner waveguides (cf. Fig. 4.1(d)), as well as the finite number of random phases in the average and the larger variance of the classical scheme [62]. Hence, these measurements provide a worst-case estimate of how fabrication errors, leading to devia-

tions from the desired coupling profile, may influence the quantum interference. In this case they clearly suggest, that a waveguide lattice with the given parameters can be inscribed with sufficient precision to observe the quantum path interference across the four major output channels and the associated composite entanglement.

Now it is shown that the nature of the output correlation depends strongly on the probability for the photons to switch their plane. Fig. 4.2(**d**) shows the output photon distribution for the X-lattice with a positive central detuning, where that probability is significantly reduced<sup>2</sup>. This has a drastic impact on the correlation function: As visible in Fig. 4.2(**e**), it is now far more likely for the photons to leave the lattice in the same corner of the input plane than in different corners. Hence, they exhibit a bunching behaviour on this plane and do no longer propagate independently. The side-branch peaks are reduced in height, due to the lower amplitude in these branches. However, they still have mutually equal heights, hence the independent evolution prevails in this plane, albeit with reduced probability. Finally, there is also a limited amount of cross-correlation between the planes. The classical measurement (**f**) confirms these expectations.

In essence, the aforementioned features of the 2D-lattice are washed out, as the probability for a transition into the side branches is reduced and the system approaches an effective 1D geometry. This shows the strong impact of the dimensionality on the possible outcomes of a quantum walk.

Finally, the evolution of entangled input states  $|\Psi_{7,10}^{(e,\phi)}\rangle$  is numerically investigated for the lattice with  $\beta_1 = -0.9C$ , which exhibits the most pronounced 2D features. Again, the opposite input corners 7 and 10 are considered. As discussed in chapter 2.2.3, the average photon number is identical for all types of two-photon input states, so the photon distribution for the entangled states is exactly as shown in Fig. 4.2(**a**). The correlation of the symmetric entangled state ( $\phi = 0$ ) presented in Fig. 4.3(**a**) is very similar to the one of the product state (cf. Fig. 4.2(**b**)), with some miniscule differences at the inner peaks. However, the antisymmetric state ( $\phi = \pi$ ) exhibits a fundamentally different correlation pattern (Fig. 4.3(**b**)). In this case, antibunching across the planes is expected, as evident from the location of the major peaks<sup>3</sup>. This means the photons will never be detected on the same plane. On the other hand, all the peaks have equal height, so there is no preference whatsoever for particular configurations which satisfy that requirement. Hence, there is no further correlation besides the antibunching across the planes.

Again, these two correlation functions show the mixture between entanglement and in-

<sup>2</sup> $\bar{n}_4 = \bar{n}_{13} \approx 0.25$  compared to  $\bar{n}_7 \approx \bar{n}_{10} \approx 0.65$

<sup>3</sup>Here,  $\Gamma_{4,7}^{(p)} \gg \Gamma_{4,4}^{(p)}, \Gamma_{7,7}^{(p)}$ , etc.

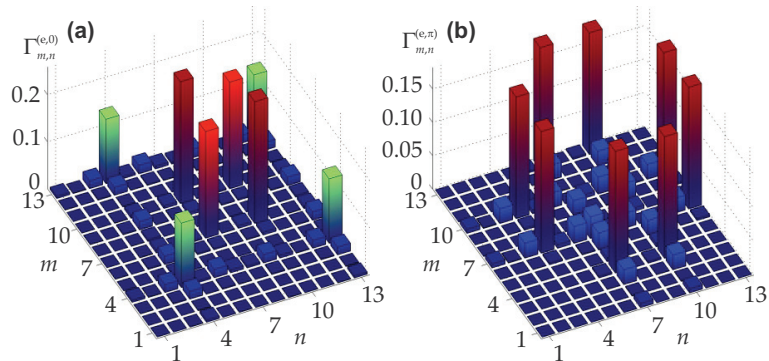


**Figure 4.3:** Calculated correlation for entangled input states  $|\Psi_{7,10}^{(e,\phi)}\rangle$  in the X-junction with  $\beta_1 = -0.9C$ . (a) Symmetric input state  $\phi = 0$ . (b) Antisymmetric state  $\phi = \pi$ . All other parameters are as before.

dependence which is made possible by the two-dimensionality of the lattice. One may notice that while here the symmetric entangled state evolves very similar to the product state and the antisymmetric state exhibits antibunching, the situation is opposite in the 1D-array (see Fig. 2.3(c-e)). This illustrates the complex dependence of the photon correlations on both, the coupling properties of the lattice as well as the character of the input state.

## 4.2 Direct measurement on a photonic chip

The remainder of this chapter is devoted to the experimental implementation of a correlated QRW in a 2D waveguide lattice. As before, the X-junction is considered as a prototypic representative of such a non-planar system. A number of challenges has to be overcome in order to make the laser-written waveguide lattice suitable for measurements with true quantum light. This will be discussed in the following section. The actual quantum measurements will then be presented in the section thereafter.

### 4.2.1 Lattice interfacing and polarisation control

To maintain the highest possible degree of indistinguishability throughout the propagation in the waveguides, it is imperative that the polarisation of the photons is maintained. As shown earlier in Fig. 2.4(b), the laser-written waveguides support two linearly polarised modes oriented along the principal axes of the elliptical refractive index profiles. Only these two polarisations, H- and V-polarisation are conserved during the propagation in an isolated waveguide, whereas any superposition is subjected to a polarisation rotation due to birefringence (see chapter 2.3). So the polarisation of the signal and idler photons must always be aligned to one of the two principal axes.

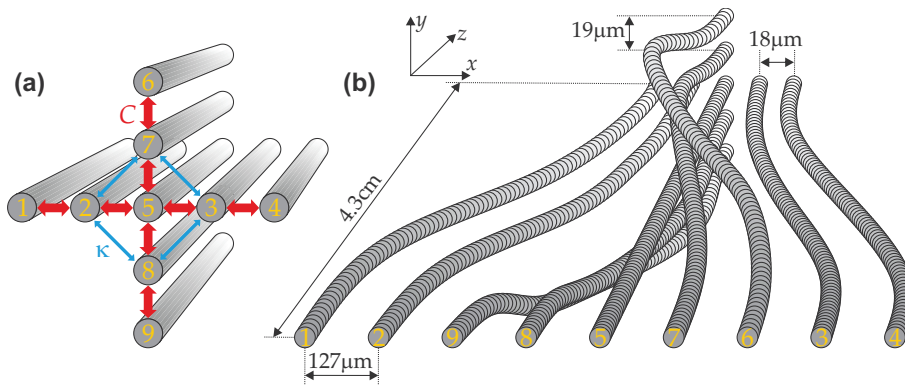
Moreover, if two or more waveguides are inscribed close enough together to allow evanescent coupling, the associated stress fields start to overlap [87]. As long as the waveguides are aligned along their principal axes, the axes of polarisation eigenmodes remain, thus still conserving H and V-polarisation. However, for any diagonal alignment, the stress fields overlap in a more complex way which distorts this property. Then the polarisation launched into a single waveguide at the input of the device is no longer maintained within the lattice<sup>4</sup>. This heavily degrades the indistinguishability of the photons and inhibits the observation of quantum interference. Therefore, the X-geometry used in the previous section has to be rotated by  $45^\circ$  to a ‘swiss cross’ arrangement of the waveguides. A preliminary measurement in such a swiss cross lattice yielded a substantial improvement with H and V polarisation being relatively well maintained again in comparison to an X-lattice of the same dimensions and coupling properties<sup>5</sup>.

Fig. 4.4(a) shows a swiss cross lattice composed of 9 waveguides with coupling strength  $C$  between nearest neighbours and second-order coupling  $\kappa$ , being isomorphic to the X-lattices from the previous chapter. Such a lattice has been realised in fused silica with the writing parameters  $E_p = 200$  nJ and  $v_0 = 1.33$  mm s<sup>-1</sup>. Each waveguide is inscribed twice to reduce propagation losses (see chapter 2.3). The ellipticity of the waveguides leads to a slight anisotropy of coupling strengths, which can be compensated by varying the waveguide separation in one axis. For H-polarisation (which will be used in the following) and horizontal (vertical) pitches of 18(19)  $\mu\text{m}$ , an approximately even coupling of  $C \approx 1.1$  cm<sup>-1</sup> is achieved in both directions.

The swiss cross has to be mapped onto the large-pitch 1D array, as required for the interfacing with photon sources and detectors via fiber arrays (cf. Fig. 2.5(c)). To this end, curved waveguide segments are used which connect the two geometries. However, there are several constraints for the waveguide trajectories in this mapping procedure: First, one has to make sure that the waveguides never intersect as this would involve undesired losses and cross-talk between the channels. Second, the coupling between the curved waveguides should be minimised and only occur between guides which are also coupled in the lattice, in order to preserve the topology of the system. Hence, the waveguides should maintain an appreciable distance between each other, anywhere except during the final approach. Finally, the bending radii should be kept as large as possible, i.e., the

<sup>4</sup>A conversion from pure H or V-polarisation to an almost even mixture of both polarisations (45% of the intensity in the respective orthogonal polarisation) was found in an X-lattice of 9 waveguides with a length of 2.3 cm and a waveguide separation of 17.5  $\mu\text{m}$ , having similar coupling properties at  $\lambda = 800$  nm as the ones presented in section 4.1.

<sup>5</sup>The intensity fraction of the orthogonal polarisation was 6% and 2.5% for input of H and V, respectively.



**Figure 4.4:** Swiss cross lattice for single photon experiments. **(a)** Lattice of 9 sites with first and second-order couplings  $C$  and  $\kappa$ , respectively. Sites 1 to 4 are aligned along the  $x$ -axis, 5 is the central waveguide and elements 6 to 9 compose the vertical branches. **(b)** Fanning region mapping this lattice to a 1D array with  $127\mu\text{m}$  pitch. The waveguide trajectories are designed to avoid crossings and allow coupling only between adjacent guides in the final stage of the approach.

overall curvature be kept to a minimum, to avoid large bending losses. A compromise between these requirements is illustrated in Fig. 4.4**(b)**, satisfying the latter requirement by aligning the centres of the swiss cross and the 1D array (guide no. 5). The other two conditions are met by fanning the guides in the vertical branches (6 to 9) to twice the vertical separation required in the 2D structure ( $38\mu\text{m}$  in this case) before they are horizontally shifted and then brought to their final position [88]. The whole fanning is implemented on a length of  $\Lambda \approx 4.3\text{cm}$  for the input as well as for the output end, leaving  $L = 1.4\text{cm}$  propagation length in the lattice available for the photons. Each curved segment follows a harmonic trajectory. For a curvature in the  $x - z$  plane, the profile is  $x(z) = \frac{A_x}{2} \left[ 1 - \cos\left(\frac{\pi z}{\Lambda_x}\right) \right] + x(0)$ , with  $A_x$  denoting the total transverse shift in the  $x$ -direction and  $\Lambda_x$  the length on which this shift is implemented. This profile has been found to entail losses growing linearly with  $A_x$  [29]. The same type of profile is used for the vertical curvature  $y(z)$ .

A detailed analysis of the losses was performed after a final cleaving of the sample following the quantum measurements (see next section) and is now presented. The front and rear ends of the sample containing the two fanning regions between the lattice and the fiber arrays were cut from the glass chip and polished. Fig. 4.5**(a)** shows a microscope image of one of the outer end faces, with all 9 waveguides aligned in one plane and separated by  $127\mu\text{m}$ . The swiss cross shape of the lattice can be seen on the inner end of a fanning segment **(b)**. Each of the waveguides has been excited at the large-pitched end with H-polarised laser light at  $\lambda = 810\text{nm}$  (again using a single arm of the Mach-Zehnder setup Fig. 3.1). The power before and after the sample are monitored by photodiodes.

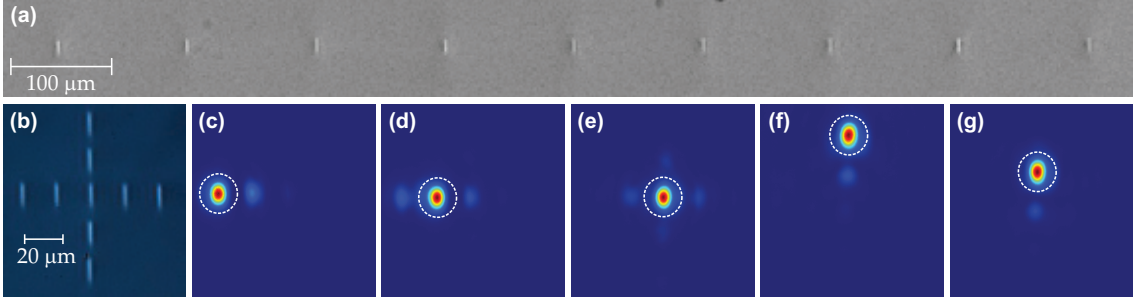


**Figure 4.5:** (a) Microscope image of the glass chip end face with the waveguides being arranged in a 1D array with  $127\ \mu\text{m}$  pitch. (b) Microscope image at the inner end of the fanning segment, where the waveguides are aligned in a swiss cross lattice. (c-g) Observed intensity output distribution at the inner side for an excitation of waveguides 1, 2, 5, 6 and 7 at the 1D endface.

Scattered light is excluded from the power measurement behind the sample by carefully aligned apertures. The limited excitation efficiency due to the finite overlap between the intensity profile in the focus of the incoupling objective and the waveguide mode is taken into account by measuring both profiles on the CCD. Also, Fresnel reflection losses at the sample surface as well as losses from the objectives and the other components of the setup are considered. The remaining difference between output and input power can then be attributed to propagation loss in the waveguide.

An effective propagation loss coefficient for the curved sections is calculated from dividing the total propagation loss by the length of the waveguide and averaging over the two fanning segments from the input and the output of the device. Table 4.1 compiles these effective losses of all waveguides together with their horizontal(vertical) bending amplitudes  $A_{x(y)}/\Lambda_{x(y)}$ .

| waveguide                                   | 1    | 2    | 3    | 4    | 5    | 6    | 7    | 8    | 9    |
|---|------|------|------|------|------|------|------|------|------|
| $A_x/\Lambda_x$ [ $\mu\text{m}/\text{cm}$ ] | 111  | 85   | -85  | -111 | 0    | -86  | -43  | 43   | 86   |
| $A_y/\Lambda_y$ [ $\mu\text{m}/\text{cm}$ ] | 0    | 0    | 0    | 0    | 0    | 86   | 43   | -43  | -86  |
| effective loss [dB/cm]                      | 0.99 | 0.87 | 1.15 | 1.26 | 0.72 | 1.12 | 0.82 | 0.94 | 1.32 |

**Table 4.1:** Measured propagation losses and bending amplitudes in the curved waveguide segments. The bending amplitude  $A_{x(y)}/\Lambda_{x(y)}$  is the total transverse shift in horizontal (vertical) direction divided by length of the corresponding curved segment. The effective loss is averaged over the full length of the waveguide and both fanning elements.

It should be noted, that the waveguides with vertical curvature are bent in  $x$ - and  $y$ -direction subsequently, hence only one type of curvature occurs at a time. As expected, the smallest loss of about  $0.7\ \text{dB}/\text{cm}$  is observed in the straight waveguide. The largest loss of about  $1.3\ \text{dB}/\text{cm}$  occurs for waveguide 9, amounting to an intensity transmission of about 27% through each of the fanning segments. From these values it is furthermore evident that H-polarised light incurs more losses from vertical bending than from horizontal

bending. Interestingly, the losses seem also to depend on the direction of the curvature. Here, a bending to the right (positive  $x$ ) induces less loss than to the opposite direction and downwards bending (negative  $y$ ) is associated to more loss than a corresponding upwards curvature. As far as bending in a single direction is concerned, the losses grow with the bending amplitude. These loss values will be taken into account in the analysis of the QRW discussed in the next section.

In order to quantify the influence of the additional coupling during the approach of the waveguides, a single fanning segment with identical parameters was fabricated and characterised by exciting the waveguides at the 1D-interface. The intensity distributions at the 2D-end are shown in Figs. 4.5(c-g) for all types of waveguides<sup>6</sup>. From these images it can be seen that most of the light remains in the input guide and only about 10...20% of the power leaks into the adjacent channels. This means that a significant coupling only occurs between guides which are also coupled in the lattice, as it is required from the design of the fanning element. A comparison to numerical simulations shows that the amount of light transferred to the adjacent sites corresponds to effective coupling strengths of  $C_{\text{fan}} \approx 0.05 \dots 0.1 \text{ cm}^{-1}$ , averaged over the whole length  $\Lambda$  of the curved waveguides. As the actual coupling in the inner lattice of length  $L = 1.4 \text{ cm}$  is  $C \approx 1.1 \text{ cm}^{-1}$ , the additional coupling from the two fanning segments can be modelled by enlarging the effective coupling strength of the inner lattice to  $C_{\text{eff}} = C + 2\Lambda L^{-1}C_{\text{fan}} \approx 1.4 \dots 1.7 \text{ cm}^{-1}$ . These are the right dimensions to localise the photon amplitude in the outer waveguides of a cross of 9 sites, when one of the corners is excited. Hence, this device can be expected to support an observation of the effects introduced in the previous section.

### 4.2.2 Observation of a two-dimensional quantum walk

In the following, the observation of a two-photon QRW in the swiss cross lattice will be presented. The measurements, simulations and data analysis were carried out in cooperation with the University of Bristol [88].

The photon source was a type-I phase matched (cf. Fig. 2.5(a)), 2 mm thick  $\text{BiB}_3\text{O}_6$ -crystal, which was pumped by a 60 mW continuous wave laser diode operating at  $\lambda_p = 404 \text{ nm}$ . The H-polarised photon pairs with  $\lambda_s = \lambda_i = 808 \text{ nm}$  were spectrally narrowed by interference filters with a 3.1 nm wide transmission window centered around  $\lambda_s$  and coupled into polarisation-maintaining fibers. Subsequently, fiber arrays as shown in Fig. 2.5(c) were employed to interface the photons with the glass chip carrying the waveguides, and to transmit the output photons to SPCMs [89]. The waveguide fabrica-

---

<sup>6</sup>Corner waveguide and inner waveguide of horizontal and vertical branch as well as the centre



tion parameters and the lattice geometry have been described in the previous section, as well as the structure of the fanning region which is used to connect the lattice to the fiber arrays (see Fig. 4.4).

As input states, an excitation of corner waveguides in branches of the same plane (sites 1 and 4, see Fig. 4.4(a)) as well as an excitation of different planes (1 and 6) were chosen. In both cases, a single photon entered each of the two waveguides, thus the photon pair was initialised in a product state (cf. Eq. (2.24)). The setup included an adjustable delay stage<sup>7</sup>, which allows to control the temporal shift between the two photons at the input of the device. Thereby, potentially different path lengths in the fanning region were compensated and the temporal overlap of the photon wavepackets in the lattice, and hence their indistinguishability, was tuned. For relative delays larger than the coherence length of the photons, an independent propagation of the individual photons is expected, whereas a perfect overlap in time should lead to a maximum-visibility quantum path interference. In order to calibrate the delay and to characterise the visibility of the quantum interference, the following experiment is conducted.

A remarkable feature of the quantum path interference of two-photon product states in any unitary network is the doubling of on-diagonal elements of the correlation matrix  $\Gamma^{(p)}$  compared to the classical case of fully distinguishable particles [90]. An illustrative example is the Hong-Ou-Mandel experiment, where clearly  $\Gamma_{k,k}^{(p)} = 2\Gamma_{k,k}^{(d)}$ , with  $k = 1, 2$ , holds for perfect indistinguishability in the dip (see Fig. 2.2(b)). In fact, the visibility of the on-diagonal quantum interference

$$V_k \equiv \frac{\Gamma_{k,k}^{(p)} - \Gamma_{k,k}^{(d)}}{\Gamma_{k,k}^{(d)}}$$

is entirely independent of the properties of the network, such as coupling distribution or evolution length. Hence, this visibility serves as a measure for the degree of photon indistinguishability which is achieved by the employed photon source in the investigated network, with  $V_k = 1$  for perfect indistinguishability at the optimum overlap. Conversely, any effects degrading the quantum interference, either due to imperfections of the source or due to decoherence or polarisation conversion in the waveguides will be reflected in a reduced visibility.

To characterise the strength of the quantum path interference in the swiss cross device the two-photon coincidence rate in output waveguide 3 is monitored for an input into opposite corners (sites 1 and 4). As the photon detectors cannot resolve the photon number, a

---

<sup>7</sup>One of the fiber input coupling stages is translated longitudinally, changing the optical path length for one photon.

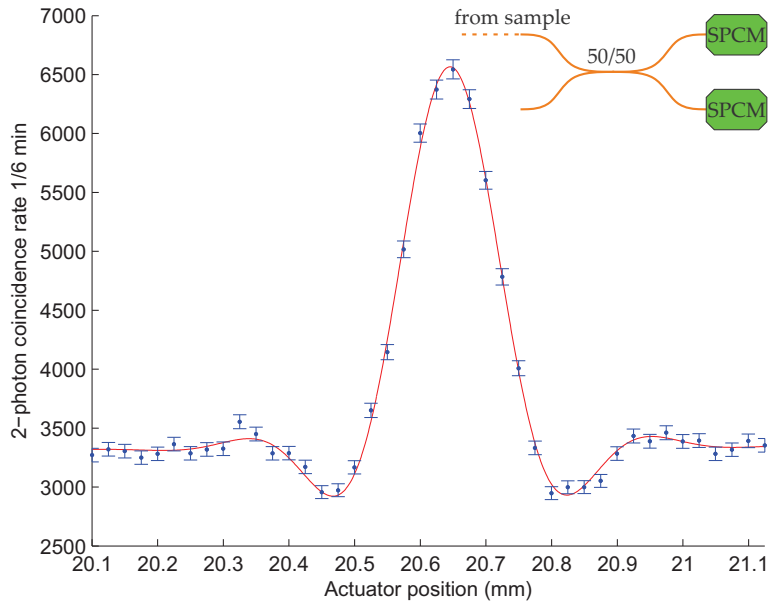


**Figure 4.6:** Measured coincidence rate in output channel 3 for an input of photons into guides 1 and 4 in dependence of the delay position. The error bars indicate the standard deviation of the underlying Poissonian photon counting statistics and the red line is a best fit to the data taking the non-Gaussian spectral shape of the interference filter into account [91]. The inset shows a scheme of the probabilistic detection method using a balanced fiber splitter. Main image taken from [88].

probabilistic detection technique is employed: The fiber which is attached to the output waveguide is connected to one input port of a 50/50 fiber splitter<sup>8</sup>. As discussed in chapter 2.2.3, when two photons are incident in the same channel, they propagate independently through the coupler, like Bernoulli trials, splitting with a probability of 50% into both output channels which feed into SPCMs (inset of Fig. 4.6). Then, a two-photon event in the input channel is detected as a coincidence between the two detectors with a chance of 50%. The main graph in Fig. 4.6 displays the measured coincidence rate in dependence of the (single-pass) delay line position, with an integration time of 6 min at each data point. The raw data has been multiplied by two, accounting for the probabilistic nature of the detection, and corrected for differences in the efficiencies of the detectors. One clearly sees how the coincidence rate is increased as the photons overlap in time. The width of the peak (full width half maximum  $\approx 150 \mu\text{m}$ ) corresponds to a duration of  $\approx 500$  fs of the photon wavepackets. One can infer the visibility of the quantum path interference from the maximum value of the peak and the coincidence rate at full distinguishability to  $V_3 = (96.8 \pm 2.5) \%$ . This demonstrates the high degree of indistinguishability which can be reached with the setup in the given sample and the resilience of the quantum interference to the residual polarisation conversion in the waveguides.

<sup>8</sup>The fiber version of the 50/50 coupler introduced in chapter 2.2.2

The QRW in the swiss cross lattice is characterised for the input configuration where both photons start in opposite corners of the same plane  $(k, l) = (1, 4)$  as well as for an excitation of the corners of perpendicular planes  $(k, l) = (1, 6)$ . Both scenarios have been investigated for fully distinguishable photons, i.e., with a large relative delay of the photons, and for maximum overlap. The probability of coincidence  $P_{m,n} = \frac{1}{1+\delta_{m,n}}\Gamma_{m,n}$  in waveguides  $m$  and  $n$  has been estimated for each setting by counting all coincidence events occurring within one hour, resulting in the count distribution  $\mathcal{N}_{m,n}$ . Again, a probabilistic detection employing fiber splitters is used to measure the on-diagonal elements ( $m = n$ ). Fig. 4.7(a) displays the resulting count distributions for the out-of-plane input of distinguishable, independently evolving, photons. Typical count rates are in the order of  $10^4$  events during the integration time. Photon counting is subject to a Poissonian statistics<sup>9</sup>, with the square root of the count rate as standard deviation [54]. Hence, the uncertainty from the counting statistics is in the order of  $\sqrt{\mathcal{N}} \sim 100$  counts for the peaks of the distribution, which is negligible compared to their height.

One can identify four sectors in the plot: Two areas belong to events where both photons occupy either the x- or y-plane together ( $\mathcal{N}_{1-4,1-4}$ ,  $\mathcal{N}_{6-9,6-9}$ ) while the other two sectors ( $\mathcal{N}_{1-4,6-9}$ ,  $\mathcal{N}_{6-9,1-4}$ ) represent events at which the photons are detected in different planes. One notices considerable coincidence probabilities in all 4 sectors. Hence, the photon evolution cannot be explained as a simple superposition of two 1D quantum walks. Instead both spatial dimensions are engaged by both photons, amounting to true 2D dynamics.

The picture changes significantly when the photons are overlapped in time. Fig. 4.7(b) shows the coincidence counts for indistinguishable photons where a redistribution of several peaks can be observed. The increase of all on-diagonal elements, as it is expected for a quantum path interference (cf. Fig. 4.6), is clearly visible. Also some other detection events change considerably. For instance, the four peaks  $\mathcal{N}_{1,5}^{(d)}$ ,  $\mathcal{N}_{1,7}^{(d)}$ ,  $\mathcal{N}_{3,5}^{(d)}$  and  $\mathcal{N}_{3,7}^{(d)}$  occurring for distinguishable photons indicate that if one photon occupies channels 1 or 3 it is likely for the other to be found in 5 or 7. These peaks have roughly the same height, suggesting that these possibilities are mutually uncorrelated. In the case of identical photons, however, these events are no longer independent, but highly correlated as evident from the enlarged peaks  $\mathcal{N}_{1,5}^{(p)}$  and  $\mathcal{N}_{3,7}^{(p)}$ , meaning that the pair tends to occupy either 1 and 5, or 3 and 7, but not the other two combinations which would be in principle allowed by the individual photon trajectories.

To quantify the strength of the correlation in the evolution dynamics it is useful to calcu-

---

<sup>9</sup>For a constant photon flux, which is a very reasonable assumption over such a long integration time.

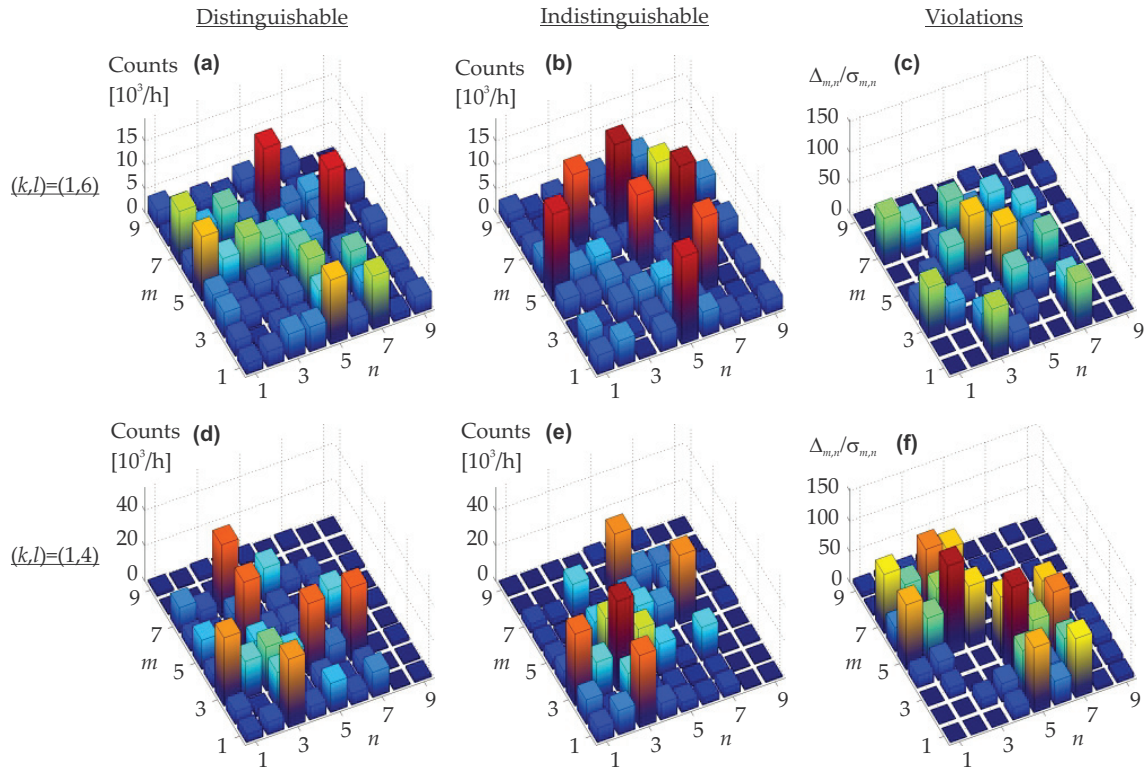


**Figure 4.7:** Observation of a QRW in the swiss cross lattice. Shown are the measured coincidence rates for distinguishable photons (left) and indistinguishable photons (centre) for out-of-plane input (a,b) and in-plane input (d,e). The on-diagonal count rates have been doubled to account for probabilistic detection and all elements have been corrected for relative detector efficiencies. The right column (c,f) displays violations of inequality (4.1) by the indistinguishable photons, measured in standard deviations as obtained from the underlying Poissonian photon counting statistics. Only positive values of the violations are shown.

late the violations of an inequality which must hold for distinguishable photons. It can be shown that their coincidence probabilities must always obey the inequality (see Appendix A.2 for a derivation)

$$2\sqrt{P_{m,m}^{(d)}P_{n,n}^{(d)}} - P_{m,n}^{(d)} \leq 0, \quad (4.1)$$

for  $m \neq n$ . This means that the on-diagonal elements of the probability matrix (corresponding to both photons occurring in the same channel) cannot exceed a certain bound given by the associated off-diagonal elements. Hence a breach of this bound is a sufficient criterion for a correlated evolution of the photons in the regime of bunching.

The left hand side of this inequality has been evaluated for the count distribution of the indistinguishable photons:  $\Delta_{m,n} \equiv 2\sqrt{\mathcal{N}_{m,m}^{(p)}\mathcal{N}_{n,n}^{(p)}} - \mathcal{N}_{m,n}^{(p)}$ . Positive values of  $\Delta_{m,n}$  indicate a violation of the inequality (4.1). To quantify the statistical significance of such violations it is necessary to compare them to the uncertainty arising from the counting statistics. Therefore the values  $\Delta_{m,n}$  are normalised with respect to their uncertainties

$\sigma_{m,n}$  which are calculated from the standard deviations of the count rates (see Appendix A.2 for details).

Fig. 4.7(c) displays the violations calculated from the measured data for an excitation of orthogonal planes. It clearly shows strong signatures of photon bunching across many combinations of waveguides. The largest violations of up to about 100 standard deviations are found where the off-diagonal elements  $\mathcal{N}_{m,n}^{(p)}$  are strongly reduced compared to  $\mathcal{N}_{m,n}^{(d)}$ . In these cases, it is very unlikely for the photons to occupy channels  $m$  and  $n$  separately, instead they bunch in one of them, forming a path-entangled state.

The corresponding correlations and violations for an in-plane excitation are shown in Figs. 4.7(d-f). Also for this input state one finds a clear trace of quantum path interference, as heralded by the increased on-diagonal elements of the correlation function for indistinguishable photons as well as the presence of strong violations reaching nearly 150 standard deviations.

A noteworthy exception are the waveguides of the lower branch (8 and 9), where only miniscule violations occur. This is related to the low probability of any photon being detected in this branch at all<sup>10</sup>. Also intensity measurements with classical light reveal that almost no light remains in these waveguides. In part, this is due to the relatively large bending losses which the light incurs in the lower guides (see Table 4.1). The dominant reason is, however, the fact that very little light couples into the lower branch in the first place. This is most likely due to a weakened coupling  $C_{5,8} < C$  between guides 5 and 8, as suggested by simulations (see later) and supported by a careful analysis of the microscope image Fig. 4.5(b), which reveals that the separation of these two waveguides is roughly 1  $\mu\text{m}$  larger than between the other guides. On the other hand, the gap between 5 and 7 is about 1  $\mu\text{m}$  smaller, leading to an enlarged coupling  $C_{5,7} > C$  into the upper branch.

Another striking feature of the distribution of violations for this input configuration is the near absence of violations in the sectors corresponding to detection of the photons in the same plane, whereas strong violations occur in the sectors corresponding to detection across the planes as well as in the central row and column. This suggests that both photons tend to occupy either the horizontal plane (without the centre) or the upper branch and centre together, but exhibit no bunching behaviour within these two areas. This is the composite behaviour of entanglement and independence, which has been predicted for the cross-topology (cf. Fig. 4.2(b)) [62].

In order to visualise the relation between the branches more clearly, it is helpful to sum the coincidences over the waveguides within each branch. In that, the network

---

<sup>10</sup> $\mathcal{N}_{8,n}$  and  $\mathcal{N}_{9,n}$  nearly vanish for all  $n$ .

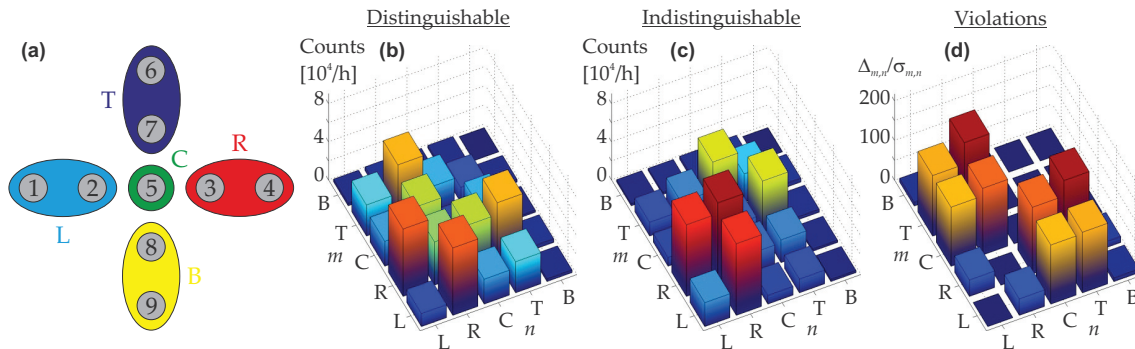


**Figure 4.8:** (a) Branches of a swiss cross waveguide lattice. (b) Measured distribution of coincidence counts among the branches for distinguishable photons and  $(k, l) = (1, 4)$ . (c) Same for photons with optimum temporal overlap. (d) Corresponding violations of inequality (4.1) in standard deviations.

is effectively reduced to the five areas left ('L'), right ('R'), top ('T'), bottom ('B') and centre ('C'), as indicated in Fig. 4.8(a). The coincidences of the in-plane input state are summed according to this scheme<sup>11</sup>. The resulting coincidence counts for distinguishable and indistinguishable photons as well as the violations of inequality (4.1), are displayed in Figs. 4.8(b-d). The previous observations are corroborated by these plots: From the absence of counts in the last row and column, it is evident that the lower branch B is essentially decoupled from the remaining lattice. On another note, the large violations (reaching up to 200 standard deviations) between branches L and R on one side and C and T on the other, demonstrate clearly that the photon pair is located either in the input branches or in the vertical branch (which includes the centre). However, with the exception of a weak violation between L and R, no further violations are visible, suggesting that the pair evolves almost independently within these two areas. This behaviour is reflected in the resilience of the off-diagonal peaks  $\mathcal{N}_{L,R}^{(p)}$  and  $\mathcal{N}_{C,T}^{(p)}$  in the coincidence pattern of the indistinguishable photons (c), whereas the other off-diagonal elements are strongly suppressed.

Finally, the experimental results are compared to numerical calculations. In order to separate the classical transfer properties of the waveguide lattice from other effects which may influence the quantum interference (photon source, photon indistinguishability, detectors, etc.), the output intensity distributions resulting from a classical excitation of the central guide as well as all four corner sites with laser light ( $\lambda = 810$  nm, H-polarisation)<sup>12</sup> were measured. These intensity patterns arise from the length of the lattice (1.4 cm), the

<sup>11</sup>On- and off-diagonal terms constitute from three and four possibilities, respectively, e.g.,  $\mathcal{N}_{L,L} = \mathcal{N}_{1,1} + \mathcal{N}_{2,2} + \mathcal{N}_{1,2}$  and  $\mathcal{N}_{L,R} = \mathcal{N}_{1,3} + \mathcal{N}_{1,4} + \mathcal{N}_{2,3} + \mathcal{N}_{2,4}$ .

<sup>12</sup>The relative deviation of the coupling strength for a spectral shift of 2 nm is estimated to be  $\approx 1\%$  [75], which is neglected here.

coupling parameters  $C$  and  $\kappa$ , as well as the loss distribution in the output fanning segment (length 4.3 cm). Furthermore, positioning errors occur during the fabrication process<sup>13</sup>, leading to site-dependent deviations of the coupling from the ideal values  $C$  and  $\kappa$ . Moreover, the waveguides affect each other via their surrounding stress fields [87]. The strength and nature of this influence depends on the location of the waveguide within the lattice and the order of inscription. Hence, a variation of the propagation constant  $\beta$  among the guides can be expected.

The most likely values for  $\beta$ ,  $C$  and  $\kappa$  are estimated by a numerical optimisation, with the 9 propagation constants and 12 couplings (see Fig. 4.4(a)) as free parameters, finding a configuration which maximises the overlap between a simulated propagation for the five excitation configurations and the respective measured intensities. In this case, a quasi-Newton method, the Broyden-Fletcher-Goldfarb-Shanno algorithm [92], is employed. The fanning losses summarised in Tab. 4.1 are taken into account in the forward simulation, whereas the losses in the straight lattice are assumed to be equal in all channels.

The optimal parameters, which result from this procedure are listed in Fig. 4.9(a). The similarity between a measured intensity distribution  $I_n$  and the forward simulation  $I_n^{(\text{sim})}$  can be quantified by a fidelity parameter [37]

$$F^{(I)} \equiv \left( \sum_{n=1}^N \sqrt{I_n I_n^{(\text{sim})}} \right)^2 / \left( \sum_{n=1}^N I_n \sum_{n=1}^N I_n^{(\text{sim})} \right). \quad (4.2)$$

With the optimal set of parameters, fidelities of  $F^{(I)} = 0.961 \dots 0.995$  have been obtained for the five intensity patterns. This and the fact that the values of these optimal parameters lie within the expectations ( $C \approx 1.5 \text{ cm}^{-1}$ ,  $\kappa \approx 0.15 \dots 0.3C$ ,  $|\beta| \lesssim |C|$ ) suggests that a plausible solution has been found which allows to model the light evolution in the lattice with reasonable accuracy. It should be noted, though, that these coupling strengths represent effective values incorporating the additional coupling in the fanning region, which has been treated as a set of isolated waveguides in the simulations. Hence, the physical values of the couplings within the lattice are lower than listed in the table. The weaker coupling  $C_{5,8} < C$ , connecting the bottom branch with the centre, and the enlarged coupling to the upper branch  $C_{5,7} > C$  fit to the corresponding displacements of the waveguides from their targeted position (cf. Fig. 4.5(b)). They seem to be the origin for the weak connection of the lower branch to the remaining lattice, which manifests itself in the absence of photons in this branch in the QRW (Figs. 4.7, 4.8).

The latter hypothesis is confirmed by the numerical simulation of the QRW with the op-

<sup>13</sup>The positioning precision is in the order of 0.5  $\mu\text{m}$ .

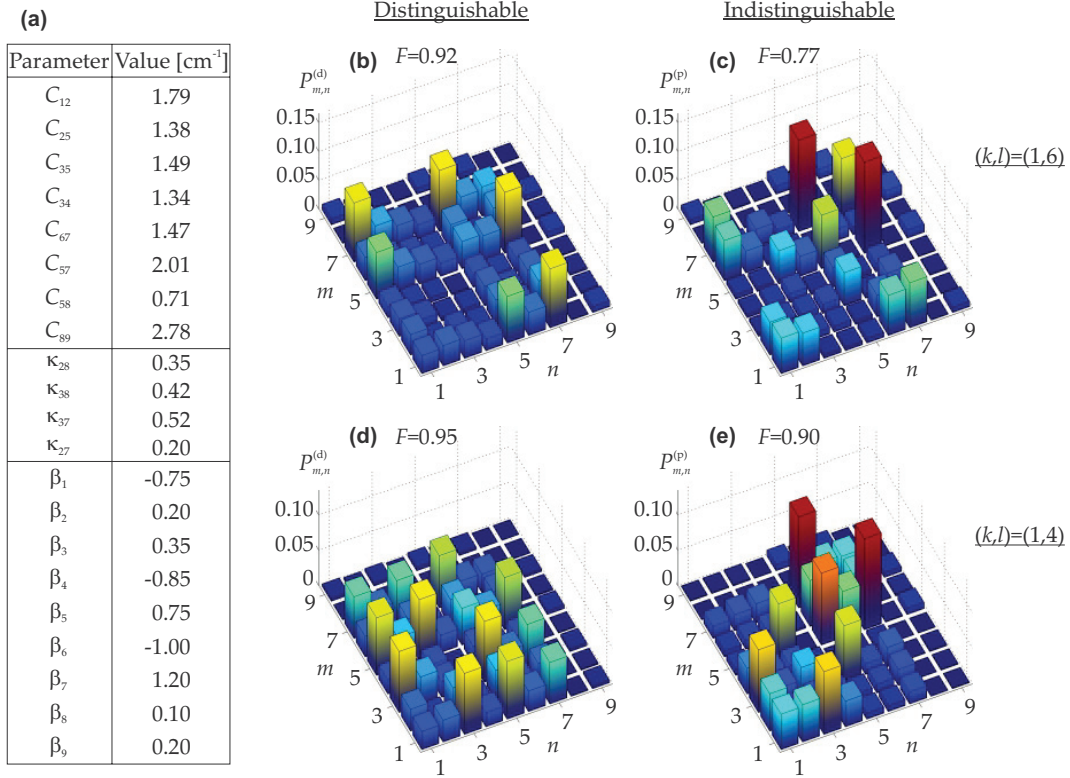


**Figure 4.9:** Numerical simulation of the QRW in a swiss cross lattice. **(a)** Lattice parameters obtained from independent classical intensity measurements, the loss distribution in the fanning region listed in Tab. 4.1 and subsequent numerical optimisation. The waveguides and couplings are labelled as in Fig. 4.4(a). **(b-e)** Normalised coincidence probabilities for distinguishable and indistinguishable photons for both input configurations, calculated from these lattice parameters and the loss distribution. The fidelities are calculated by Eq. (4.3) and measure the similarity to the experimental data in Fig. 4.7.

timal set of lattice parameters, employing Eq. (2.27) for indistinguishable and Eq. (A.2) for distinguishable photons (see Appendix A.2). The loss distribution of Tab. 4.1 is taken into account for the fanning section after the lattice<sup>14</sup>. The results for distinguishable as well as indistinguishable photons and both input configurations (in-plane and out-of-plane) are presented in Figs. 4.9(b-e). In each case, the coincidence probabilities have been calculated and normalised to compensate loss. The empty rows and columns 8 and 9 clearly indicate that the detached behaviour of the branch B can indeed be attributed to the uneven couplings between the two vertical branches and the centre. In three of the four cases (b,d,e), the calculated probability patterns agree quite well to the measured

<sup>14</sup>The losses on the input side merely lead to global damping of the coincidence count rates. They have no influence on the relative distribution of the two-photon events.



count distributions, with fidelities

$$F \equiv \left( \sum_{m,n=1}^N \sqrt{P_{m,n} \mathcal{N}_{m,n}} \right)^2 / \left( \sum_{m,n=1}^N P_{m,n} \sum_{m,n=1}^N \mathcal{N}_{m,n} \right) \quad (4.3)$$

not below 90%. The good agreement demonstrates that the trajectories of the QRW, for distinguishable as well as for indistinguishable photon pairs, are essentially controlled by the coupling properties of the waveguide lattice and a high degree of coherence is maintained throughout the evolution. The slight reduction in fidelity from the classical single-waveguide excitation (the values for  $F^{(1)}$  quoted above) to the distinguishable photon measurement (**b,d**) can be attributed to the additional uncertainties arising in the quantum experiment, such as varying coupling efficiencies into the optical fibers and the non-zero photon bandwidth. In case of indistinguishable photons the fidelity is further reduced by limitations in the visibility of the quantum interference. The relatively poor fidelity for maximum-overlap photons in the out-of-plane configuration (**c**) seems to originate mostly from a mismatch of the peaks associated to events where one of the photons is detected in channels 1 or 3. In principle, this could be due to an unknown source of distinguishability in these waveguides being effective only for this particular input configuration. However, this seems rather unlikely as strong violations of inequality (4.1) are still observed in the experimental data and the on-diagonal elements of the count distribution for temporally overlapped photons nearly double in height compared to delayed photons (cf. Fig. 4.7(**a-c**)). On the other hand, the lower fidelity could merely arise from errors in the numerical optimisation which happen to shift the peaks between adjacent channels in this setting. At least the general shape of the distribution is clearly reproduced by the simulation<sup>15</sup>, which suggests that slightly different coupling parameters may produce a significantly better agreement. Hence, the coherence and the indistinguishability of the photons seem to be unaffected also for the out-of-plane excitation, which means that the dynamics of the photon evolution is chiefly governed by the topology and the coupling properties of the lattice.

These results demonstrate how a 2D waveguide network can be utilised to control the behaviour of photons in a correlated QRW. The possible paths of the photons traverse both spatial dimensions and allow for a multitude of quantum path interferences for appropriately chosen lattice configurations and input states. The non-planar geometry of the crossed network, exemplarily investigated here, triggers the genesis of intricate output

---

<sup>15</sup>The four peaks in channels 5 and 7, the ridge from  $\mathcal{N}_{1,6}$  via  $\mathcal{N}_{5,5}$  to  $\mathcal{N}_{6,1}$  and the three peaks in guides 1 and 2.

states which contain features of both, path-entanglement and independence. Such a behaviour is not encountered in 1D configurations and illustrates how the additional spatial degree of freedom enhances the complexity of the quantum walk without the necessity of an increased number of quanta in the system.

## 5 Glauber-Fock lattices

In the previous chapter, the second transverse spatial dimension was utilised in order to enrich the quantum walk of two indistinguishable particles in comparison to the QRW on a uniform planar lattice. Another route towards a more diverse spectrum of trajectories, beyond the usual ballistic paths occurring in a uniform 1D lattice, is a variation of the lattice properties along its transverse direction. Examples are the Bloch oscillations in lattices with a linear index gradient [93], Anderson localisation in disordered arrays [94] and the dynamics in lattices with a periodic modulation of losses [66]. If furthermore the shift-invariance of the lattice is broken, the evolution of a quantum state will depend not only on the relative distance between the input guides, but also on the absolute position within the lattice.

In this chapter, a particular example of a non-shift-invariant coupling distribution is considered. Specifically, the coupling in this semi-infinite Glauber-Fock lattice grows with the square root of the transverse waveguide coordinate [95]. In this analytically solvable system one finds a rich family of two-particle correlations which are highly characteristic of the type as well as the initial position of the input state [96]. The QRW of indistinguishable particles in such lattices will be investigated in detail in the second section.

In the precursing section, the single-particle dynamics in these systems, which is readily accessible by classical light excitation with a single beam, is studied. It turns out that the light evolution in these lattices is analogous to the behaviour of Fock states when overlaid with a coherent field [97, 98]. To date, this displacement of Fock states has not been observed directly and only been implemented for the lowest-order Fock states, due to the difficulty of generating pure higher-order number states [99, 100]. On the other hand, the order of the Fock state translates to the transverse waveguide coordinate in the lattice without any fundamental limit to the quantum number. At the same time, the light evolution can be directly monitored by fluorescence microscopy techniques [29]. In this sense, the classical light evolution in a Glauber-Fock lattice serves as a compact and controllable optical emulator of the Fock state displacement in phase space [96].

## 5.1 Displaced Fock states and their classical emulator

At first the properties of Fock states, coherent states and displaced Fock states are briefly reviewed.

As introduced in chapter 2.1.2, the eigenstates of the harmonic oscillator Hamiltonian (2.10), termed Fock states, form a ladder with equidistant energy separation which is ascended (descended) by the creation (annihilation) operators as described in Eq. (2.11). In optics, these states quantify the number of photons in a given mode; the state  $|n\rangle$  carries exactly  $n$  photons. However, the Fock states have a completely random phase [53, 54].

A coherent beam of light, on the other hand, is associated to a complex field amplitude  $\alpha$  with well defined phase, but contains an undetermined number of photons. Its quantum state can be formally derived as eigenstate of the annihilation operator  $\hat{a}$  with eigenvalue  $\alpha$ :  $\hat{a}|\alpha\rangle = \alpha|\alpha\rangle$ . The intuition behind this approach is the following: The annihilation operator  $\hat{a}$  represents, in essence, the operator of the electric field (see chapter 2.1). Hence, the state of a coherent light beam with its well defined field should be an eigenstate of  $\hat{a}$ . The outcome of this approach is the coherent state which can be expanded in the Fock basis as [52]:

$$|\alpha\rangle = e^{-\frac{|\alpha|^2}{2}} \sum_{n=0}^{\infty} \frac{\alpha^n}{\sqrt{n!}} |n\rangle. \quad (5.1)$$

This implies that the probability to detect  $n$  photons in a coherent mode is given by a Poissonian distribution with expectation value  $|\alpha|^2$ .

The relation to classical fields can be best understood in phase space: The conjugated variables of the oscillator  $\hat{Q}$ ,  $\hat{P}$  (see chapter 2.1) essentially correspond to the real and imaginary parts of the electric field in the optical mode. Hence, the coherent state with amplitude  $\alpha$  has a mean position in phase space  $(\langle\hat{Q}\rangle, \langle\hat{P}\rangle)$  which is given by  $\alpha = (2\hbar/\omega)^{-\frac{1}{2}} \langle\hat{Q}\rangle + i(2\hbar\omega)^{-\frac{1}{2}} \langle\hat{P}\rangle$ . Clearly, the exact position cannot be determined as required by the Heisenberg uncertainty principle. However, one can show that for all coherent states  $\Delta\hat{Q}\Delta\hat{P} = \hbar/2$  holds, meaning that they are minimum-uncertainty states [54, 55]. Importantly, this uncertainty is independent of  $\alpha$ . Hence, the relative uncertainties  $\Delta\hat{Q}/\langle\hat{Q}\rangle$  and  $\Delta\hat{P}/\langle\hat{P}\rangle$  vanish for large fields, thus establishing a consistent connection to classical optics [52].

As it is well known, the superposition of coherent fields leads to a summation of the field amplitudes. Accordingly, the superposition of two coherent states  $|\alpha_1\rangle$  and  $|\alpha_2\rangle$  forms another coherent state with the summed amplitude:  $\hat{a}|\alpha_1 + \alpha_2\rangle = (\alpha_1 + \alpha_2)|\alpha_1 + \alpha_2\rangle$ .

This can be formally expressed by a displacement of  $|\alpha_1\rangle$  by  $\alpha_2$  in phase space:

$$|\alpha_1 + \alpha_2\rangle = \hat{D}(\alpha_2) |\alpha_1\rangle \equiv e^{\alpha_2 \hat{a}^\dagger - \alpha_2^* \hat{a}} |\alpha_1\rangle, \quad (5.2)$$

with the displacement operator  $\hat{D}(\alpha_2)$ . The vacuum state  $|0\rangle$  is equivalent to the coherent state with amplitude 0. Hence, any coherent state can be obtained from a displacement of the vacuum state:

$$|\alpha\rangle = \hat{D}(\alpha) |0\rangle.$$

This displacement in phase space is illustrated in Fig. 5.1(a).

Of course, not only the vacuum state can be superimposed with a coherent field of amplitude  $\alpha$ , but any photon number state  $|k\rangle$ . This is formally described by a displacement of the Fock state in phase space and leads to the notion of displaced number states or displaced Fock states (DFS)  $|\alpha, k\rangle \equiv \hat{D}(\alpha) |k\rangle$ . Their photon number probability amplitudes can be calculated as [97, 98]:

$$\langle n|\alpha, k\rangle = e^{-\frac{|\alpha|^2}{2}} \sqrt{n!k!} \alpha^{n-k} \sum_{j=\max(0, k-n)}^k \frac{(-1)^j |\alpha|^{2j}}{j! (k-j)! (n-k+j)!}, \quad (5.3)$$

which contains the distribution of a coherent state as special case  $k = 0$  (cf. Eq. (5.1)). Some examples of corresponding probability distributions  $P_{\alpha, k}(n) \equiv |\langle n|\alpha, k\rangle|^2$  are presented in Fig. 5.1(b). The blue curve shows the single-peaked Poissonian of the coherent state ( $k = 0$ ). As evident from the other plots, the distribution broadens for growing order  $k$  and exhibits  $k + 1$  maxima.

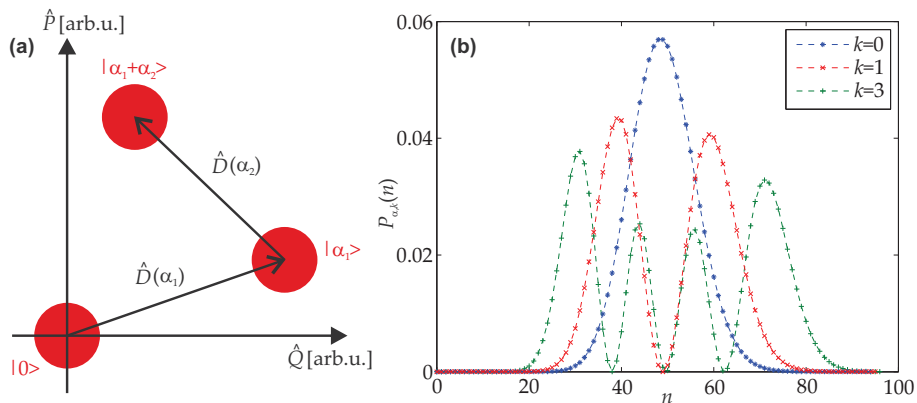


**Figure 5.1:** Displacement of Fock states. (a) Phase space diagram illustrating the mean positions (centres of the spheres) and uncertainties (radii) of coherent states, which arise from a displacement of the vacuum state. (b) Probability distribution of displaced Fock states  $|\alpha, k\rangle$  in the photon number basis for  $\alpha = 7$ .

Besides this fundamental appearance as product of a coherent field and a photon number state, DFS arise in a variety of further quantum optical contexts. Due to their hybrid character containing phase as well as photon number information, they form a versatile tool for the measurement of quasi-probability distributions of quantum states [101, 102]. This has been successfully performed on coherent states [103], on single photons [104] and motional states of trapped ions [105]. Moreover, DFS form the eigenstates of two-level atoms in an externally driven cavity [106] and it has recently been predicted that the use of entangled displaced single photons can enhance communication rates in quantum information processing applications, compared to conventional single photons, due to the additional phase degree of freedom [107]. Last but not least, electronic transitions in molecules obey the same principles [98]: The ground state as well as the excited state have vibrational sublevels, which are in good approximation harmonic oscillator eigenstates, typically with a displacement between the two parabolas in the energy vs. inter-atomic distance diagram. The probabilities for electric dipole transitions between the sublevels are given by the Franck-Condon factors [108, 109], which show the same characteristic oscillatory behaviour as the number distribution of DFS.

Despite this ubiquitousness, the experimental generation of DFS has so far been limited to very low orders of  $k$ . The main reason is the difficulty in generating pure number states to be superposed with a coherent state, be it in a photonic [99] or an ionic setting [100]. The latter approach holds the current record with  $k = 2$  and  $\alpha \approx 2.8$ .

As it will be demonstrated in the following, a viable alternative to gain insight into the genesis of DFS is offered by an emulation of the displacement process in lattices of coupled waveguides. In a lattice with specifically engineered coupling distribution, the probability distribution  $P_{\alpha,k}(n)$  can be mapped onto the light intensity distribution  $I_n$  [95, 96]. In particular, the Fock state ladder is represented by the array of waveguides and the displacement corresponds to longitudinal evolution. This has the great advantage that the parameters  $k$  and  $\alpha$  are only limited by the physical dimensions of the emulator. Moreover, the evolution of the light intensity during the displacement can be directly monitored, as no collapse of the wavefunction occurs for classical light.

The idea of this novel concept is to represent each Fock state by a single waveguide. Therefore, a semi-infinite array of waveguides is required. The modal light amplitudes  $\{b_n\}_{n=0}^{\infty}$  are governed by the coupled mode equations (cf. Eq. (3.1)):

$$i \frac{d}{dz} b_n(z) + C_n b_{n-1}(z) + C_{n+1} b_{n+1}(z) = 0, \quad (5.4)$$

with nearest-neighbour coupling  $C_n$  between guides  $n - 1$  and  $n$ , obeying  $C_0 = 0$ . The initial Fock state  $|k\rangle$  shall be represented by an excitation of the lattice at site  $k$ , i.e.,  $b_n(0) = \delta_{n,k}$ . Then, the propagation along the axis  $z$  shall correspond to a growing displacement magnitude  $|\alpha|$ . Clearly, not the entire complex plane can be mapped onto a single axis. Instead a displacement along the positive  $\hat{P}$ -axis of phase space is chosen. One requires that the light amplitude  $b_n(z)$  corresponds to the probability amplitude of the DFS  $|i\rho z, k\rangle$ , with some constant  $\rho > 0$ :

$$b_n(z) = \langle n | \hat{D}(i\rho z) | k \rangle.$$

With this and the definitions of the operators (2.11),(5.2) one finds immediately for the coupled mode equation (5.4):

$$i \frac{d}{dz} b_n(z) + \rho \left( \sqrt{n} b_{n-1}(z) + \sqrt{n+1} b_{n+1}(z) \right) = 0.$$

Hence, the coupling constants must grow with the square root of the transverse waveguide coordinate  $C_n = \rho\sqrt{n}$  in order for the analogy to hold. Then the directly measurable intensity  $I_n(z)$  corresponds to the number probability  $P_{i\rho z, k}(n) = P_{iC_1 z, k}(n)$ . Another benefit of the optical approach is that by a single experiment, i.e., the excitation of site  $k$ , the displacement is monitored for the entire interval  $[0, \alpha_{\max}]$  with the maximum amplitude determined by the length of the sample  $L$  and the coupling between the first two sites,  $\alpha_{\max} = iC_1 L$ .

In a real experimental setting, the lattice can only contain a finite number of waveguides  $N$ . Hence, the projection of the DFS onto the Fock ladder will be truncated at the state  $|N - 1\rangle$ .  $N$  is chosen such that the high- $n$  tail of  $P_{\alpha_{\max}, k}(n)$  (see Fig. 5.1(b)) does not reach the boundary, and hence the truncation does not significantly compromise the analogue. An illustration of a Glauber-Fock waveguide lattice is given in Fig. 5.2.

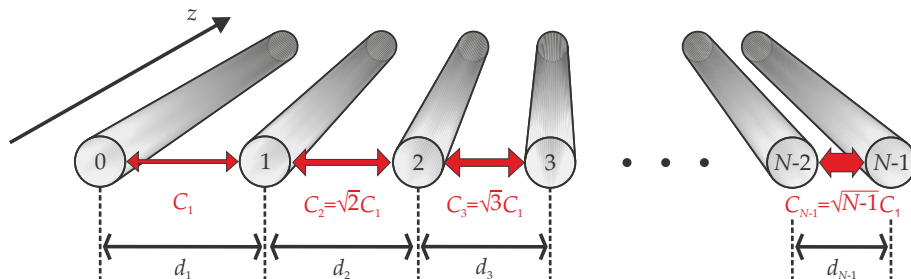


**Figure 5.2:** Schematic illustration of a truncated Glauber Fock waveguide lattice with  $N$  waveguides. The square root growth of the coupling strength  $C_n$  is implemented by a judicious choice of the waveguide separations  $d_n$ .

The coupling strength between two waveguides is determined by the overlap of their mode fields and the index profile, as governed by Eq. (2.13). The most practical way to tune this overlap without affecting the on-site propagation constants in an inhomogeneous manner is a controlled variation of the distance between identical guides. A larger separation between adjacent guides  $d_n$ , leads to a smaller overlap, reducing the coupling  $C_n$ . Hence, the waveguides should be positioned increasingly dense towards the high- $n$  region of the lattice, in order to implement the square root distribution  $C_n \propto \sqrt{n}$  (see Fig. 5.2).

The waveguide separations, which are required for a realisation of the coupling strengths of concern in this work, lie in the range  $10 \mu\text{m} \lesssim d \lesssim 40 \mu\text{m} \gg \lambda$ . For such distances substantially larger than the wavelength, the waveguide modes decay exponentially away from the waveguide centre. Hence, the coupling decays exponentially with waveguide separation in the region of interest [75]:

$$C_n = C_1 e^{-\frac{d_n - d_1}{\eta}}. \quad (5.5)$$

Here,  $C_1$  is taken as a given value whereas  $d_1$  and  $\eta$  are open parameters depending on the particular inscription conditions as well as the wavelength and polarisation of the propagating light. To obtain the desired coupling dependence  $C_n = C_1 \sqrt{n}$ , one finds straightforwardly from (5.5) the required distribution of waveguide separations:

$$d_n = d_1 - \eta \log(\sqrt{n}). \quad (5.6)$$

To find the values of  $\eta$  and  $d_1$ , a series of directional couplers (see chapter 2.2.2) has been fabricated in a  $L = 1.05 \text{ cm}$  long fused silica sample with pulse energy  $E_p = 220 \text{ nJ}$ , writing velocity  $v_0 = 1.5 \text{ mm s}^{-1}$  and separations  $11 \mu\text{m} \leq d \leq 30 \mu\text{m}$ . Each coupler is excited in one of its channels, say number 1, by an H-polarised continuous wave laser beam with  $\lambda = 633 \text{ nm}$ . The output intensities  $I_1$  and  $I_2$  are recorded on a CCD<sup>1</sup> and the coupling strength  $C$  can be obtained from their ratio according to

$$\tan(CL) = \sqrt{\frac{I_2}{I_1}}. \quad (5.7)$$

The latter expression follows directly from the analytic solution of the coupler, the classical analogue of Eq. (2.20).

The coupling strengths  $C$  have been determined employing this method for all 20 couplers and plotted over their waveguide spacing  $d$  (see Fig. 5.3). The graph reveals clearly an

---

<sup>1</sup>The numeric values are taken from the peak intensities of the mode fields after a digital low-pass filtering for artifact removal.



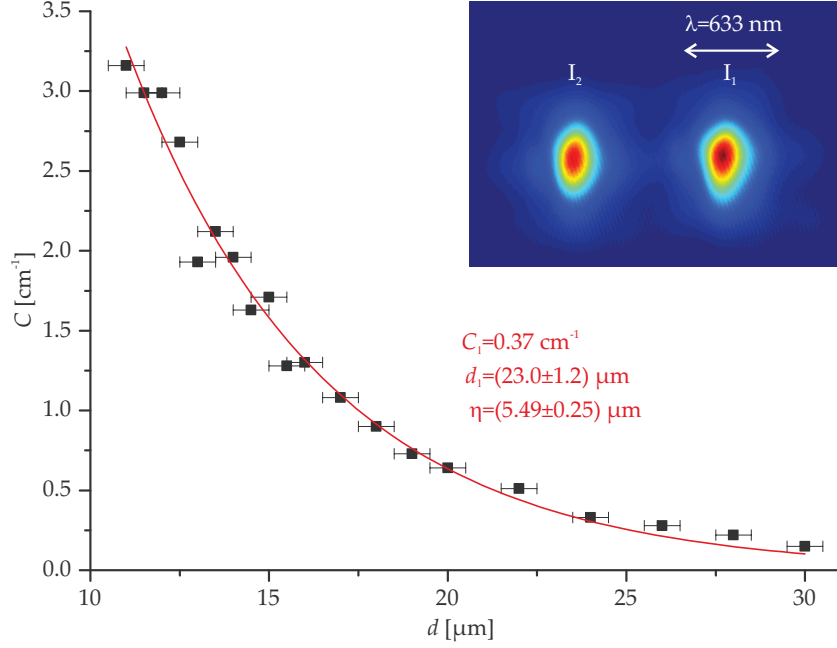


**Figure 5.3:** Measured coupling vs. distance dependence in directional coupler used as a calibration of the parameters  $d_1$  and  $\eta$  of the Glauber Fock lattice for a given  $C_1 = 0.37 \text{ cm}^{-1}$  and  $\lambda = 633 \text{ nm}$ . The error bars indicate the positioning precision of the fabrication setup and the red curve is the best exponential fit to the data points. The inset shows the output intensity of the coupler with  $d = 19 \text{ }\mu\text{m}$ , where the right waveguide has been excited with H-polarisation, as indicated by the white arrow.

exponential dependence, as expected from Eq. (5.5), with the uncertainty in waveguide positioning of  $\pm 0.5 \text{ }\mu\text{m}$  as the major source of errors. The coupling between the first two sites in the Glauber-Fock lattice was chosen to be  $C_1 = 0.37 \text{ cm}^{-1}$ , as it provides a good compromise between the maximum displacement amplitude  $\alpha_{\text{max}}$  and the initial Fock state order  $k$  which can be investigated on the maximum available length (10 cm) without exceeding practically feasible values for the largest coupling in the system ( $C_{N-1} \lesssim 3 \text{ cm}^{-1}$ ). With this choice, the parameters of interest turn out to be  $d_1 \approx 23 \text{ }\mu\text{m}$  and  $\eta \approx 5.5 \text{ }\mu\text{m}$ .

Using these values and the same fabrication conditions, a Glauber-Fock lattice consisting of  $N = 59$  waveguides with a length of  $L = 10 \text{ cm}$  has been inscribed. With  $C_1 = 0.37 \text{ cm}^{-1}$  this amounts to a maximum coupling  $C_{N-1} \approx 2.8 \text{ cm}^{-1}$  and a displacement amplitude  $\alpha_{\text{max}} = 3.7i$  at the output of the lattice. The calculated intensity evolution and output profiles are shown in the upper row of Fig. 5.4 for input sites  $k = 0$ ,  $k = 1$ ,  $k = 4$  and  $k = 7$  which correspond to initial Fock states  $|0\rangle$ ,  $|1\rangle$ ,  $|4\rangle$  and  $|7\rangle$  respectively. In addition to a measurement of the output intensity distribution by imaging the output facet onto a CCD, it is also possible to directly monitor the intensity evolution in 1D arrays via a fluorescence microscopy technique [29]. The key to this method is the

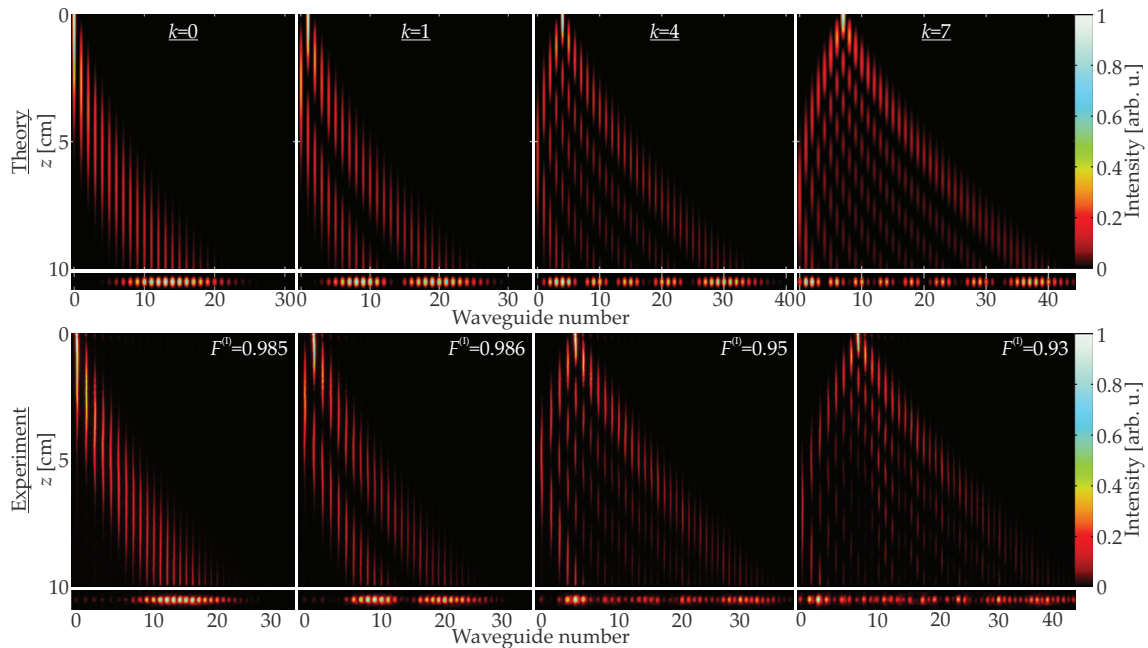


**Figure 5.4:** Light propagation in a Glauber-Fock lattice of 59 waveguides, showing the intensity evolution and the output intensity profile for the input sites  $k = 0$ ,  $k = 1$ ,  $k = 4$  and  $k = 7$ . Top row: Numerical simulation for  $C_1 = 0.37 \text{ cm}^{-1}$ . Bottom row: Experimental data. Only the region of the lattice containing appreciable light intensities is shown. Each image has been normalised to its respective peak intensity. The fidelities  $F^{(1)}$  are calculated from the output distributions of theory and experiment according to Eq. (4.2). Note that for convenience the waveguides are plotted equidistantly in the numerical simulation, whereas they are distributed according to Eq. (5.6) in the experiment.

formation of colour centres from OH-groups in the glass during the waveguide inscription process. As a consequence, a small fraction of guided light at  $\lambda = 633 \text{ nm}$  is absorbed and induces isotropic emission of fluorescence at wavelengths around  $650 \text{ nm}$ . As long as the absorption of the colour centres is not saturated, the emitted fluorescence intensity is proportional to the guided light intensity in the waveguide. The fluorescent light emitted in an upward direction out of the sample is then collected by a microscope objective, spectrally filtered to suppress scattered  $633 \text{ nm}$  radiation, and imaged onto another CCD. The whole imaging optics can be translated along the sample to consecutively measure the entire light propagation.

The intensity evolution measured by this technique is displayed together with the measured output intensities in the lower row of Fig. 5.4 for the same input channels as in the simulation above, exhibiting a very close agreement to the numerical data, with fidelities ranging from 0.93 to above 0.98. It is clearly visible how in the case  $k = 0$  the initial light distribution broadens and evolves into the Poissonian distribution of a coherent state. For  $k > 0$ , the characteristic probability distribution of a DFS with its  $k + 1$  maxima forms after an initial reflection at the  $n = 0$  boundary. In every case, the high- $n$  tails

decay more slowly than the low- $n$  tails, just as one expects from  $P_{\alpha,k}(n)$  (cf. Fig. 5.1**(b)**). The right-hand boundary  $n = N - 1$  is never reached by the propagating light, hence the system can be effectively treated as semi-infinite, as required for an emulation of the semi-infinite Fock ladder.

These results demonstrate how the genesis of DFS from the superposition of a Fock state and a coherent field can be emulated in a compact, robust and controllable optical environment. The classical wave nature of light allows a permanent observation of the displacement process. In this case, the displacement has been investigated simultaneously for all amplitudes in the interval  $\alpha \in [0, 3.7i]$  and for Fock states up to order  $k = 7$  in one and the same structure. In principle, the optical analogue is not limited to the probabilities of the DFS in the Fock basis. Also the phase information is contained in the light field, which could be extracted by interferometric phase retrieval at the end of the lattice. Such measurements have been performed in other waveguide array settings via a superposition of the output field with a reference plane wave and phase stepping [110].

## 5.2 Photon correlations without shift-invariance

As demonstrated in the previous section, the single-particle dynamics in Glauber-Fock lattices offers a great variety of evolution paths. The key is the inhomogeneous distribution of the coupling strength, which breaks the transverse shift-invariance of the array, thus rendering the response of the system dependent on the absolute position. This behaviour is unencountered in lattices with transverse translational symmetry where each waveguide is embedded in the same coupling environment, but also in disordered lattices with shift-invariant probability distributions.

A natural question to pose is how this transverse degree of freedom influences the evolution of two-photon states and their correlation functions. The number of possible paths for each photon will be determined by its input site, namely there will be  $k + 1$  lobes for a photon injected into site  $k$ . Therefore, one can expect a strong dependence of the two-photon correlations on the *absolute* excitation position in the lattice. The further away the input occurs from the  $n = 0$  boundary, the more intricate the correlation patterns should be. This stands in stark contrast to the QRW of photon pairs in uniform lattices [36, 37] (see Fig. 2.3), or otherwise shift-invariant systems [66, 93, 94], where the two-photon correlations only depend on the *relative* separation of the input guides and the type of the input state.

As in any waveguide lattice, the evolution of the bosonic creation operators is governed by

the evolution equation (2.22). The rows of the unitary evolution matrix  $\mathbf{U}$  are the amplitude response functions of the lattice for single-site excitation. By virtue of the analogy between the light evolution in a Glauber-Fock lattice and the displacement of number states, as discussed in the previous section, this response is equivalent to the probability amplitude of a DFS in the Fock basis as given in Eq. (5.3):

$$U_{k,n}(z) = \langle n | iC_1 z, k \rangle. \quad (5.8)$$

With this analytic solution at hand, all correlations of products states can be calculated according to Eq. (2.27), whereas correlations of path-entangled states are governed by Eq. (2.28). For both types, the average photon number distribution is given by (2.26).

The lattice under consideration has  $N = 59$  waveguides,  $L = 10$  cm and  $C_1 = 0.36 \text{ cm}^{-1}$ . The average photon numbers for single guide excitation can be calculated from (2.23) and (5.8) and are shown in Fig. 5.5(a) for the first five sites  $k = 0, \dots, 4$ . Once again, the output distribution of the photons assumes the typical probability distribution of a DFS

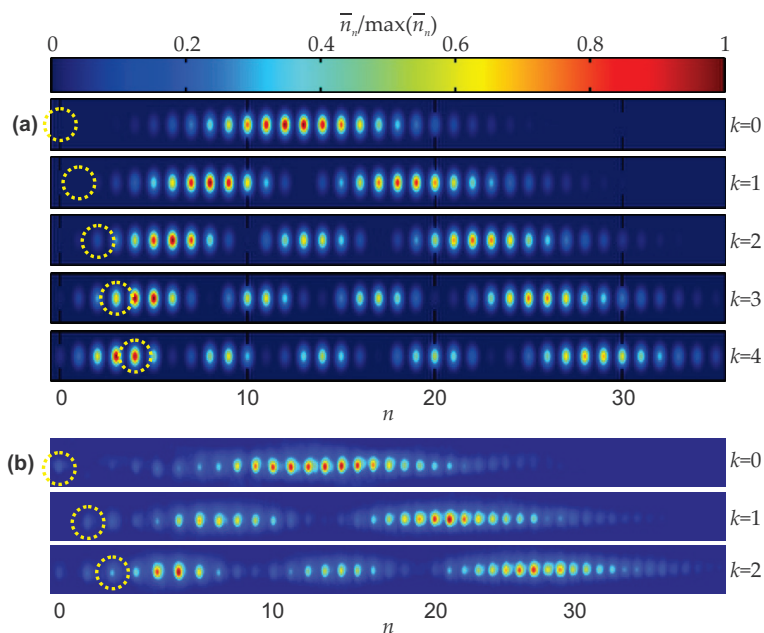


**Figure 5.5:** Single particle output distribution in a Glauber-Fock lattice. (a) Calculated normalised mean photon number distribution for a lattice with  $C_1 = 0.36 \text{ cm}^{-1}$  after an evolution length of  $L = 10$  cm for  $k = 0, \dots, 4$ . (b) Measured output intensity distribution in such a lattice for an excitation of the guides  $k = 0, 1, 2$  with  $\lambda = 800$  nm. The same colormap as in (a) is used and each image has been normalised to its respective peak intensity. In both subfigures, only the region of the lattice containing appreciable photon numbers/light intensities is shown and the input guides are marked by yellow circles. In (a) the waveguides are plotted equidistantly, whereas they are distributed according to Eq. (5.6) in the experiment (b). The experimental data is discussed later in the text (see page 66).

with its  $k + 1$  maxima and its increasing width for larger  $k$ . If two photons enter such a Glauber-Fock lattice, there will be many output channels in which a detection event could originate from both of the input channels  $k$  and  $l$ . For example, the site  $n = 10$  can be reached from the input channels 0, 1 and 3, whereas  $n = 20$  is connected to the input sites 1, 2 and 4. Hence, one can expect diverse quantum path interferences which should manifest themselves in the photon correlation functions.

The simplest case is the product state  $|\Psi_{k,l}^{(p)}\rangle$  being initialised on the leftmost channels  $(k, l) = (0, 1)$ . In this case, the single lobe of  $k = 0$  interferes with the two lobes of  $l = 1$ . The resulting correlation function at the output of the lattice is shown in Fig. 5.6(a). It exhibits two peaks on the main diagonal. They occur exactly where the overlap between the two single photon distributions (see first two rows in Fig. 5.5(a)) is the largest, near  $n = m = 10$  and  $n = m = 16$ . So if a photon is in one of the two overlapping regions, the other occurs there as well. This is the typical photon-bunching effect. However, there are also sections, which can only be occupied by one of the photons, as the single photon distributions do not overlap there ( $n = 13$ ,  $n < 4$  and  $n > 25$ ). This leads to the anti-diagonal trench splitting the correlation function in the centre as well as to a rapid decline away from the two maxima along the main diagonal.

In a shift-invariant lattice, the same pattern of the correlation function would be obtained for any nearest-neighbour input. This is not the case in Glauber-Fock lattices. A mere shift by a single site changes the two-photon probability distribution quite considerably (see Fig. 5.6(b)): The two peaks are shifted to  $n = m = 7$  and  $n = m = 21$ , where the outer lobes of the single-particle distributions overlap (cf. second and third row of Fig. 5.5(a)). Furthermore, additional off-diagonal peaks arise, such as the one around  $(m, n) = (15, 7)$ . This means that the photons may bunch in the first overlap region around  $m = n = 7$  as well as split between the first and third region at  $n \approx 15$ . However, they cannot split between the first and second ( $n \approx 11$ ) or first and last ( $n \approx 21$ ) region, as indicated by the corresponding minima of the correlation function. Hence, the previously simple bunching characteristic is replaced by a more intricate behaviour which exhibits bunching as well as events with separate output locations for some of the overlapping photon paths. The correlation pattern is complemented by additional anti-diagonal ridges and trenches, the latter occurring wherever the single photon distributions do not overlap.

The correlation function of the next higher order  $(k, l) = (2, 3)$  is plotted in Fig. 5.6(c). It clearly continues the trend towards more off-diagonal peaks, anti-diagonal ridges and trenches as well as a spreading of the overall distribution. For very large  $k$  the coupling profile  $C_n \propto \sqrt{n}$  gets increasingly flat and the correlation function approaches the one of

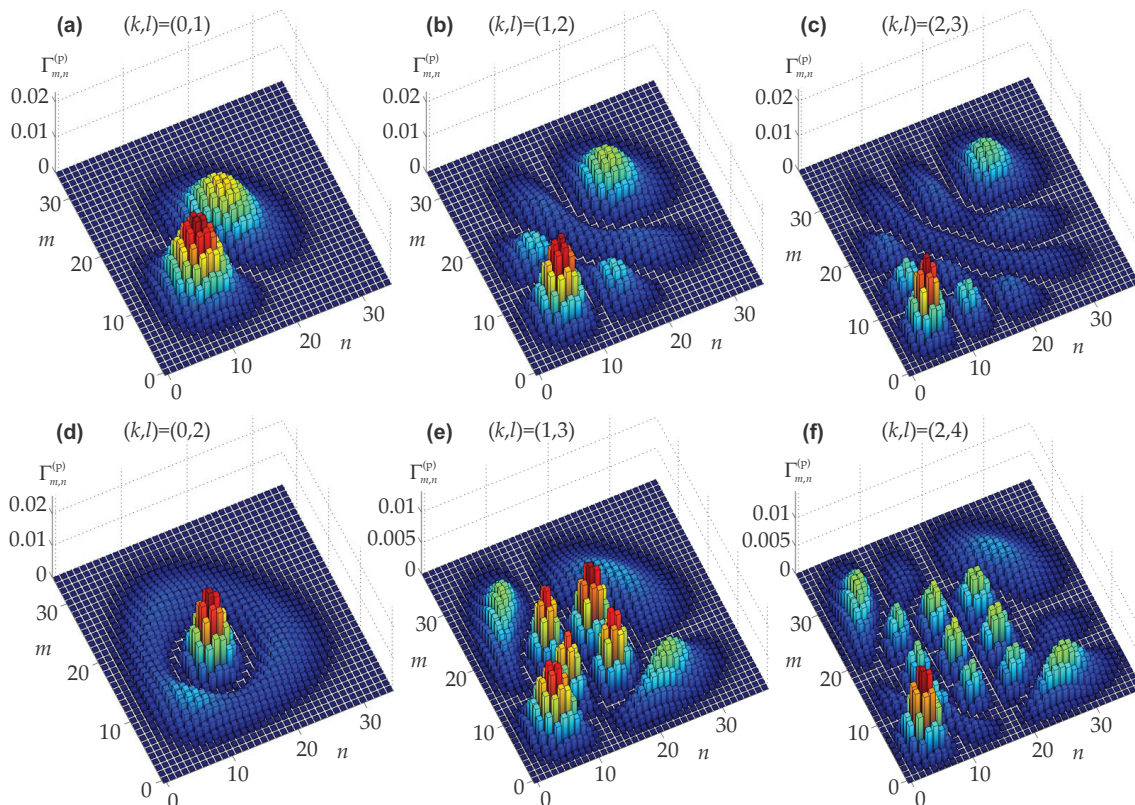


**Figure 5.6:** Calculated two-photon correlation functions of a product state incident on the Glauber-Fock lattice with parameters as in Fig. 5.5. **(a-c)** Nearest-neighbour excitation  $l = k + 1$ . **(d-f)** Next-nearest-neighbour excitation  $l = k + 2$ , both for  $k = 0, 1$  and  $2$ . Again, the high- $m(n)$  region is not shown for better visibility of the relevant elements.

a uniform 1D array (cf. Fig. 2.3(c)).

A similar tendency towards increased complexity is observed for next-nearest neighbour excitation. In the simplest case  $(k, l) = (0, 2)$ , shown in Fig. 5.6(d), one finds a pronounced bunching peak around  $m = n = 13$ . This peak is located in the dominant overlap region of the single photon distributions (cf. first and third row of Fig. 5.5(a)). The surrounding circular trench is associated to destructive quantum interference between the inner and the outer overlapping regions as well as to events where a photon is detected in a region which can only be reached from one of the input channels. For an increasing separation to the boundary of the lattice this outer ring as well as the inner maximum break up into more and more peaks (see Figs. 5.6(e,f)). There are considerable numbers of on- as well as off-diagonal peaks, so bunching events occur as well as separate photon detections. Again, for large  $k$ , the two-photon correlation approaches the distribution of a next-nearest neighbour input in a uniform array (see, e.g., [36]).

These correlation functions demonstrate how the quantum interference of two indistinguishable photons in a Glauber-Fock lattice is governed by the site-dependent number and structure of the interfering photon paths. Hence, the outcome of a QRW in such a

lattice is strongly influenced by the absolute position of the input state, not only by the distance between the input guides.

As a next step, these photon correlations are investigated by means of the classical characterisation technique presented in chapter 3.1 [62, 96]. To this end, a Glauber-Fock lattice designed for the wavelength of the interferometric setup shown in Fig. 3.1 ( $\lambda = 800$  nm) is required. A calibration measurement with directional couplers, as explained in the previous section, has been conducted. From this, the distance parameters for a lattice with  $C_1 = 0.36 \text{ cm}^{-1}$  were found as  $d_1 \approx 34 \mu\text{m}$  and  $\eta \approx 10.7 \mu\text{m}^2$ . Another lattice, consisting of  $N = 59$  waveguides and having a length of 10 cm, was fabricated with these parameters. The output intensities from a single waveguide excitation of the first three sites are shown in Fig. 5.5(b). They follow again the probability distribution of a DFS, the minima being even more clearly visible than in the experiments with  $\lambda = 633$  nm from the previous section<sup>3</sup>. A noteworthy difference to the theoretical distribution (a) lies in a slight shift towards larger  $n$  on the right hand side, causing an increased width of the intensity distribution. This seems to arise from an enlarged transverse ‘acceleration’ of the light towards higher  $n$ , likely resulting from the coupling distribution growing slightly stronger than intended in the high- $n$  region.

The correlation function  $\Gamma_{m,n}^{(p)}$  of the product state input is classically emulated for the nearest-neighbour channels  $(k, l) = (0, 1)$  and  $(k, l) = (1, 2)$ , as well as the next-nearest-neighbour configuration  $(k, l) = (0, 2)$ . The classical correlation  $\Gamma_{m,n}^{(c)}$  is obtained for each case by averaging over 60 random phases in a two-beam interferometric measurement and deducting single-waveguide excitation terms, as given by Eqs. (3.4) and (3.6). The results are shown in Fig. 5.7. The structure of the corresponding two-photon correlations (see Fig. 5.6(a,b,d)) is generally reproduced including all major peaks and valleys, albeit with reduced contrast. The increased width of the single-photon distributions on the right-hand side in the investigated lattice is clearly reflected in the larger spread of the correlation functions towards higher waveguide indices  $n$  and  $m$ . This also accounts for the lower absolute values of the coincidence probabilities. In the case of next-nearest neighbour excitation the ridges at  $m = 4 \dots 5$  are relatively large in comparison to the expected correlation. This can be attributed to the enlarged first and reduced central peak in the single-photon distribution for  $k = 2$  as well as the increased spread of the  $k = 0$  distribution (cf. Fig. 5.5) in the experiment, which reduces the probability for

<sup>2</sup>The mode size, and thereby the coupling strength, grows with increasing wavelength and decays slower over distance. Hence, at 800 nm larger waveguide separations and variations of that separation, the latter being governed by the parameter  $\eta$ , are needed to obtain the same coupling strengths as at 633 nm. Otherwise, the same fabrication parameters as in the previous section have been used.

<sup>3</sup>The larger value of  $\eta$  at  $\lambda = 800$  nm makes the system less vulnerable to positioning errors.

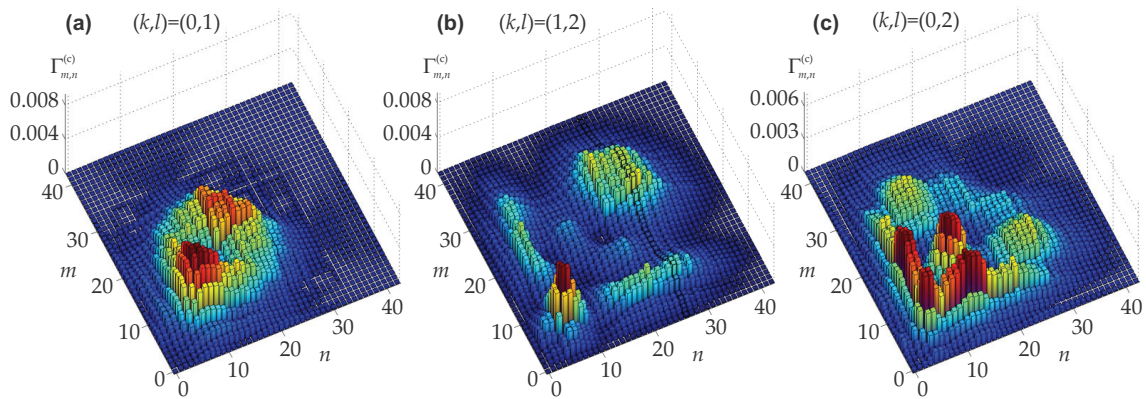


**Figure 5.7:** Measured classical correlations in the Glauber-Fock lattice. The subpanels show the input configuration  $(k, l) = (0, 1)$ (a),  $(1, 2)$ (b) and  $(0, 2)$ (c), respectively.

constructive quantum path interference in the centre.

Once again, this demonstrates the benefits of the classical measurement technique, which allows to evaluate the expected impact of the fabrication induced imperfections on the QRW of photon pairs in the lattice without the additional efforts necessitated by experiments in the single-photon regime. In the current case, the results suggest that the produced Glauber Fock lattice suffices to observe the key features of the predicted correlation patterns. At the same time, an increased spread of the distribution towards the strongly coupling end of the lattice as well as some alterations in the relative probabilities of the coincidence events can be expected due to the deviations of the lattice properties from the ideal Glauber-Fock configuration.

Before path-entangled photons will be investigated, the correlation of a pair of indistinguishable fermions is studied. This will prove to aid the understanding of the entangled photon behaviour. As photons are always bosons, fermions are clearly unphysical entities in optical waveguides. Nonetheless, it has recently been demonstrated how polarisation entangled states of photons can be exploited to simulate the dynamics of fermions on a lattice, be it in a coupler cascade [50] or in a continuous waveguide lattice [111]. Alternatively, it is possible to investigate fermionic dynamics directly in other discrete systems, such as trapped atoms in optical lattices [112]. Hence, a QRW of fermions in a Glauber-Fock lattice may well be of interest for future experiments.

The propagation of fermion pairs in lattices can be formally treated just as outlined for photons in chapter 2. The only two differences are that the fermion ladder operators  $\hat{f}_n^{(\dagger)}$  obey the anti-commutator relation  $\{\hat{f}_m, \hat{f}_n^\dagger\} = \delta_{m,n}$  and that only one fermion can occupy each mode:  $\hat{f}_n^\dagger |0, \dots, 1_{(n)}, \dots, 0\rangle = 0$ , as required by the Pauli-exclusion principle [113].



With this, the fermionic input state on channels  $k$  and  $l$  ( $k \neq l$ ) can be expressed as:

$$\left| \Psi_{k,l}^{(f)} \right\rangle \equiv \hat{f}_k^\dagger \hat{f}_l^\dagger |\emptyset\rangle$$

and its correlation function is [94]

$$\Gamma_{m,n}^{(f)} = |U_{m,k}U_{n,l} - U_{m,l}U_{n,k}|^2.$$

Note that the quantum interference term in this expression has exactly the opposite sign as for indistinguishable bosons (cf. Eq. (2.27)).

A Glauber-Fock lattice with the same parameters as before is considered for the QRW of fermions. Of course, the single-particle distributions  $\bar{n}$  must be identical to the ones of Fig. 5.5(a), as neither bosonic nor fermionic exchange symmetry plays a role in the single-particle regime. The expected two-fermion correlation for the leftmost nearest-neighbour input state  $\left| \Psi_{0,1}^{(f)} \right\rangle$  is plotted in Fig. 5.8(a). As evident from the zero probability on the main diagonal, both particles can indeed not occur together in any channel, as required by the exclusion principle. In essence, the bosonic correlation pattern of Fig. 5.6(a) is rotated by  $90^\circ$ , which means that the fermions tend to antibunch, i.e., they never occupy one of the two overlapping regions of the single-particle distributions together.

Similarly, the shifted input  $(k,l) = (1,2)$  produces a correlation map which resembles the bosonic correlation rotated by  $90^\circ$  (see Figs. 5.8(b) and 5.6(b)). A closer look reveals that the correlation of the bosons is effectively inverted. Wherever, there is constructive quantum interference of photons, there is now a minimum in the fermionic pattern and vice versa. In particular, if one fermion is located in the first overlap region ( $n \approx 7$ ) of the single-particle distributions (cf. second and third row in Fig. 5.5(a)), the other particle may be in the second ( $m \approx 11$ ) or fourth region ( $m \approx 21$ ), but not in the first or third ( $m \approx 15$ ).

The correlation of the next-nearest-neighbour fermionic input  $(k,l) = (0,2)$ , shown in Fig. 5.8(c), cannot be simply regarded as a rotation of the bosonic function. Nevertheless, a very intuitive explanation of the four-peaked pattern is possible: The fermion initialised at site  $k = 0$  leaves the lattice most likely somewhere near the maximum of its single-particle probability distribution centred around  $n = 13$ . Due to Pauli-exclusion, the other fermion is effectively pushed out of the central lobe of its probability distribution, which is also centred at  $n = 13$ . Instead, it tends to occupy one of the outer two lobes which have very little overlap with the distribution of the fermion from  $k = 0$ , leading to the four peaks in  $\Gamma_{m,n}^{(f)}$ .

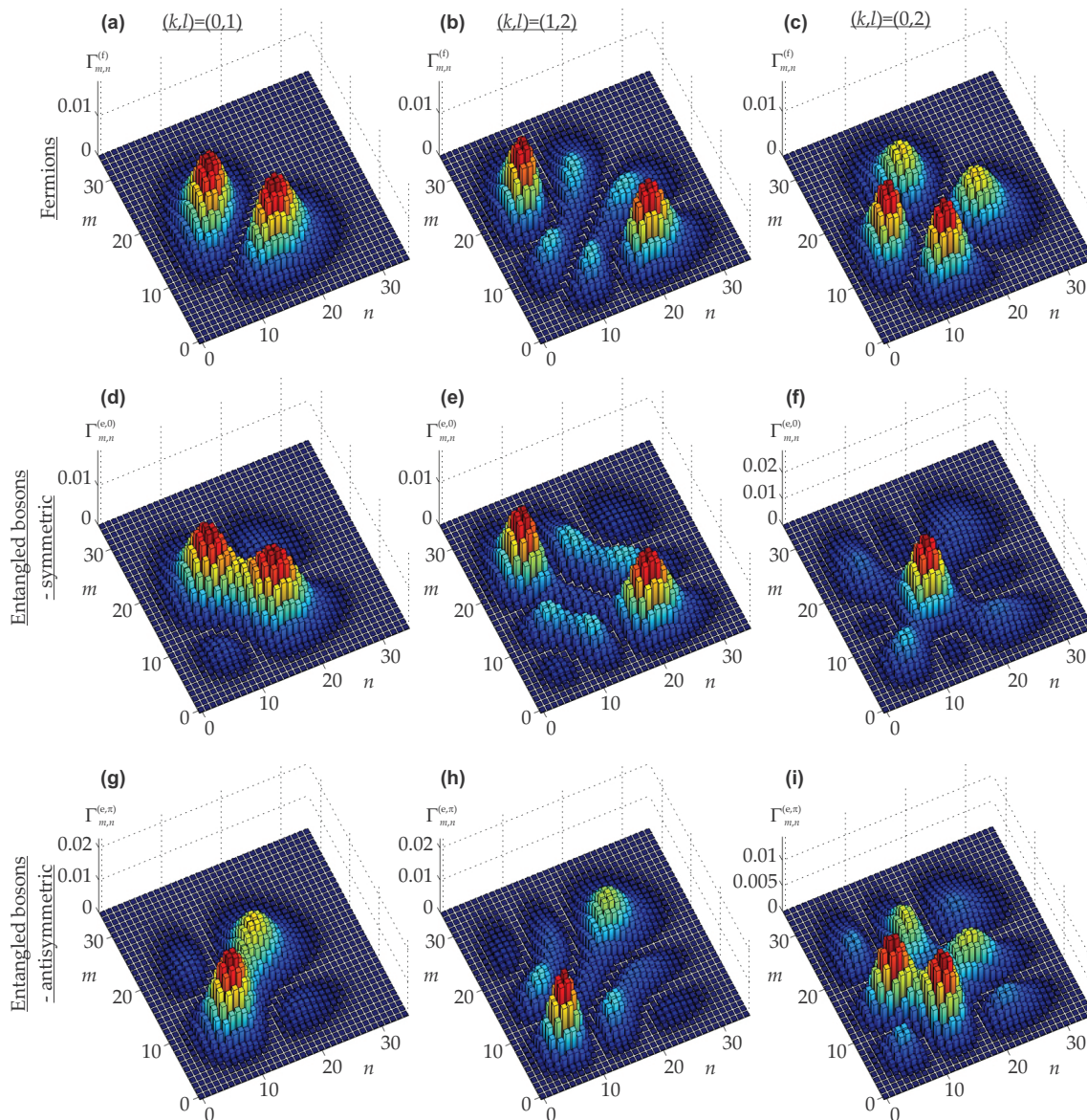


**Figure 5.8:** Calculated two-particle correlation functions in the Glauber-Fock lattice for the first two nearest-neighbour excitations (left and central column) as well as the first next-nearest-neighbour configuration (right column). The top row (**a-c**) shows the correlation of two fermions, whereas the central and bottom row display the correlations of the path-entangled bosonic input states with  $\phi = 0$  (**d-f**) and  $\phi = \pi$  (**g-i**), respectively.

Finally, the evolution of path-entangled two-photon input states is investigated for the exchange phases  $\phi = 0$  (the symmetric state) and  $\phi = \pi$  (antisymmetric). The correlation functions for the three input configurations  $(k, l) = (0, 1)$ ,  $(1, 2)$  and  $(0, 2)$  are displayed in Fig. 5.8(**d-i**). A comparison to the corresponding bosonic (Fig. 5.6(**a,b,d**)) and fermionic (Fig. 5.8(**a-c**)) correlations reveals that the correlations of path-entangled photons contain features of both extremes. Hence, their QRW exhibits bosonic bunching as well as fermionic antibunching properties. Interestingly, whether the bosonic or the fermionic behaviour prevails, depends on the symmetry of the entangled photon state, i.e., on  $\phi$ , as well as on the separation of the input sites. For nearest-neighbour input, the antisymmetric state shows predominantly bosonic characteristics (Fig. 5.8(**g,h**)), whereas the same holds true for next-nearest neighbour input in case of  $\phi = 0$  (**f**). The other configurations follow primarily fermionic statistics (**d,e,i**). However, in neither case does the entangled state produce purely bosonic or fermionic correlations. In the boson-dominated scenarios, additional off-diagonal peaks are always visible, whereas in the predominantly fermionic cases no on-diagonal zero-trench occurs.

For all the photon and fermion input states investigated in this section, the absolute initial position within the Glauber-Fock lattice has a strong influence on the correlation patterns, by virtue of the broken shift-invariance. In general, the QRW of the indistinguishable particles gets increasingly complex, for a growing distance to the  $n = 0$ -boundary of the lattice. Moreover, no two input states lead to identical correlation patterns. Therefore, each two-particle probability distribution in a Glauber-Fock lattice effectively acts as a fingerprint of the input state. Conversely, the available state space of a two-particle QRW in the Glauber-Fock lattice is much larger than in a uniform 1D lattice, due to the utilisation of the degree of freedom associated to the absolute transverse position.

# 6 Entangled photons in disordered lattices

In this final main chapter, the evolution of a photon pair in a disordered 1D waveguide lattice will be investigated. Disorder arises in physics whenever a system is subjected to random fluctuations. In quantum mechanics, one has to distinguish between *temporal* and *spatial* disorder. The former means that the potential changes randomly in time which leads to decoherence of the wavefunction. The latter describes the case of a spatially random potential which is constant in time. This case is highly relevant for an understanding of the conductivity of solids: In a perfectly crystalline material, the atomic potential is periodic causing the electronic eigenfunctions of the system to extend over the entire lattice. Hence, the electrons are very mobile and the material has a high conductivity. However, for spatially disordered potentials, as occurring in amorphous materials, some of the eigenstates localise and charge transport is suppressed. This Anderson localisation is at the origin of the low conductivity of electrical insulators. Since its first prediction in 1958 [114], no successful attempts have been made to observe it in a solid. The reason is that it is inherently difficult to isolate single electrons and observe their evolution on the relevant time scales. Moreover, oscillations of the lattice and inelastic electronic scattering cause the atomic potential to fluctuate in time, which rapidly destroys coherence. However, Anderson localisation as such is a pure wave phenomenon, so one may use other platforms than electronic wavefunctions in solids to observe it.

It turns out that linear optics does indeed provide the tools which are necessary for this observation: First of all, photons do not interact with each other, such that a classical beam of light exhibits single photon dynamics. Moreover, their coherence time can be chosen very long by using modern lasers and the photons usually interact only very weakly with the environment. Exploiting these properties, it has been possible to observe enhanced backscattering, a phenomenon which is associated to Anderson localisation, of light in semiconductor powder [115].

In order to observe the suppression of transport in one or two spatial dimensions directly, one can resort to waveguide lattices [116]. The time-independent Schrödinger equation is equivalent to the paraxial Helmholtz equation, which describes light evolution in up to two

---

transverse and one longitudinal dimensions, the latter corresponding to time in quantum mechanics. The wavefunction in the Schrödinger equation maps to the electric field and the potential to the refractive index profile [117]. Regular as well as disordered refractive index profiles, which are invariant along their longitudinal axis can be fabricated by a variety of techniques. Importantly, the replacement of time by a spatial coordinate enables the direct observation of the transport by measuring the light evolution. Furthermore, an effective scaling of the time-axis by appropriately tuning the refractive index profile and the wavelength is possible. This idea culminated in the observation of signatures of disorder-suppressed transport in optical fiber arrays [118] and finally in the Anderson localisation of light in 2D [119] and 1D [30] waveguide lattices. A recent review compiles the research on single-particle Anderson localisation and its observation in waveguide systems [120].

Beyond the single-particle regime, the exchange symmetry of indistinguishable bosons or fermions leads to quantum path interference. This leads to a number of questions: Will both particles localise independently, localise faster than a single particle or, on the contrary, exclude each other from localisation? If the particles localise, will their quantum correlation survive the localisation? Which role plays the type of the input state? Lahini *et al.* started the theoretical investigation on two-particle correlations in a 1D disordered lattice addressing several of these fundamental questions [94]. Another recent prediction was that spatially extended entangled states, i.e., path-entangled photon pairs distributed over many input sites, remain spatially extended upon propagation in a disordered waveguide lattice, even when the single-particle wavefunctions are localised. However, their relative separation localises faster than classical light in the same system [121].

The second part of this chapter presents the experimental observation of this so-called Anderson co-localisation which also represents the first observation of a two-particle continuous-time QRW in a disordered lattice<sup>1</sup>. The experiment is conducted in a planar waveguide array with off-diagonal disorder, i.e., a disorder in the coupling strength. The first part will outline the design and fabrication of the waveguide lattice in which this disorder is implemented as well as the classical characterisation of the device. The experiments in both parts have been performed in cooperation with the CREOL, University of Central Florida.

---

<sup>1</sup>A discrete-time correlated QRW on a single realisation of a disordered lattice of directional couplers has very recently been published [51].

## 6.1 Waveguide lattices with uniform coupling disorder

The starting point for an investigation of Anderson localisation is the coupled mode equation for classical light amplitudes evolving in an infinite 1D nearest-neighbour coupled optical waveguide array:

$$i \frac{d}{dz} b_n(z) + \beta_n b_n(z) + C_n b_{n-1}(z) + C_{n+1} b_{n+1}(z) = 0.$$

The difference to the previous chapter (see Eq. (5.4)) is that here the lattice is regarded as infinite<sup>2</sup> and relative detunings  $\beta_n$  of the waveguides are allowed for the moment.

The original electronic tight-binding model of Anderson assumed even couplings  $C_n = C$  and random values for the on-site energies, which directly translate to the propagation constants  $\beta_n$ , in the optical context. This type of disorder is referred to as *on-diagonal* disorder, as it affects the main-diagonal of the Hamiltonian. This is also the type of disorder which has been implemented in many optical experiments [30, 51, 119].

The other type of disorder is realised in a system of identical waveguides  $\beta_n = 0$  with randomised coupling strengths. In contrast to on-diagonal disorder, this *off-diagonal* disorder preserves a conjugation symmetry of the eigenmodes of the system [122], which is relevant for certain imaging applications [123]. Besides this, essentially the same dynamics of classical light intensity evolution occur for both-types of disorder. Consequently, the suppression of transport and Anderson localisation are also observed in lattices with off-diagonal disorder [118, 124, 125]. In laser-written waveguide lattices, it is easier to implement a controlled disorder in the coupling than in the propagation constants, as waveguide separations can be controlled more accurately than their refractive indices<sup>3</sup>. Therefore, a purely off-diagonal disorder will be considered in the remainder of this chapter.

The aim is to implement a uniform distribution of coupling constants on the interval  $C_n \in [C_0 - \Delta, C_0 + \Delta]$ , with mean coupling  $C_0$ . As discussed in the previous chapter, the coupling follows an exponential dependence on the waveguide separation (5.5):

$$C_n = C_0 e^{-\frac{d_n - d_0}{\eta}}.$$

In this notation  $d_0$  is the waveguide distance corresponding to the average coupling  $C_0$ . With this relation the uniform probability distribution of the couplings  $C_n$  transforms

<sup>2</sup>In practice, this means that the lattice must be large enough, such that boundary effects are irrelevant.

<sup>3</sup>While the repeatability of the waveguide propagation constants is high, their value is more difficult to measure than the interwaveguide coupling

into an exponential distribution of the distances with probability density  $p(d_n)$ :

$$p(d_n) \propto e^{-\frac{d_n-d_0}{\eta}} \mathbb{1}_{[d_{\min}, d_{\max}]}(d_n), \quad (6.1)$$

with the boundaries of the interval  $d_{\min(\max)} \equiv d_0 - \eta \log\left(1 \pm \frac{\Delta}{C_0}\right)$  corresponding to the maximum (minimum) coupling  $C_0 \pm \Delta$ . All waveguide spacings in the array will be independent random variables adhering to this probability distribution.

The random arrays were designed for a mean coupling  $C_0 = 1.7 \text{ cm}^{-1}$ . As for the Glauber-Fock lattices in the last chapter, a series of directional couplers has been fabricated to calibrate the parameters  $\eta$  and  $d_0$ . Here, 19 couplers have been inscribed into a  $L = 2 \text{ cm}$  long glass sample with distances ranging from  $12 \mu\text{m}$  to  $30 \mu\text{m}$  and fabrication parameters  $E_p = 300 \text{ nJ}$  and  $v_0 = 1 \text{ mm s}^{-1}$ . One waveguide of each coupler has been excited with  $\lambda = 800 \text{ nm}$  and H-polarisation and the coupling strengths have been subsequently measured from the output intensity ratios according to (5.7). The result is presented in Fig. 6.1(a), once again showing a clear exponential dependence. From the numerical fitting procedure, the separation corresponding to the mean coupling turns out to be  $d_0 \approx 17.1 \mu\text{m}$  and the scaling parameter is  $\eta \approx 8.0 \mu\text{m}$ . The blue lines indicate

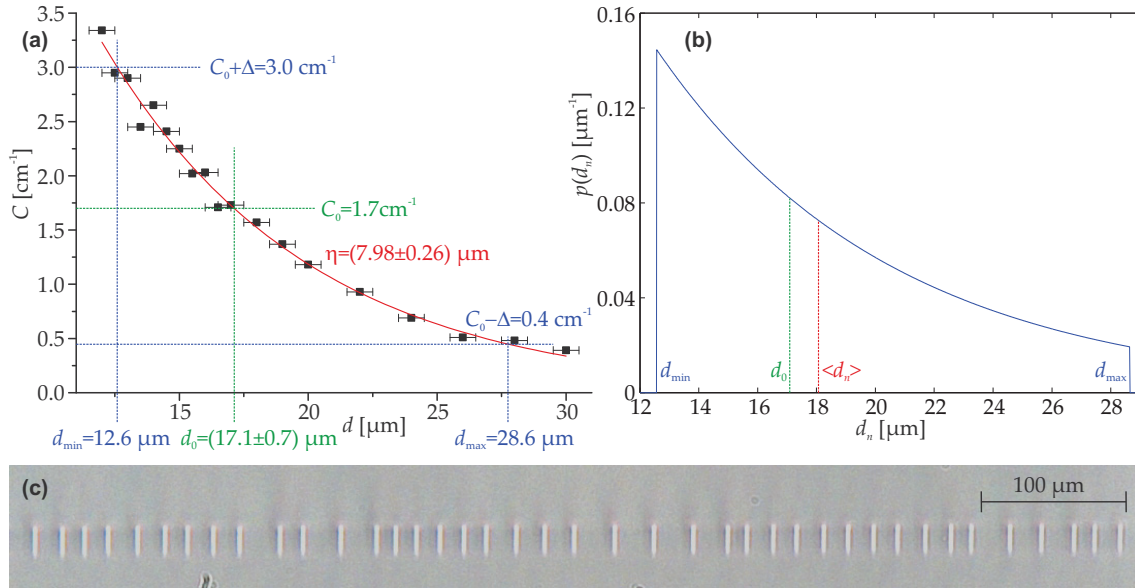


**Figure 6.1:** Implementation of a waveguide lattice with off-diagonal disorder. (a) Measured coupling vs. distance dependence in directional couplers for  $\lambda = 800 \text{ nm}$ . The parameters  $d_0$  and  $\eta$  are obtained from a best exponential fit (red line) to the data for a given value of  $C_0 = 1.7 \text{ cm}^{-1}$ . The error bars indicate the positioning precision of the setup. The blue lines are the boundaries of the coupling and distance intervals for  $\Delta = 1.3 \text{ cm}^{-1} \approx 0.76 C_0$ . (b) Corresponding probability density of the waveguide spacing  $d_n$  which is needed to obtain a uniform distribution of the coupling for the coupling-distance parameters from (a). The distance belonging to the average coupling  $d_0$  is shown in green, the average distance  $\langle d_n \rangle$  in red. (c) Microscope image of the cross-section of a disordered waveguide lattice fabricated according to this probability distribution.

the extreme couplings  $C_0 \pm \Delta$  and the associated separations for the exemplary value  $\Delta = 1.3 \text{ cm}^{-1} \approx 0.76C_0$ .

From these parameters, the exponential probability distribution of the waveguide separations in the array (6.1) can be calculated, as shown in Fig. 6.1(b). Clearly, small distances are more likely than large ones and the interval  $[d_{\min}, d_{\max}]$  is not centered on  $d_0$ , but shifted to larger values. This is necessary as a larger increase of  $d_n$  is required to reach the lower bound of the coupling  $C_0 - \Delta$  than a decrease to reach the upper bound  $C_0 + \Delta$ . Also, due to the nonlinear relationship between distance and coupling, the average separation  $\langle d_n \rangle$  does not coincide with the distance of the average coupling  $d_0$ . A segment of an off-diagonally disordered waveguide lattice, implemented from this probability distribution is displayed in Fig. 6.1(c).

In order to gain insight into the expected light evolution in disordered lattices, a numerical investigation is performed. Four arrays are considered, each consisting of  $N = 101$  waveguides with a length of  $L = 4.9 \text{ cm}$ . The waveguide separations are randomly chosen according to (6.1), with dimensions of the coupling interval  $\Delta = 0$  (a uniform array) and  $\Delta/C_0 \approx 0.41, 0.59$  and  $0.71$  (termed ‘weak’, ‘medium’ and ‘strong’ disorder, respectively). For the uniform array (see Fig. 6.2(a)) one observes the characteristic ballistic propagation with two pronounced outer lobes and the width of the multi-peaked intensity distribution

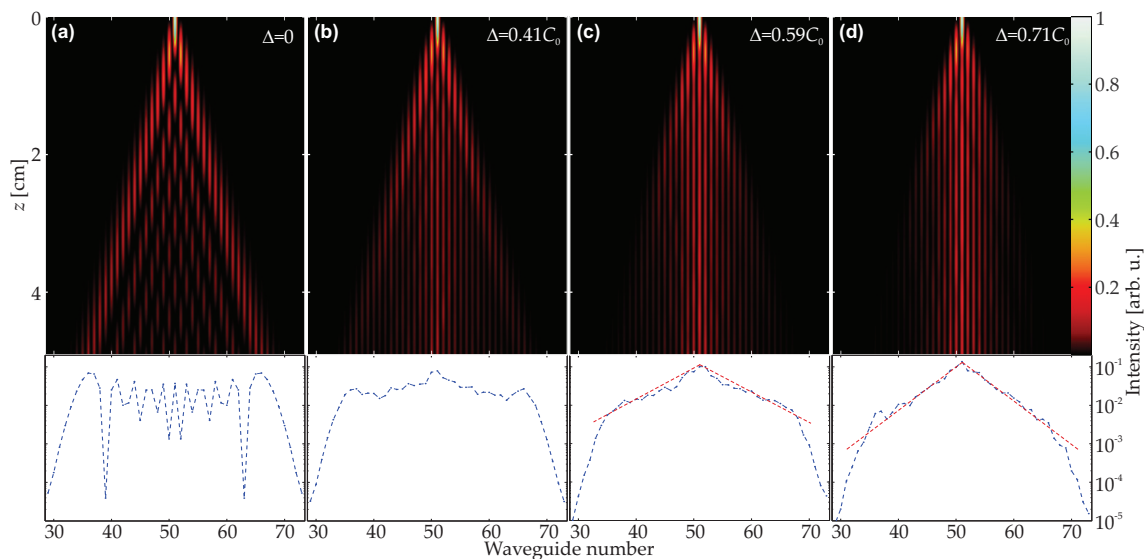


**Figure 6.2:** Calculated light evolution (top row) and output intensity distribution (bottom row) in off-diagonally disordered lattices with 101 waveguides of length 4.9 cm and  $C_0 = 1.7 \text{ cm}^{-1}$ . Only the inner waveguides surrounding the excited central site are shown in each case. (a) Regular lattice. (b-d) Disordered lattices with increasing strength of disorder. The images present ensemble averages with 100 realisations. The exponentials in (c,d) (red dashed lines) serve as a guide to the eye.



growing linearly in  $z$ . Note that the boundaries of the lattice are far away from the main lobes, so their influence on the light evolution can be neglected.

In the presence of disorder the light evolution changes considerably. In a typical realisation, the light takes a random trajectory through the disordered lattice. Of course, a single realisation is not necessarily representative of the phenomena which can be expected for a given level of disorder, nor does it allow to draw conclusions about macroscopic physical quantities, be it conductivities in a solid or transmission spectra of optical materials. To this end, some averaging is required. Here, an ensemble average over the intensities obtained from 100 independent realisations of the lattice spacings  $\{d_n\}_{n=1}^N$  is performed. The result for weak disorder is shown in Fig. 6.2**(b)**. The ballistic outer lobes are still visible in the intensity evolution pattern. However, compared to the regular lattice, the multi-peaked structure of the intensity distribution is washed out. Hence, there is some appreciable probability to find light in any of the waveguides between the two outer lobes. Moreover, a central peak arises, corresponding to light remaining near the initial site of excitation. For increasing disorder, the inner peak gets more and more pronounced, whereas the ballistic lobes disappear **(c,d)**. Another evident feature associated to Anderson localisation are the exponential slopes of the intensity distribution (see red lines). Interestingly, the intensity distribution always approaches the exponentially localised distribution in the limit  $z \rightarrow \infty$  in 1D lattices, as soon as some disorder is present [30, 94]. For stronger disorder, this limit is reached more quickly and the slope of the exponential is steeper. Hence, arrest of transport always occurs in disordered 1D lattices, merely the strength of the confinement depends on the magnitude of disorder.

Instead of ensemble averaging one can also perform spatial averaging by exciting a single lattice at many different input positions. As long as the region over which the averaging occurs is sufficiently large and the disorder does not change across that region, i.e., the disorder is shift-invariant, the two averaging approaches are equivalent [126]. This fact is commonly exploited in optical experiments on Anderson localisation [30, 115, 125] and will also be used in the following to reduce the experimental effort. Instead of fabricating many lattices with the same disorder parameters, it is sufficient to fabricate a single lattice which is large enough to accommodate many input positions. Each distance  $d_n$  is independently chosen from the same probability distribution  $p(d_n)$ . Therefore, the lattice is effectively shift-invariant, as long as the boundaries do not play a role. The lattice size  $N = 101$  allows for a sufficient number of input sites which can be excited without their ballistic lobes (or what remains of them in the disordered lattices) hitting the boundaries (cf. Fig. 6.2).

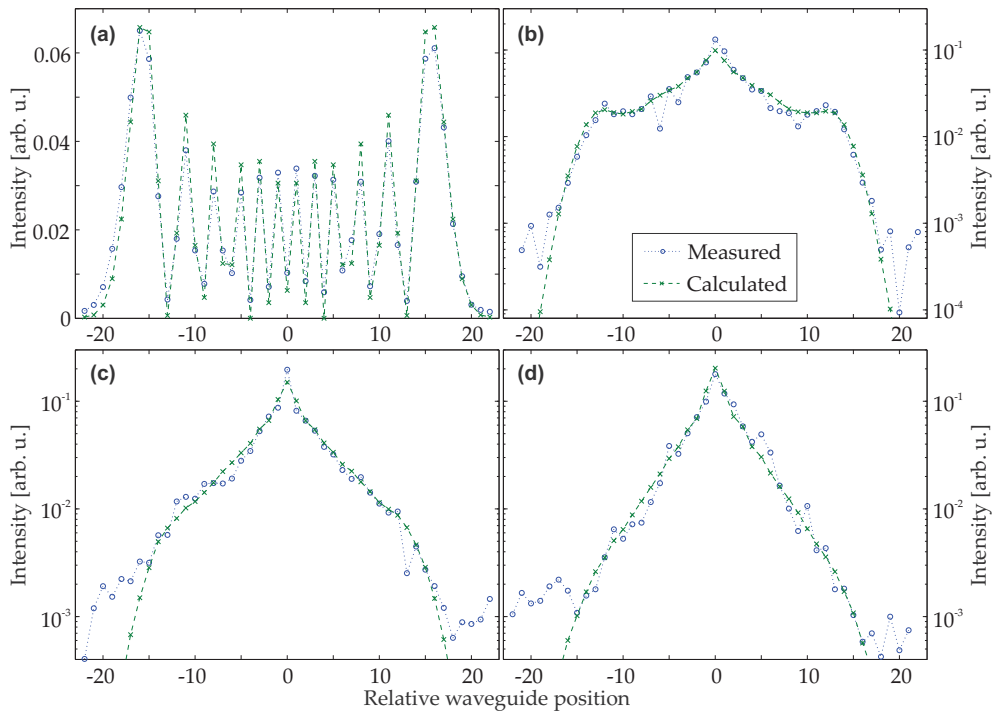


**Figure 6.3:** Observation of Anderson localisation. **(a)** Spatially averaged output intensity of the uniform lattice (blue curve) in comparison to the numerical result for  $C_0 = 1.8 \text{ cm}^{-1}$  (green). The abscissa is the waveguide coordinate relative to the excitation site  $n - k$ . **(b-d)** Same for the disordered lattices. The theoretical curve is an ensemble average over 10,000 realisations with  $C_0 = 1.5 \text{ cm}^{-1}$  and  $\Delta/C_0 = 0.51$  in the case of weak disorder **(b)**,  $\Delta/C_0 = 0.70$  for medium disorder **(c)** and  $\Delta/C_0 = 0.87$  for strong disorder **(d)**.

Consequently, four waveguide lattices have been fabricated with designed coupling and disorder parameters as in the numerical simulation. However, in an array of laser-written waveguides the coupling is often slightly stronger than in directional couplers of the same waveguide separation, due to a mutual influence of the waveguides via their stress fields, which is difficult to predict exactly. In combination with an apparent drift in the inscription laser parameters as well as a different wavelength  $\lambda = 780 \text{ nm}$ , which had to be used in the following experiments for technical reasons, this led to slightly different coupling strengths and somewhat stronger disorders being realised in the lattice, which will be determined momentarily.

The inner waveguides  $k = 31 \dots 71$  of the uniform lattice have been excited and the average of the measured output intensity distributions centered around the input site was taken<sup>4</sup>. The averaged distribution is shown as the blue curve in Fig. 6.3**(a)**. It extends over  $\approx 40$  sites, so the boundaries of the lattice are clearly irrelevant for the light evolu-

<sup>4</sup>The average is taken to compensate for miniscule variations in the output intensity between the input sites due to positioning errors.

tion at all the investigated input sites. The comparison to a numerical simulation (green curve) reveals a very close agreement between the measured distribution and the expected pattern for  $C_0 = 1.8 \text{ cm}^{-1}$ , so the coupling in the uniform lattice is slightly larger than designed.

Subsequently, the three disordered lattices were excited at these positions, measuring the output intensities and performing the spatial average over all 41 input sites. The resulting averaged intensity distributions are displayed as blue data points in Figs. 6.3**(b-d)**. In the weakly disordered case, residual ballistic lobes are visible as well as the central localisation peak (see **(b)**). For the more strongly disordered cases **(c,d)**, the ballistic lobes disappear and a pronounced exponential peak forms in the centre, as expected from the theoretical considerations. Hence, the Anderson localisation of light is clearly observed via spatial averaging in these lattices with coupling disorder. However, the comparison to numerical simulations (shown again in green) reveals that the parameters  $C_0$  and  $\Delta$  deviate from the intended values. The mean coupling can be estimated from the ballistic lobes in the weakly disordered lattice to be  $C_0 = 1.5 \text{ cm}^{-1}$ . The difference to the coupling in the regular lattice may arise from the fact that the fit parameters  $\eta$  and  $d_0$  from the calibration measurement do not exactly reflect the coupling-distance dependence in the disordered lattices. Therefore, the implemented distances impose a different coupling distribution, which may well lead to a shifted mean coupling. Similarly, one finds slightly altered values for the relative magnitudes of the disorder by numerically fitting the exponential slopes of the localisation peak to the measured distribution. It turns out that in these laser-written lattices the values are  $\Delta/C_0 \approx 0.51, 0.70$  and  $0.87$  for weak, medium and strong disorder, respectively.

One should note that despite this deviation from the design configuration, these parameters are nonetheless quite suitable to investigate the effect of an increasing disorder on the light evolution, as they clearly show the different regimes of partial and full Anderson localisation and the associated suppression of transport. Hence, these waveguide lattices should be a practical platform for QRWs of indistinguishable photons in these regimes, which will be investigated in the next section.

## 6.2 Anderson localisation of entangled photons

An important aspect of quantum mechanics is its inherent randomness. In the following this randomness will be exploited to perform the spatial averaging, which is required to

draw reliable conclusions about the system. In principle, a single extended quantum state can replace many different classical input configurations.

The starting point is the symmetric ( $\phi = 0$ ) path-entangled state defined in Eq. (2.25), which resides on two lattice sites at the same time. It can be extended to a state which is entangled across the  $M$  input channels  $k_1, \dots, k_M$ :

$$\left| \Psi_{k_1, \dots, k_M}^{(\text{ext})} \right\rangle \equiv \frac{1}{\sqrt{2^M}} \sum_{j=1}^M \left( \hat{b}_{k_j}^\dagger \right)^2 |\emptyset\rangle = \frac{1}{\sqrt{M}} \sum_{j=1}^M |0, \dots, 2_{(k_j)}, \dots, 0\rangle. \quad (6.2)$$

If a photon pair is initialised in such a spatially extended state, the two photons will always enter the waveguides together. However, it is entirely uncertain in which of the  $M$  waveguides the photons are initialised. Therefore, this state should perform the spatial averaging in the shift-invariant disordered lattices discussed in the previous section by virtue of its intrinsic indeterminism [121].

A straightforward calculation leads to the average photon number distribution after the evolution of the extended state in any waveguide lattice over the distance  $z$ :

$$\bar{n}_m^{(\text{ext})}(z) = \frac{2}{M} \sum_{j=1}^M |U_{m, k_j}(z)|^2.$$

For  $M = 2$ , this yields exactly the known two-site distribution (2.26). Regardless of  $M$ , the average photon number arises always as incoherent sum over the contributions from all single input channels. For the two-photon correlation function, one obtains:

$$\Gamma_{m,n}^{(\text{ext})}(z) = \frac{2}{M} \left| \sum_{j=1}^M U_{m, k_j}(z) U_{n, k_j}(z) \right|^2$$

which is also consistent to the two-channel result (2.28).

The evolution and output distribution of the average photon number in a uniform lattice (parameters as in chapter 6.1.) are shown in Fig. 6.4(a) for an extended entangled input state with  $M = 20$  residing on adjacent channels located in the centre of the lattice. As each input channel is associated to a ballistic propagation pattern (cf. Fig. 2.3), their incoherent sum yields a smooth distribution, with a width determined by the ballistic lobes of the outermost input channels  $k_1$  and  $k_M$ . So the photons can, in principle, leave the lattice at any waveguide of an extended region with a size given by  $M$  and the effective evolution length  $C_0 L$ . The system can again be treated as effectively infinite in the transverse direction, as the boundary is not reached by the photons.

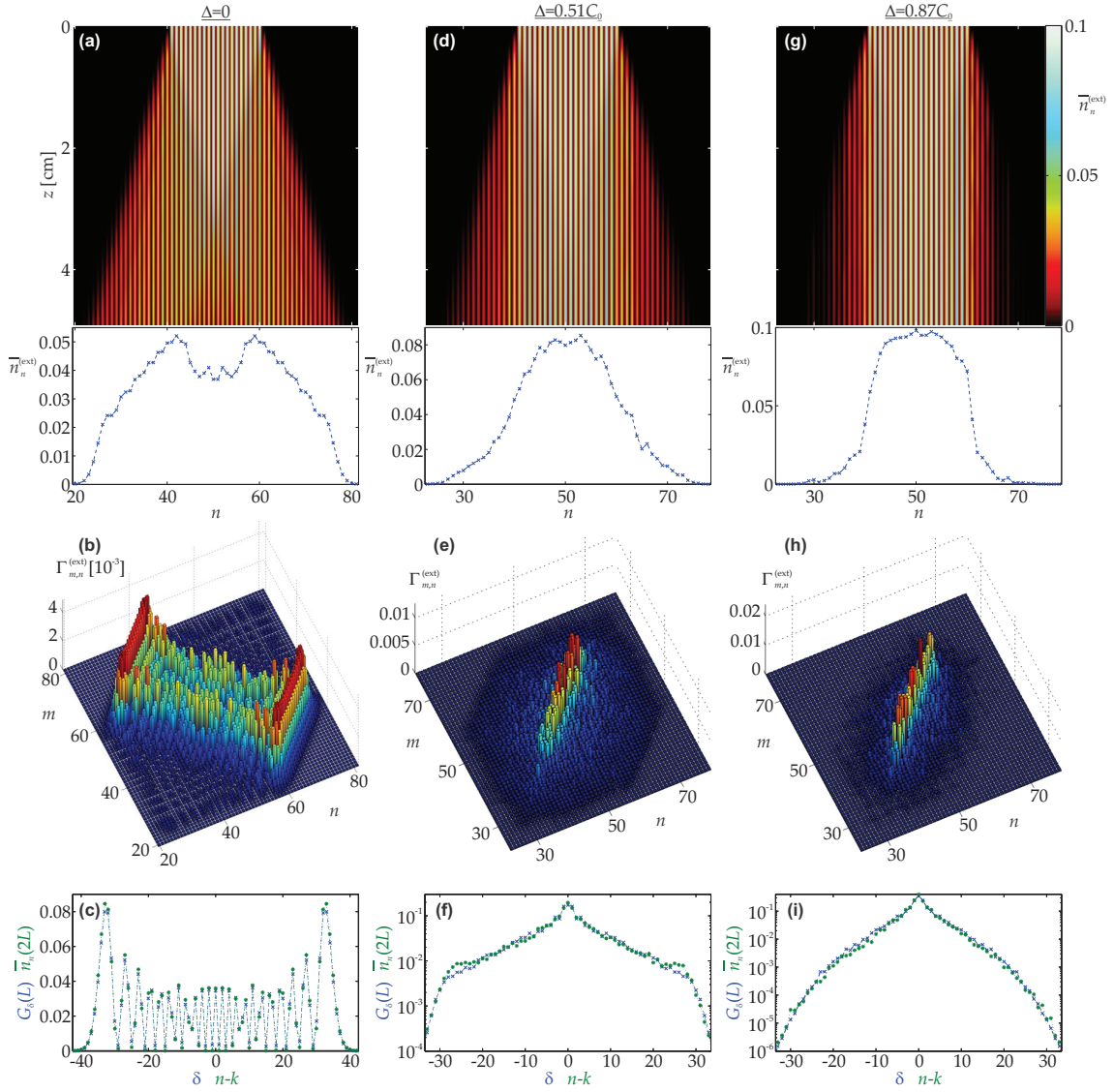


**Figure 6.4:** Numerical Investigation of Anderson co-localisation for  $M = 20$ . Shown are a uniform (a-c), a weakly disordered (d-f) and a strongly disordered lattice (g-i) of length  $L = 4.9$  cm. Top row: Evolution and output distribution of the average photon number. Middle row: Photon correlation at the output. Bottom row: Inter-photon distance function  $G_\delta(L)$  at the output (blue, dashed line) in comparison with the number distribution  $\bar{n}_n(2L)$  from single-waveguide input to site  $k$  after the twofold evolution length (green, dotted line), shifted by  $k$  sites. The results in the disordered lattices are ensemble averages with 20 realisations (500 for  $\bar{n}_n(2L)$ ) in each case. The mean couplings are  $C_0 = 1.8 \text{ cm}^{-1}$  in the uniform lattice and  $C_0 = 1.5 \text{ cm}^{-1}$  in the disordered lattices, as obtained from the analysis of the classical results (see Fig. 6.3).

The correlation function displayed in Fig. 6.4**(b)** exhibits a clear trace of antibunching. The absence of substantial on-diagonal peaks reveals that the photons are very unlikely to occupy a waveguide together, even though this was their initial configuration. Note that the same type of behaviour is observed in the case  $M = 2$  (two antibunching peaks in Fig. 2.3**(d)**). In addition, the long ridges parallel to the main diagonal suggest that certain distances between the photons are more likely than others. This can be quantitatively analysed by introducing the following measure for the inter-photon distance probability [94]:

$$G_\delta(z) \equiv \sum_{m=\max(1-\delta,1)}^{\min(N-\delta,N)} \Gamma_{m,m+\delta}^{(\text{ext})}(z),$$

with the distance  $\delta$  satisfying  $-N + 1 \leq \delta \leq N - 1$ . In case of the uniform lattice, this quasi-distribution<sup>5</sup> exhibits the characteristic structure of the single-site response of the uniform lattice with its ballistic lobes. In particular,  $G_\delta(L)$  for the extended input state matches closely the distribution of the average photon number  $\bar{n}_n(2L)$  for an excitation of the single site  $k$  with two photons, at the twofold evolution length, when shifted by  $k$  sites (see Fig. 6.4**(c)**). A formal equivalence of the two quantities can be shown to hold in the limit  $M \rightarrow \infty$  [121]. Hence, while the photon pair is distributed over a large transverse domain, the individual photon positions are highly correlated, their relative distance underlying a quasi-distribution which is proportional to the shifted probability distribution of the single photon position in a lattice of double length. In case of the uniform lattice with its pronounced ballistic lobes in the single-site response function, this means that the photon pair is most likely separated, with the individual photons occurring as far away from each other as possible.

Figs. 6.4**(d-i)** show the numerical results for an extended state initialised in a weakly ( $\Delta = 0.51C_0$ ) and strongly ( $\Delta = 0.87C_0$ ) disordered lattice, respectively. In contrast to the classical Anderson localisation from the previous section, the spatial averaging is no longer performed by exciting several sites one after another, but from the simultaneous excitation of all  $M = 20$  sites with the entangled state. As  $M$  is yet too small to obtain smooth results and a clear picture of the general trend, an additional ensemble average with 20 independent realisations of disorder is performed in the numerical analysis.

For growing disorder, the mean photon number gets more and more concentrated around the excitation sites, due to the diminishing ballistic lobes of the single site responses (see **(d,g)**). At the same time, the correlation function changes drastically. Instead of an-

---

<sup>5</sup>Note, that in reality one cannot distinguish between  $\delta < 0$  and  $\delta > 0$ , due to photon indistinguishability. Therefore, one needs to remove one semi-axis of the function  $G_\delta$  and multiply  $G_0$  with 1/2 in order to obtain an actual probability distribution for the photon distance  $|\delta|$ .

tibunching, the photons now tend to occupy the same output channel ( $\mathbf{e}, \mathbf{h}$ ). The long on-diagonal ridge corresponds to each input waveguide being a likely localisation spot for the pair. The associated localisation peaks get more distinct for increasing strengths of disorder.

In accordance to this bunching behaviour, the inter-photon distance becomes very small ( $\mathbf{f}, \mathbf{i}$ ). In particular, its distribution  $G_\delta$  is exponentially localised around  $\delta = 0$ , with the steepness of the slope depending on  $\Delta/C_0$ . Also in case of these disordered lattices,  $G_\delta(L)$  for the extended input state has the same properties as  $\bar{n}_n(2L)$ .<sup>6</sup> Hence, the photon pair remains transversally extended, in a sense that it can occupy many possible output channels, but the two photons will always be detected together near one of the input guides. This Anderson co-localisation occurs twice as fast as the corresponding localisation of a single particle wavefunction [121].

To generate the entangled input state in an experiment, once again a type-I SPDC source is employed. In contrast to the scheme presented in chapter 4.2 (see Fig. 2.5), a collinear setup is used here. A continuous wave laser ( $\lambda_p = 404$  nm, power 80 mW) pumps a 1.5 mm thick  $\text{LiIO}_3$  crystal, cut such that collinear wave vectors are phase-matched in the degenerate case  $\lambda_s = \lambda_i = 808$  nm. Subsequently, the pump photons are removed by a polarising beam-splitter. Signal and idler photons are imaged onto the front face of the sample by a focussing lens (focal length  $f = 30$  mm). Due to the collinear geometry and the absence of any spatial filtering (such as the apertures in Fig. 2.5), the extended spatial profile of the pump beam is imprinted on the spatial distribution of the signal and idler photons<sup>7</sup>. This profile covers approximately  $M \approx 20$  waveguides at the front face of the sample. Clearly, signal and idler can be generated anywhere within the pump beam profile, but they will always be created at the same location and without transverse momentum. Hence, the two photons will always hit the sample together as a pair. This implements an approximate version of the extended path-entangled state (6.2) [127]. Of course, most pairs will not couple into a waveguide but rather scatter into the bulk. This is not a problem, however, as these photons diffract over the sample length of 4.9 cm to such an extent, that their spatial density gets negligibly small. The main approximation of Eq. (6.2) lies in the uneven spatial distribution of the photons, due to the Gaussian intensity profile of the pump beam. Therefore, the state is not sharply truncated beyond the  $M = 20$  sites and the photons are more likely to excite one of the central guides, than one of the outer channels.

<sup>6</sup>More realisations of disorder are required in the ensemble average of  $\bar{n}_n$ , as no spatial averaging arises from the input state.

<sup>7</sup>For a schematic drawing of the source, see [127]

In order to characterise the output of the arrays, the end face of the glass chip is imaged onto two planes by another lens ( $f = 40$  mm) and a non-polarising beam splitter. Hence, each photon pair leaving the sample splits with a probability of 50% onto the two image planes. In each plane, a multimode fiber is scanned across the imaged waveguide locations to collect the photons. These fibers are connected to two SPCMs, measuring the coincidence rate within a 3 ns detection window. Each combination of fiber positions  $(m, n)$  provides an estimation of one element of the coincidence probability matrix  $P_{m,n}^{(\text{ext})}$ . Thus, collecting the data for all combinations and multiplying the on-diagonal terms  $m = n$  by two, gives a measurement of the correlation function  $\Gamma_{m,n}^{(\text{ext})}$ . The expectation value of the photon number distribution  $\bar{n}_n^{(\text{ext})}$  is measured from the count rates of a single scanned fiber [127]. As before, only the central region of the waveguide lattices is excited in each case, such that the boundaries have no influence.

The measured output number distribution in the uniform lattice is presented in the blue curve of Fig. 6.5(a). It exhibits a similar shape and size as the theoretical expectation (cf. Fig. 6.4(a)). Some noteworthy differences are the larger separation of the two main peaks and an increased modulation depth of the distribution. This likely arises from a slightly larger coupling than in the classical case<sup>8</sup>, as well as the non-uniform distribution of the photons at the input.

A Gaussian intensity profile of the pump beam, will lead to a Gaussian spatial profile of the generated photon distribution behind the nonlinear crystal. Hence, a more realistic input state is given by:

$$\left| \Psi_{k_0, \sigma}^{(\text{Gauss})} \right\rangle \equiv \frac{1}{\sqrt{2\sqrt{\pi}\sigma}} \sum_{k=1}^N e^{-\frac{(k-k_0)^2}{2\sigma^2}} \left( \hat{b}_k^\dagger \right)^2 |\emptyset\rangle,$$

with  $k_0$  and  $\sigma$  as mean position and standard deviation of the Gaussian envelope, respectively. As long as the influence of the boundaries is negligible, the truncation of the Gaussian plays no significant role. A straightforward calculation shows that the envelope function also occurs in the average photon number and the correlation function, yielding:

$$\bar{n}_m^{(\text{Gauss})}(z) = \frac{2}{\sqrt{\pi}\sigma} \sum_{k=1}^N e^{-\frac{(k-k_0)^2}{\sigma^2}} |U_{m,k}(z)|^2$$

---

<sup>8</sup>Here, the wavelength is 808 nm, compared to 780 nm in the classical measurements used for the determination of the simulation parameters, amounting to larger couplings. Realistic estimates for the couplings at this wavelength are  $C_0 \approx 2 \text{ cm}^{-1}$  for the uniform lattice and  $C_0 \approx 1.7 \text{ cm}^{-1}$  for the disordered lattices.



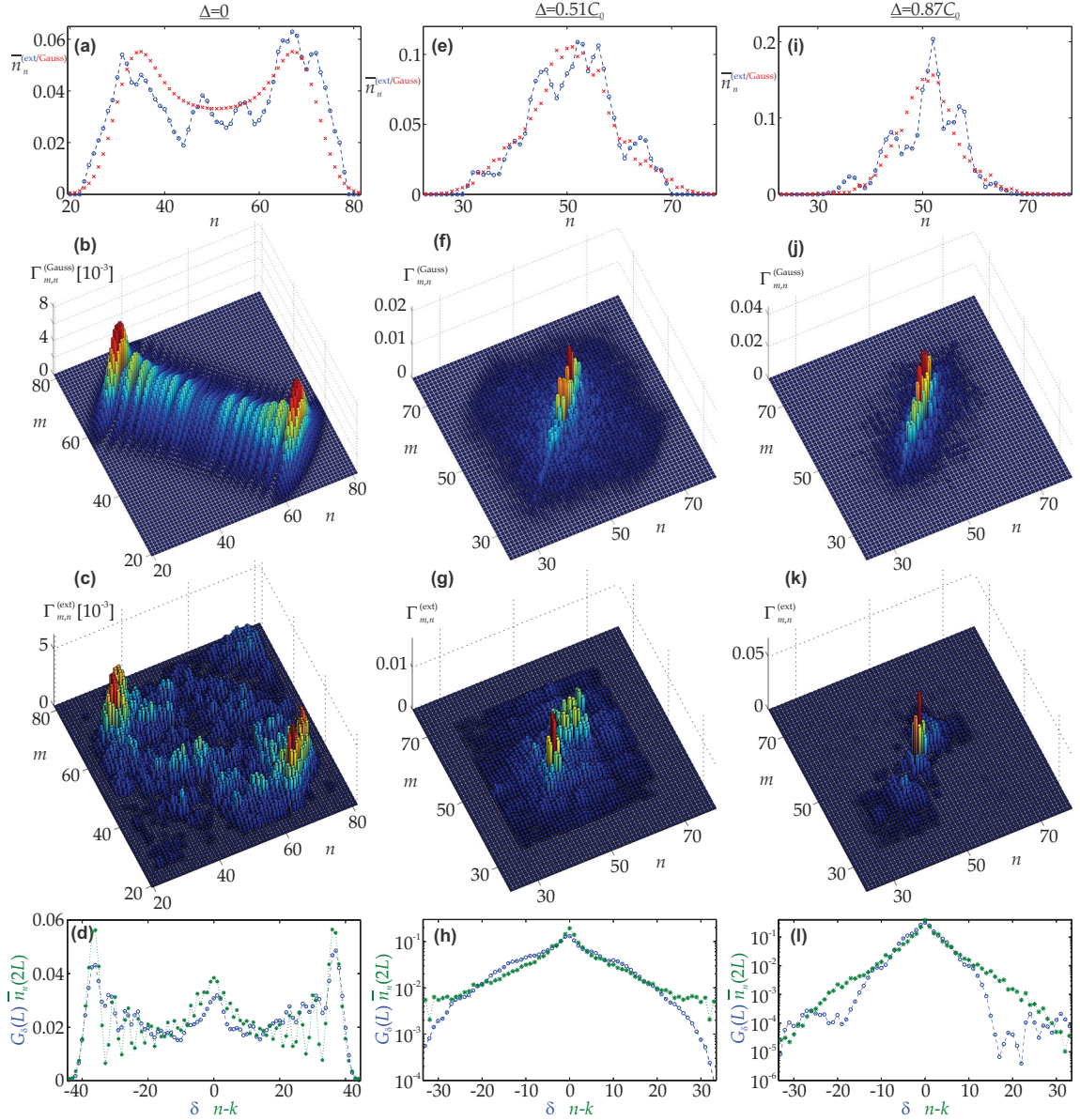


**Figure 6.5:** Observation of Anderson co-localisation. The cases of the uniform lattice with  $C_0 = 2 \text{ cm}^{-1}$  (a-d), weakly disordered (e-h) and strongly disordered lattice (i-l), both with  $C_0 = 1.7 \text{ cm}^{-1}$  are presented. Top row: Average photon number distribution at the output of the  $L = 4.9 \text{ cm}$  long lattice. The experimental data is shown in blue, the numerically calculated values for a Gaussian excitation profile with  $\sigma = 5.5$ , averaged over 20 realisations of disorder, in red. Second row: Calculated disorder-averaged correlation function for the Gaussian excitation. Third row: Measured correlation functions. Bottom row: Inter-photon distance quasi-distribution obtained from these correlation measurements (blue circles) compared to expected photon number distribution at the double distance  $2L$  (green symbols) from an ensemble average with 500 disorder realisations. In (d), the case of a very weak disorder  $\Delta = 0.15C_0$  has been considered.

and

$$\Gamma_{m,n}^{(\text{Gauss})}(z) = \frac{2}{\sqrt{\pi}\sigma} \left| \sum_{k=1}^N e^{-\frac{(k-k_0)^2}{2\sigma^2}} U_{m,k}(z) U_{n,k}(z) \right|^2.$$

The red data points in Fig. 6.5(a) show the calculated output average photon numbers for a Gaussian excitation with a width of  $\sigma = 5.5$ , which is the best fit to the experimental data. Together with the increased coupling, this retrieves the spread of the distribution as well as the inner dip. The additional modulation of the experimental curve may result from the fact that also  $|\Psi_{k_0,\sigma}^{(\text{Gauss})}\rangle$  is an approximation of the input state, as the pump beam profile may not be perfectly Gaussian, the nonlinear crystal may contain inhomogeneities and the SPDC is a spontaneous process with intrinsic noise.

The Gaussian envelope also arises along the main diagonal in the correlation function, as it can be seen in Fig. 6.5(b). In comparison to the top-hat excitation (cf. Fig. 6.4(b)) some of inner features along the main diagonal are washed out, whereas the anti-diagonal structure remains unaffected.

The Gaussian confinement due to the spatial pump beam profile is clearly visible in the measured correlation function shown in Fig. 6.5(c), as the off-diagonal ridges follow roughly a Gaussian envelope along the diagonal direction. The pattern exhibits anti-bunching of the photon pair with strong correlations in the inter-photon distance.

These correlations are most conveniently interpreted in the distance function  $G_\delta(L)$  (blue curve in (d)). The ballistic lobes of the ideal uniform lattice are visible, albeit with some reduced visibility of the minima in between. Moreover, a small peak can be seen in the inner region near  $\delta = 0$ . As discussed before, the function  $G_\delta(L)$  is expected to be equivalent to the average photon number from a single-site input to a lattice of double length. A comparison to numerical simulations of  $\bar{n}_n(2L)$  (shown in green) shows how the inner peak can be generated from a small amount of disorder: In the simulation  $\Delta = 0.15C_0$  creates a peak of comparable height, which suggests that disorder from small imprecisions of the lattice fabrication contributes to this observation. Due to the effective doubling in evolution length, the peak is more pronounced than in the classical investigation of the lattice (see the brief discussion on the limit  $z \rightarrow \infty$  in chapter 6.1). However, a quantitative analysis of the classical measurement (see Fig. 6.3(a)), reveals that the disorder can be at most  $\Delta < 0.1C_0$  (which is also a realistic constraint given the fabrication precision). Also the reduced depth of the oscillations in  $G_\delta$  is only partially explained by a mere disorder of the lattice. Another contribution to the inner peak likely arises from limitations to the visibility of the quantum path interference. This would also explain the on-diagonal peak near  $m = n = 80$  in the correlation function (Fig. 6.5(c)).

In the disordered lattices, the mean photon number distributions shown in the blue curves of Figs. 6.5(e,l) narrow considerably compared to the regular lattice, yet remaining extended over about 20 sites. The distributions are more peaked in their centres than the calculated top-hat results (cf. Figs. 6.4(d,g)). The numerical data (red points) suggests that this can at least partially be explained by a Gaussian input state profile<sup>9</sup>. The correlation functions in the disordered scenarios (f,g,j,k) exhibit no further trace of anti-bunching. Instead, they get concentrated on the main diagonal, as expected from theory and indicating the presence of Anderson co-localisation. The envelope of the correlation ridge along the main-diagonal is again constrained by the pump beam profile. Also its lateral width seems to agree well to the numerical data. The latter observation is corroborated by comparing the experimental result for  $G_\delta(L)$  with the calculated distribution  $\bar{n}_n(2L)$  (h,l). The exponential form of the localisation peak is clearly visible in both cases and the slopes match. This is a clear evidence for the observation of Anderson co-localisation in disordered waveguide lattices. Note that the fluctuations of  $G_\delta$  at the level of  $10^{-4}$  are most likely due to the absence of additional ensemble averaging in the experimental data and photon counting statistics.

These results represent an implementation of a QRW of indistinguishable bosons on a disordered lattice. They experimentally demonstrate the phenomenon of Anderson co-localisation and answer several of the initially posed questions for the extended path-entangled input state: The two bosons of the pair do not localise independently; the whole pair does not even localise at all, as it retains an extended wavefunction. Instead, the inter-particle distance is concentrated around 0, i.e., the two photons tend to occupy the same channel. Therefore, the disorder does not compromise their initial correlation. On the contrary, it helps to overcome the severe impact of transverse ballistic transport on the correlation, leading to co-localisation for sufficient amounts of disorder. This localisation in the relative distance coordinate occurs at the twofold speed as the single-particle localisation.

---

<sup>9</sup>For disordered lattices, another approximation of the input state lies in the fact, that the displacement of the waveguides is not considered in the Gaussian envelope

## 7 Conclusion and Outlook

In this thesis, photonic QRWs in lattices of evanescently coupled waveguides were investigated. Of particular interest was the quantum path interference of pairs of indistinguishable photons, which is induced by their bosonic exchange symmetry. This amounts to correlations between the possible trajectories the pair can take through the lattice. The complexity of QRWs scales exponentially with the number of participating quanta, which is of great relevance for quantum information processing applications. However, the experimental overhead grows unfavourably with the number of photons.

Therefore, the aim of this thesis was to explore alternative avenues towards QRWs with a complexity beyond the case of a pair in a uniform 1D lattice, without increasing the number of quanta. To this end, the second transverse dimension as well as a lateral variation of the lattice properties in 1D systems can be utilised. These degrees of freedom are accessible by direct waveguide writing with ultrashort laser pulses. In the course of this work, a 2D crossing of waveguide arrays, a Glauber-Fock array with a controlled variation of the coupling strength as well as a disordered lattice have been investigated as paradigmatic examples.

In order to allow a rapid and reliable estimation of the expected QRW performance in a waveguide lattice, a method for the simulation of two-photon QRWs with classical light has been developed at the beginning of this thesis. The scheme employs only two coherent light beams of fixed intensity but variable relative phase and is applicable to arbitrary lattice geometries. A sequence of random phases suffices to estimate the photon correlation function of pairs in a product state with vanishing bias for large numbers of measurements [62]. This technique has been successfully applied to a variety of waveguide lattices throughout this work and beyond [62, 96, 128]. Furthermore, a modified version of this method entailing controlled phases enables the unbiased and precise simulation of a QRW of photon pairs in a path-entangled input state [72]. In both cases, the expectation value of the two-photon coincidence rate is obtained by purely classical optics at the expense of requiring more measurement settings than in the quantum regime. The major benefit of the classical method is that it merely relies on ‘off-the-shelf’ coherent light sources and

---

a camera compared to the need for SPDC-sources and a multitude of bucket detectors in case of an actual quantum measurement. Thus, a rapid and reliable characterisation of the laser-written waveguide lattices regarding their expected performance in QRWs is possible.

As it has been demonstrated in the fourth chapter of this work, the complexity of photon pair correlations can be substantially increased compared to the scenario of uniform planar lattices by exploiting the second transverse spatial dimension. This leads to larger Hilbert spaces being occupied by the two quanta. The structure of choice has been an intersection of two 1D arrays. Via numerical calculations, the classical characterisation technique developed in this work as well as an experimental implementation of a QRW, it has been shown how the photon trajectories cover both transverse dimensions and exhibit intricate correlations [62, 88]. These correlations depend on whether the photons are injected on one or on both planes of the 2D structure. In either case, the correlation contains features of path-entanglement and independence. A crossover between 1D and 2D characteristics can be induced by tuning the likelihood of the photons to jump onto the other plane, which in turn can be controlled by the lattice properties [62].

Even if only a single transverse dimension is accessible, be it due to the fabrication technology or other constraints, the complexity of QRWs can nonetheless be increased by making use of the absolute coordinate as a degree of freedom, as was shown in chapter 5. To this end, the translational invariance of a uniform lattice has to be broken. Planar Glauber-Fock lattices with a square root increase of the coupling strength along their transverse dimension break that invariance and have been investigated in terms of their single-particle as well as their two-particle dynamics [96]. In the single-particle regime, which can be probed with classical light, these lattices act as an optical analogue of the displacement of Fock states in phase space. Such an optical simulator has been experimentally realised by a specifically engineered distribution of the inter-waveguide distance, achieving record values of displacement amplitude and Fock state order. Due to the absence of lateral translational symmetry in these lattices, QRWs of two indistinguishable particles exploit the transverse coordinate as an additional degree of freedom. As revealed by theoretical analysis and the classical characterisation technique, their correlation acts as a fingerprint of the relative separation of the input waveguides as well as their absolute position within the lattice. Conversely, information can be encoded in both parameters.

Finally, even an uncontrolled variation of the lattice properties along the transverse dimension can lead to a QRW fundamentally differing from the scenario in a uniform lattice. In this vein, disordered 1D lattices in the regime of Anderson localisation have been in-

investigated regarding their impact on the QRW of path-entangled photons. A uniform distribution of the coupling, amounting to off-diagonal disorder, has been realised, again by tuning the waveguide separation. Anderson localisation in the classical regime has been observed in these lattices by spatial averaging [125]. In the quantum domain, a photon pair in an extended entangled state has been considered, which performs spatial averaging by virtue of its intrinsic randomness. It has been demonstrated numerically and experimentally that the pair localises together while remaining spatially extended [127]. This Anderson co-localisation occurs at half the evolution length of a single particle.

These results demonstrate how the trajectories and correlations in a two-particle QRW can be controlled by tailoring the geometry of a lattice and its properties. By introducing either the lateral position in a 1D system or the second transverse dimension as degrees of freedom, the state space of the QRW can be substantially enlarged. This promises an enhanced capacity for information processing applications without increasing the number of quanta in the system. As far as bosonic QRWs are concerned, optical waveguide lattices constitute a robust platform with the direct laser inscription technique providing the required degree of control over the lattice parameters as well as the capability of a 2D fabrication.

Further research already extends or may in the future extend this work in a variety of directions:

One avenue is the experimental implementation of the classical characterisation technique for path-entangled photon pairs. The statistical simulations presented earlier in this work suggest that the phase precisions offered by spatial light modulators or piezoelectric actuators are sufficient for a very accurate and precise reconstruction of the quantum correlation [72].

Any discrete and passive linear optical system with evenly distributed losses can be described by a unitary transfer matrix. In a recent work, it could be shown that a complete characterisation of all magnitudes and phases of this unitary is possible with a series of classical interference measurements, employing a pairwise excitation of the individual channels of the system, sweeping relative phases and time-resolved intensity detection [129]. The continuous light evolution in a waveguide lattice discussed in this work represents a special case of such an optical network. Hence, that scheme can be seen as a generalisation of the method introduced in chapter 3 of this work and be employed to determine all entries of the unitary  $\mathbf{U}$ . This should be a very useful tool when it comes to analysing higher-order moments, such as correlations in multi-particle QRWs, which

---

are also governed by the unitary [130].

The theoretical framework of this thesis considered coupled waveguide systems which are either unitary or exhibit at least equal losses in all channels<sup>1</sup>. However, it has been analytically proven that the formalisms for the calculation of average photon number distributions and photon correlations carry over to arbitrary loss distributions [66]. Hence, non-unitary lattice systems can be analysed with the same methods, as long as no gain is involved. As recently demonstrated experimentally, the loss distribution in 1D laser-written waveguide lattices can be controlled independently from the real part of the refractive index by periodic curvatures and the associated bending loss [131].

The semi-infinite Glauber-Fock lattice considered in chapter 5 can be superimposed with a linear transverse index gradient, leading to the more general concept of so-called Glauber-Fock oscillator lattices. These systems support an oscillatory behaviour resembling Bloch-oscillations and exhibiting revivals in both, the single-particle as well as the two-particle regime, even for extended entangled states [132]. Such lattices have been experimentally implemented and their single-particle response has been investigated via classical light. The two independent fabrication parameters of writing velocity and waveguide separation have been used to implement the required index gradient and coupling distribution [133]. Moreover, as shown by Longhi in an independent work, a Glauber-Fock oscillator lattice superimposed with a binary superlattice<sup>2</sup>, emulates the Jaynes-Cummings model, which governs a two-level system resonantly interacting with a bosonic mode. In this analogue, the index contrast of the superlattice corresponds to the resonance frequency, the index gradient determines the detuning of the field and the coupling between the waveguides maps to the field-atom interaction strength [134].

Quite interestingly, even finite Glauber-Fock lattices have been analytically proven to exhibit almost complete revivals, again for single particle distributions as well as two-particle correlations [135].

One of the earliest devised applications of QRWs was the excitation transfer in spin chains by a specifically engineered coupling [13]. The envisioned state transfer requires a finite 1D lattice with binomial coupling distribution, enabling periodic revivals and a perfect transfer from one site to its counterpart on the other end at half that revival distance. However, as spins in solids are challenging to position and manipulate in a precise manner, such schemes have never been realised beyond very small system sizes [136]. An

---

<sup>1</sup>The non-uniform fanning losses in chapter 4 occurred only in segments of decoupled waveguides.

<sup>2</sup>An alternation between a high and a low refractive index

optical analogue, on the other hand, has been within reach, due to the more sophisticated level of control accessible in laser-written waveguide lattices. Thus, a high-fidelity transfer across a large-scale device has been successfully implemented [128]. The only difference to the initial spin context is the bosonic nature of the optical system leading to a different symmetry in two-particle correlations, which have been investigated via the classical characterisation approach introduced in chapter 3 [128]. Moreover, extended path-entangled input states are predicted to revive within a transfer distance, i.e., half of a single-particle revival distance, and to flip their correlation from perfect bunching to antibunching at every half of that distance in these lattices [137].

All QRWs considered in this work were exclusively based on the position degree of freedom. Clearly, information can also be encoded in the polarisation state of a photon, thereby increasing the number of available modes on a given spatial domain. Moreover, recent experiments have demonstrated that a QRW of polarisation-entangled photons on a lattice can produce the same dynamics as the QRW of fermions or even anyons<sup>3</sup> [50, 111]. Therefore, the combination of the polarisation and position degrees of freedom seems to be a very promising route for further investigation. Technical obstacles are, however, the birefringence of the waveguides, which will eventually lead to decoherence of a polarisation-entangled state when the temporal overlap of the polarisation components gets compromised, as well as the polarisation-dependent coupling in laser-written waveguides (see chapter 2.3). While the former issue does pose no serious problem for typical birefringences, photon wavepacket durations ( $\sim 100$  fs) and length scales ( $\sim 10$  cm), the polarisation dependent coupling can lead to rapidly diverging spatial evolution paths for the individual polarisation components which mixes the two degrees of freedom. In 1D arrangements, this problem can be overcome by a careful choice of the angle of alignment between the waveguides [50]. Whether a similar approach can be developed for 2D lattices or the coupling can be made sufficiently polarisation independent by means of the fabrication process, e.g., via beam shaping techniques [139] or waveguide writing in the heat accumulation regime [140], remains yet to be explored.

All these developments and prospects highlight that QRWs in optical waveguide lattices constitute a thriving scientific field which is just starting to reveal its full potential. The outcomes of this research may provide valuable insights into natural transport processes as well as lay the foundations for promising applications such as state transfer devices and resource-efficient quantum computation.

---

<sup>3</sup>Particles with fractional spin that interpolate between bosonic and fermionic exchange statistics [138]



# References

- [1] A. Einstein, “Über die von der molekularkinetischen Theorie der Wärme geforderte Bewegung von in ruhenden Flüssigkeiten suspendierten Teilchen,” *Ann. Physik* **322**, 549–560 (1905).
- [2] R. Brown, “A brief account of microscopical observations made in the months of June, July and August, 1827, on the particles contained in the pollen of plants; and on the general existence of active molecules in organic and inorganic bodies.” *Phil. Mag.* **4**, 161–173 (1828).
- [3] F. Bartumeus, M. G. E. da Luz, G. M. Viswanathan, and J. Catalan, “Animal search strategies: A quantitative random-walk analysis,” *Ecology* **86**, 3078–3087 (2005).
- [4] A. Ariño and S. L. Pimm, “On the nature of population extremes,” *Evolutionary Ecology* **9**, 429–443 (1995).
- [5] L. Bachelier, “Théorie de la spéculation,” Ph.D. thesis, École Normale Supérieure (1900).
- [6] B. Mandelbrot, “The variation of certain speculative prices,” *J. Bus.* **36**, 394–419 (1963).
- [7] Y. Aharonov, L. Davidovich, and N. Zagury, “Quantum random walks,” *Phys. Rev. A* **48**, 1687 (1993).
- [8] E. Farhi and S. Gutmann, “Quantum computation and decision trees,” *Phys. Rev. A* **58**, 915 (1998).
- [9] J. Kempe, “Quantum random walks - an introductory overview,” *Contemp. Phys.* **44**, 307 (2003).
- [10] O. Mülken and A. Blumen, “Spacetime structures of continuous-time quantum walks,” *Phys. Rev. E* **71**, 036128 (2005).
- [11] P. Rebentrost, M. Mohseni, I. Kassal, S. Lloyd, and A. Aspuru-Guzik, “Environment-assisted quantum transport,” *New J. Phys.* **11**, 033003 (2009).

- [12] S. Bose, “Quantum communication through an unmodulated spin chain,” *Phys. Rev. Lett.* **91**, 207901 (2003).
- [13] M. Christandl, N. Datta, A. Ekert, , and A. J. Landahl, “Perfect state transfer in quantum spin networks,” *Phys. Rev. Lett.* **92**, 187902 (2004).
- [14] A. M. Childs, “Universal computation by quantum walk,” *Phys. Rev. Lett.* **102**, 180501 (2009).
- [15] J. Du, H. Li, X. Xu, M. Shi, J. Wu, X. Zhou, and R. Han, “Experimental implementation of the quantum random-walk algorithm,” *Phys. Rev. A* **67**, 042316 (2003).
- [16] C. A. Ryan, M. Laforest, J. C. Boileau, and R. Laflamme, “Experimental implementation of a discrete-time quantum random walk on an NMR quantum-information processor,” *Phys. Rev. A* **72**, 062317 (2005).
- [17] M. Karski, L. Förster, J.-M. Choi, A. Steffen, W. Alt, D. Meschede, and A. Widera, “Quantum walk in position space with single optically trapped atoms,” *Science* **325**, 174–177 (2009).
- [18] H. Schmitz, R. Matjeschk, C. Schneider, J. Glueckert, M. Enderlein, T. Huber, and T. Schaetz, “Quantum walk of a trapped ion in phase space,” *Phys. Rev. Lett.* **103**, 090504 (2009).
- [19] F. Zähringer, G. Kirchmair, R. Gerritsma, E. Solano, R. Blatt, and C. F. Roos, “Realization of a quantum walk with one and two trapped ions,” *Phys. Rev. Lett.* **104**, 100503 (2010).
- [20] A. Schreiber, K. N. Cassemiro, V. Potoček, A. Gábris, P. J. Mosley, E. Anderson, I. Jex, and C. Silberhorn, “Photons walking the line: A quantum walk with adjustable coin operations,” *Phys. Rev. Lett.* **104**, 050502 (2010).
- [21] M. A. Broome, A. Fedrizzi, B. P. Lanyon, I. Kassal, A. Aspuru-Guzik, and A. G. White, “Discrete single-photon quantum walks with tunable decoherence,” *Phys. Rev. Lett.* **104**, 153602 (2010).
- [22] P. L. Knight, E. Roldán, and J. E. Sipe, “Quantum walk on the line as an interference phenomenon,” *Phys. Rev. A* **68**, 020301(R) (2003).
- [23] D. Bouwmeester, I. Marzoli, G. P. Karman, W. Schleich, and J. P. Woerdman, “Optical Galton board,” *Phys. Rev. A* **61**, 013410 (1999).

- 
- [24] B. Do, M. L. Stohler, S. Balasubramanian, D. S. Elliott, C. Eash, E. Fischbach, M. A. Fischbach, A. Mills, and B. Zwickl, “Experimental realization of a quantum quincunx by use of linear optical elements,” *J. Opt. Soc. Am. B* **22**, 499–504 (2005).
- [25] H. B. Perets, Y. Lahini, F. Pozzi, M. Sorel, R. Morandotti, and Y. Silberberg, “Realization of quantum walks with negligible decoherence in waveguide lattices,” *Phys. Rev. Lett.* **100**, 170506 (2008).
- [26] A. Jones, “Coupling of optical fibers and scattering in fibers,” *J. Opt. Soc. Am.* **55**, 261–271 (1965).
- [27] S. Somekh, E. Garmire, A. Yariv, H. Garvin, and R. Hunsperger, “Channel optical waveguide directional coupler,” *Appl. Phys. Lett.* **22**, 46–48 (1973).
- [28] D. N. Christodoulides, F. Lederer, and Y. Silberberg, “Discretizing light behaviour in linear and nonlinear optical waveguide lattices,” *Nature* **424**, 817–823 (2003).
- [29] F. Dreisow, M. Heinrich, A. Szameit, S. Doering, S. Nolte, A. Tuennermann, S. Fahr, and F. Lederer, “Spectral resolved dynamic localization in curved fs laser written waveguide arrays,” *Opt. Exp.* **16**, 3474–3483 (2008).
- [30] Y. Lahini, A. Avidan, F. Pozzi, M. Sorel, R. Morandotti, D. N. Christodoulides, and Y. Silberberg, “Anderson localization and nonlinearity in one-dimensional disordered photonic lattices,” *Phys. Rev. Lett.* **100**, 013906 (2008).
- [31] Y. Lahini, R. Pugatch, F. Pozzi, M. Sorel, R. Morandotti, N. Davidson, and Y. Silberberg, “Observation of a localization transition in quasiperiodic photonic lattices,” *Phys. Rev. Lett.* **103**, 013901 (2009).
- [32] R. R. Gattass and E. Mazur, “Femtosecond laser micromachining in transparent materials,” *Nature Photon.* **2**, 219–225 (2008).
- [33] A. Szameit and S. Nolte, “Discrete optics in femtosecond-laserwritten photonic structures,” *J. Phys. B: At. Mol. Opt. Phys.* **43**, 163001 (2010).
- [34] S. Liu, Y. Hu, P. Zhang, X. Gan, C. Lou, D. Song, J. Zhao, J. Xu, and Z. Chen, “Symmetry-breaking diffraction and dynamic self-trapping in optically induced hexagonal photonic lattices,” *Appl. Phys. Lett.* **100**, 061907 (2012).
- [35] B. Terhalle, A. S. Desyatnikov, D. N. Neshev, W. Krolikowski, C. Denz, and Y. S. Kivshar, “Effect of nonlinearity on dynamic diffraction and interband coupling in two-dimensional hexagonal photonic lattices,” *Phys. Rev. A* **86**, 013821 (2012).

- [36] Y. Bromberg, Y. Lahini, R. Morandotti, and Y. Silberberg, “Quantum and classical correlations in waveguide lattices,” *Phys. Rev. Lett.* **102**, 253904 (2009).
- [37] A. Peruzzo, M. Lobino, J. C. F. Matthews, N. Matsuda, A. Politi, K. Poulios, X.-Q. Zhou, Y. Lahini, N. Ismail, K. Woerhoff, Y. Bromberg, Y. Silberberg, M. G. Thompson, and J. L. O’Brien, “Quantum walks of correlated photons,” *Science* **329**, 1500 (2010).
- [38] P. P. Rohde, A. Schreiber, M. Štefaňák, I. Jex, A. Gilchrist, and C. Silberhorn, “Increasing the dimensionality of quantum walks using multiple walkers,” *J. Comp. Theor. Nanoscience* **10**, 1644–1652 (2013).
- [39] X.-C. Yao, T.-X. Wang, P. Xu, H. Lu, G.-S. Pan, X.-H. Bao, C.-Z. Peng, C.-Y. Lu, Y.-A. Chen, and J.-W. Pan, “Observation of eight-photon entanglement,” *Nature Photon.* **6**, 225–228 (2012).
- [40] S. Longhi, “Photonic bloch oscillations of correlated particles,” *Opt. Lett.* **36**, 3248–3250 (2011).
- [41] A. Schreiber, A. Gábris, P. P. Rohde, K. Laiho, M. Štefaňák, V. Potoček, C. Hamilton, I. Jex, and C. Silberhorn, “A 2D quantum walk simulation of two-particle dynamics,” *Science* **336**, 55–58 (2012).
- [42] M. Gräfe, A. S. Solntsev, R. Keil, A. A. Sukhorukov, M. Heinrich, A. Tünnermann, S. Nolte, A. Szameit, and Y. S. Kivshar, “Biphoton generation in quadratic waveguide arrays: A classical optical simulation,” *Sci. Rep.* **2**, 562 (2012).
- [43] G. D. Marshall, A. Politi, J. C. F. Matthews, P. Dekker, M. Ams, M. J. Withford, and J. L. O’Brien, “Laser written waveguide photonic quantum circuits,” *Opt. Exp.* **17**, 12546 (2009).
- [44] L. Sansoni, F. Sciarrino, G. Vallone, P. Mataloni, A. Crespi, R. Ramponi, and R. Osellame, “Polarization entangled state measurement on a chip,” *Phys. Rev. Lett.* **105**, 200503 (2010).
- [45] A. Crespi, R. Ramponi, R. Osellame, L. Sansoni, I. Bongioanni, F. Sciarrino, G. Vallone, and P. Mataloni, “Integrated photonic quantum gates for polarization qubits,” *Nat. Commun.* **2**, 566 (2011).
- [46] T. Meany, M. Delanty, S. Gross, G. D. Marshall, M. J. Steel, and M. J. Withford, “Non-classical interference in integrated 3D multiports,” *Opt. Exp.* **20**, 26895–26905 (2012).

- 
- [47] N. Spagnolo, C. Vitelli, L. Aparo, P. Mataloni, F. Sciarrino, A. Crespi, R. Ramponi, and R. Osellame, “Three-photon bosonic coalescence in an integrated tritter,” *Nat. Commun.* **4**, 1606 (2013).
- [48] M. Tillmann, B. Dakić, R. Heilmann, S. Nolte, A. Szameit, and P. Walther, “Experimental boson sampling,” *Nature Phot.* **7**, 540–544 (2013).
- [49] A. Crespi, R. Osellame, R. Ramponi, D. J. Brod, E. F. G. ao, N. Spagnolo, C. Vitelli, E. Maiorino, P. Mataloni, and F. Sciarrino, “Integrated multimode interferometers with arbitrary designs for photonic boson sampling,” *Nature Phot.* **7**, 545–549 (2013).
- [50] L. Sansoni, F. Sciarrino, G. Vallone, P. Mataloni, A. Crespi, R. Ramponi, and R. Osellame, “Two-particle bosonic-fermionic quantum walk via integrated photonics,” *Phys. Rev. Lett.* **108**, 010502 (2012).
- [51] A. Crespi, R. Osellame, R. Ramponi, V. Giovannetti, R. Fazio, L. Sansoni, F. D. Nicola, F. Sciarrino, and P. Mataloni, “Anderson localization of entangled photons in an integrated quantum walk,” *Nature Phot.* **7**, 322–328 (2013).
- [52] R. J. Glauber, “Coherent and incoherent states of the radiation field,” *Phys. Rev.* **131**, 2766 (1963).
- [53] C. C. Gerry and P. L. Knight, *Introductory Quantum Optics* (Cambridge University Press, 2005).
- [54] D. F. Walls and G. J. Milburn, *Quantum Optics* (Springer-Verlag, 2008).
- [55] H. Carmichael, “Lecture notes: Quantum optics,” University of Auckland (2007).
- [56] F. Lederer, “Vorlesungsmanuskript: Theoretische optik,” FSU Jena (2005).
- [57] V. A. Fock, “Konfigurationsraum und zweite Quantelung,” *Z. Physik* **75**, 622 (1932).
- [58] A. Einstein, “Über einen die Erzeugung und Verwandlung des Lichtes betreffenden heuristischen Gesichtspunkt,” *Ann. Physik* **322**, 132 (1905).
- [59] C. K. Hong, Z. Y. Ou, and L. Mandel, “Measurement of subpicosecond time intervals between two photons by interference,” *Phys. Rev. Lett.* **59**, 2044 (1987).
- [60] F. Bloch, “Über die Quantenmechanik der Elektronen in Kristallgittern,” *Z. Physik* **52**, 555 (1928).

- [61] L. E. Estes, T. H. Keil, and L. M. Narducci, “Quantum-mechanical description of two coupled harmonic oscillators,” *Phys. Rev.* **175**, 286 (1968).
- [62] R. Keil, A. Szameit, F. Dreisow, M. Heinrich, S. Nolte, and A. Tünnermann, “Photon correlations in two-dimensional waveguide arrays and their classical estimate,” *Phys. Rev. A* **81**, 023834 (2010).
- [63] A. Yariv, *Quantum Electronics* (John Wiley & Sons, 1989), 3rd ed.
- [64] K. Okamoto, *Fundamentals of optical waveguides* (Elsevier, 2006), 2nd ed.
- [65] A. Szameit, “Light propagation in two-dimensional waveguide arrays,” Ph.D. thesis, FSU Jena (2007).
- [66] M. Gräfe, R. Heilmann, R. Keil, T. Eichelkraut, M. Heinrich, S. Nolte, and A. Szameit, “Correlations of indistinguishable particles in non-Hermitian lattices,” *New J. Phys.* **15**, 033008 (2013).
- [67] P. Grangier, G. Roger, and A. Aspect, “Experimental evidence for a photon anti-correlation effect on a beam splitter: A new light on single-photon interferences,” *Europhys. Lett.* **1**, 173 (1986).
- [68] Z. Y. Ou, X. Y. Zou, L. J. Wang, and L. Mandel, “Experiment on nonclassical fourth-order interference,” *Phys. Rev. A* **42**, 2957 (1990).
- [69] J. C. F. Matthews, A. Politi, A. Stefanov, and J. L. O’Brien, “Manipulation of multiphoton entanglement in waveguide quantum circuits,” *Nature Phot.* **3**, 346–350 (2009).
- [70] N. D. Mermin, “Extreme quantum entanglement in a superposition of macroscopically distinct states,” *Phys. Rev. Lett.* **65**, 1838 (1990).
- [71] J. O. Owens, M. A. Broome, D. N. Biggerstaff, M. E. Goggin, A. Fedrizzi, T. Lindjorð, M. Ams, G. D. Marshall, J. Twamley, M. J. Withford, and A. G. White, “Two-photon quantum walks in an elliptical direct-write waveguide array,” *New J. Phys.* **13**, 075003 (2011).
- [72] R. Keil, F. Dreisow, M. Heinrich, A. Tünnermann, S. Nolte, and A. Szameit, “Classical characterisation of biphoton correlation in waveguide lattices,” *Phys. Rev. A* **83**, 013808 (2011).
- [73] K. Itoh, W. Watanabe, S. Nolte, and C. Schaffer, “Ultrafast processes for bulk modification of transparent materials,” *MRS Bulletin* **31**, 620–625 (2006).

- 
- [74] S. Nolte and M. Will and J. Burghoff and A. Tünnermann, “Femtosecond waveguide writing: a new avenue to three-dimensional integrated optics,” *Appl. Phys. A* **77**, 109–111 (2003).
- [75] A. Szameit, F. Dreisow, T. Pertsch, S. Nolte, and A. Tuennermann, “Control of directional evanescent coupling in fs laser written waveguides,” *Opt. Exp.* **15**, 1579–1587 (2007).
- [76] R. Bhardwaj, P. B. Corkum, D. M. Rayner, C. Hnatovsky, E. Simova, and R. S. Taylor, “Stress in femtosecond-laser-written waveguides in fused silica,” *Opt. Lett.* **29**, 1312–1314 (2004).
- [77] I. Mansour and F. Caccavale, “An improved procedure to calculate the refractive index profile from the measured near-field intensity,” *J. Lightwave Technol.* **14**, 423–428 (1996).
- [78] E. A. J. Marcatili, “Bends in optical dielectric guides,” *Bell Syst. Tech. J.* **48**, 2103–2132 (1969).
- [79] Y. Shih, “Entangled biphoton source - property and preparation,” *Rep. Prog. Phys.* **66**, 1009–1044 (2003).
- [80] M. Gräfe, “Quantum random walks in gekoppelten Wellenleitersystemen,” Master’s thesis, FSU Jena (2012).
- [81] R. H. Hadfield, “Single-photon detectors for optical quantum information applications,” *Nature Photon.* **3**, 696–705 (2009).
- [82] A. Gulinatti, I. Rech, M. Assanelli, M. Ghioni, and S. Cova, “A physically based model for evaluating the photon detection efficiency and the temporal response of SPAD detectors,” *J. Mod. Opt.* **58**, 10–20 (2011).
- [83] G. T. Reid, “Automatic fringe pattern analysis: A review,” *Opt. and Lasers in Engng.* **7**, 37–68 (1986/7).
- [84] B. Hein and G. Tanner, “Wave communication across regular lattices,” *Phys. Rev. Lett.* **103**, 260501 (2009).
- [85] T. Kitagawa, M. S. Rudner, E. Berg, and E. Demler, “Exploring topological phases with quantum walks,” *Phys. Rev. A* **82**, 033429 (2010).
- [86] M. B. Plenio and S. F. Huelga, “Dephasing-assisted transport: quantum networks and biomolecules,” *New J. Phys.* **10**, 113019 (2008).

- [87] L. A. Fernandes, J. R. Grenier, P. R. Herman, J. S. Aitchison, and P. V. S. Marques, “Stress induced birefringence tuning in femtosecond laser fabricated waveguides in fused silica,” *Opt. Exp.* **20**, 24103–24114 (2012).
- [88] K. Poullos, R. Keil, D. Fry, J. D. A. Meinecke, J. C. F. Matthews, A. Politi, M. Gräfe, M. Heinrich, S. Nolte, A. Szameit, and J. L. O’Brien, “Quantum walks of correlated photon pairs in two-dimensional waveguide arrays,” arXiv:1308.2554v1 [quant-ph] (2013).
- [89] A. Peruzzo, A. Laing, A. Politi, T. Rudolph, and J. L. O’Brien, “Multimode quantum interference of photons in multiport integrated devices,” *Nat. Commun.* **2**, 224 (2011).
- [90] K. Mattle, M. Michler, H. Weinfurter, A. Zeilinger, and M. Zukowski, “Non-classical statistics at multiport beam splitters,” *Appl. Phys. B* **60**, S111–S117 (1995).
- [91] A. Politi, J. C. F. Matthews, M. Thompson, and J. O’Brien, “Integrated quantum photonics,” *Selected Topics in Quantum Electronics, IEEE Journal of* **15**, 1673–1684 (2009).
- [92] W. H. Press, S. A. Teukolsky, W. T. Vetterling, and B. P. Flannery, *Numerical Recipes in C* (Cambridge University Press, 1992), 2nd ed.
- [93] Y. Bromberg, Y. Lahini, and Y. Silberberg, “Bloch oscillations of path-entangled photons,” *Phys. Rev. Lett.* **105**, 263604 (2010).
- [94] Y. Lahini, Y. Bromberg, D. N. Christodoulides, and Y. Silberberg, “Quantum correlations in two-particle Anderson localization,” *Phys. Rev. Lett.* **105**, 163905 (2010).
- [95] A. Perez-Leija, H. Moya-Cessa, A. Szameit, and D. N. Christodoulides, “Glauber-Fock photonic lattices,” *Opt. Lett.* **35**, 2409 (2010).
- [96] R. Keil, A. Perez-Leija, F. Dreisow, M. Heinrich, H. Moya-Cessa, S. Nolte, D. N. Christodoulides, and A. Szameit, “Classical analogue of displaced Fock states and quantum correlations in Glauber-Fock photonic lattices,” *Phys. Rev. Lett.* **107**, 103601 (2011).
- [97] M. Boiteux and A. Levelut, “Semicohherent states,” *J. Phys. A* **6**, 589 (1973).
- [98] F. A. M. deOliveira, M. S. Kim, P. L. Knight, and V. Buzek, “Properties of displaced number states,” *Phys. Rev. A* **41**, 2645 (1990).



- 
- [99] A. I. Lvovsky and S. A. Babichev, “Synthesis and tomographic characterization of the displaced Fock state of light,” *Phys. Rev. A* **66**, 011801 (2002).
- [100] F. Ziesel, T. Ruster, A. Walther, H. Kaufmann, K. Singer, F. Schmidt-Kaler, and U. G. Poschinger, “Experimental creation and analysis of displaced number states,” *J. Phys. B: At. Mol. Opt. Phys.* **46**, 104008 (2013).
- [101] L. G. Lutterbach and L. Davidovich, “Method for direct measurement of the Wigner function in cavity QED and ion traps,” *Phys. Rev. Lett.* **78**, 2547 (1997).
- [102] K. Banaszek and K. Wodkiewicz, “Testing quantum nonlocality in phase space,” *Phys. Rev. Lett.* **82**, 2009 (1999).
- [103] K. Banaszek, C. Radzewicz, K. Wodkiewicz, and J. S. Krasinski, “Direct measurement of the Wigner function by photon counting,” *Phys. Rev. A* **60**, 674 (1999).
- [104] P. Bertet, A. Auffeves, P. Maioli, S. Osnaghi, T. Meunier, M. Brune, J. M. Raimond, and S. Haroche, “Direct measurement of the Wigner function of a one-photon Fock state in a cavity,” *Phys. Rev. Lett.* **89**, 200402 (2002).
- [105] D. Leibfried, D. M. Meekhof, B. E. King, C. Monroe, W. M. Itano, and D. J. Wineland, “Experimental determination of the motional quantum state of a trapped atom,” *Phys. Rev. Lett.* **77**, 4281 (1996).
- [106] P. Alsing, D.-S. Guo, and H. J. Carmichael, “Dynamic Stark effect for the Jaynes-Cummings system,” *Phys. Rev. A* **45**, 5135 (1992).
- [107] S. A. Podoshvedov and J. Kim, “Dense coding by means of the displaced photon,” *Phys. Rev. A* **77**, 032319 (2008).
- [108] J. Franck, “Elementary processes of photochemical reactions,” *Trans. Faraday Soc.* **21**, 536–542 (1926).
- [109] E. Condon, “A theory of intensity distribution in band systems,” *Phys. Rev.* **28**, 1182–1201 (1926).
- [110] J. W. Fleischer, T. Carmon, M. Segev, N. K. Efremidis, and D. N. Christodoulides, “Observation of discrete solitons in optically induced real time waveguide arrays,” *Phys. Rev. Lett.* **90**, 023902 (2003).
- [111] J. C. F. Matthews, K. Poullos, J. D. A. Meinecke, A. Politi, A. Peruzzo, N. Ismail, K. Wörhoff, M. G. Thompson, and J. L. O’Brien, “Observing fermionic statistics with photons in arbitrary processes,” *Sci. Rep.* **3**, 1539 (2013).

- [112] I. Bloch, J. Dalibard, and W. Zwerger, “Many-body physics with ultracold gases,” *Rev. Mod. Phys.* **80**, 885 (2008).
- [113] J. W. Negele and H. Orland, *Quantum Many-Particle Systems* (Westview Press, 1998).
- [114] P. W. Anderson, “Absence of diffusion in certain random lattices,” *Phys. Rev.* **109**, 1492–1505 (1958).
- [115] D. S. Wiersma, P. Bartolini, A. Lagendijk, and R. Righini, “Localization of light in a disordered medium,” *Nature* **390**, 671–673 (1997).
- [116] H. D. Raedt, A. Lagendijk, and P. de Vries, “Transverse localization of light,” *Phys. Rev. Lett.* **62**, 47–50 (1989).
- [117] S. Longhi, “Quantum-optical analogies using photonic structures,” *Laser & Photon. Rev.* **3**, 243 (2009).
- [118] T. Pertsch, U. Peschel, S. Nolte, A. Tünnermann, F. Lederer, J. Kobelke, K. Schuster, and H. Bartelt, “Nonlinearity and disorder in two-dimensional fiber arrays,” *Phys. Rev. Lett.* **93**, 053901 (2004).
- [119] T. Schwartz, G. Bartal, S. Fishman, and M. Segev, “Transport and Anderson localization in disordered two-dimensional photonic lattices,” *Nature* **446**, 52–55 (2007).
- [120] M. Segev, Y. Silberberg, and D. N. Christodoulides, “Anderson localization of light,” *Nature Phot.* **7**, 197–204 (2013).
- [121] A. F. Abouraddy, G. D. Giuseppe, D. N. Christodoulides, and B. E. A. Saleh, “Anderson localization and colocalization of spatially entangled photons,” *Phys. Rev. A* **86**, 040302(R) (2012).
- [122] Y. Lahini, Y. Bromberg, Y. Shechtman, A. Szameit, D. N. Christodoulides, R. Morandotti, and Y. Silberberg, “Hanbury Brown and Twiss correlations of Anderson localized waves,” *Phys. Rev. A* **84**, 041806(R) (2011).
- [123] R. Keil, Y. Lahini, Y. Shechtman, M. Heinrich, R. Pugatch, F. Dreisow, A. Tünnermann, S. Nolte, and A. Szameit, “Perfect imaging through a disordered waveguide lattice,” *Opt. Lett.* **37**, 809–811 (2012).
- [124] A. Szameit, Y. V. Kartashov, P. Zeil, F. Dreisow, M. Heinrich, R. Keil, S. Nolte, A. Tünnermann, V. A. Vysloukh, and L. Torner, “Wave localization at the boundary of disordered photonic lattices,” *Opt. Lett.* **35**, 1172–1174 (2010).

- 
- [125] L. Martin, G. D. Giuseppe, A. Perez-Leija, R. Keil, F. Dreisow, M. Heinrich, S. Nolte, A. Szameit, A. F. Abouraddy, D. N. Christodoulides, and B. E. A. Saleh, “Anderson localization in optical waveguide arrays with off-diagonal coupling disorder,” *Opt. Exp.* **19**, 13636 (2011).
- [126] B. Kramer and A. MacKinnon, “Localization: Theory and experiment,” *Rep. Prog. Phys.* **56**, 1469–1564 (1993).
- [127] G. D. Giuseppe, L. Martin, A. Perez-Leija, R. Keil, F. Dreisow, S. Nolte, A. Szameit, A. F. Abouraddy, D. N. Christodoulides, and B. E. A. Saleh, “Einstein-Podolsky-Rosen spatial entanglement in ordered and Anderson photonic lattices,” *Phys. Rev. Lett.* **110**, 150503 (2013).
- [128] A. Perez-Leija, R. Keil, A. Kay, H. Moya-Cessa, S. Nolte, L.-C. Kwek, B. M. Rodríguez-Lara, A. Szameit, and D. N. Christodoulides, “Coherent quantum transport in photonic lattices,” *Phys. Rev. A* **87**, 012309 (2013).
- [129] S. Rahimi-Keshari, M. A. Broome, R. Fickler, A. Fedrizzi, T. C. Ralph, and A. G. White, “Direct characterization of linear-optical networks,” *Opt. Express* **21**, 13450–13458 (2013).
- [130] K. Mayer, M. C. Tichy, F. Mintert, T. Konrad, and A. Buchleitner, “Counting statistics of many-particle quantum walks,” *Phys. Rev. A* **83**, 062307 (2011).
- [131] T. Eichelkraut, R. Heilmann, S. Stützer, F. Dreisow, D. N. Christodoulides, S. Nolte, and A. Szameit, “Mobility transition from ballistic to diffusive transport in non-Hermitian lattices,” *Nat. Commun.* **4**, 2533 (2013).
- [132] A. Perez-Leija, R. Keil, A. Szameit, A. F. Abouraddy, H. Moya-Cessa, and D. N. Christodoulides, “Tailoring the correlation and anticorrelation behavior of path-entangled photons in Glauber-Fock oscillator lattices,” *Phys. Rev. A* **85**, 013848 (2012).
- [133] R. Keil, A. Perez-Leija, P. Aleahmad, H. Moya-Cessa, S. Nolte, D. N. Christodoulides, and A. Szameit, “Observation of Bloch-like revivals in semi-infinite Glauber-Fock photonic lattices,” *Opt. Lett.* **37**, 3801–3803 (2012).
- [134] S. Longhi, “Jaynes-Cummings photonic superlattices,” *Opt. Lett.* **36**, 3407–3409 (2011).
- [135] B. M. Rodríguez-Lara, “Exact dynamics of finite Glauber-Fock photonic lattices,” *Phys. Rev. A* **84**, 053845 (2011).

- [136] J. Zhang, G. L. Long, W. Zhang, Z. Deng, W. Liu, and Z. Lu, “Simulation of Heisenberg xy interactions and realization of a perfect state transfer in spin chains using liquid nuclear magnetic resonance,” *Phys. Rev. A* **72**, 012331 (2005).
- [137] A. Perez-Leija, R. Keil, H. Moya-Cessa, A. Szameit, and D. N. Christodoulides, “Perfect transfer of path-entangled photons in  $J_x$  photonic lattices,” *Phys. Rev. A* **87**, 022303 (2013).
- [138] F. Wilczek, “Quantum mechanics of fractional-spin particles,” *Phys. Rev. Lett.* **49**, 957–959 (1982).
- [139] R. Osellame, S. Taccheo, M. Marangoni, R. Ramponi, P. Laporta, D. Polli, S. De Silvestri, and G. Cerullo, “Femtosecond writing of active optical waveguides with astigmatically shaped beams,” *J. Opt. Soc. Am. B* **20**, 1559–1567 (2003).
- [140] S. M. Eaton, H. Zhang, M. L. Ng, J. Li, W.-J. Chen, S. Ho, and P. R. Herman, “Transition from thermal diffusion to heat accumulation in high repetition rate femtosecond laser writing of buried optical waveguides,” *Opt. Express* **16**, 9443–9458 (2008).
- [141] Y. Bromberg and Y. Lahini, “The calculation of the classical intensity correlation,” Private communication.

# A Appendix

## A.1 Derivation of the intensity correlation

This section is devoted to the derivation of the modulated classical intensity correlation (3.10) from its definition (3.9) and the phases (3.8). It will be shown that this function is equivalent to the third term of eq. (3.7), allowing it to be used for the classical emulation of the quantum interference of path-entangled photon pairs.

With the known intensity evolution for two-waveguide excitation (3.3) one obtains from the definition (3.9):

$$\Gamma_{m,n}^{(\text{int},\phi)} = \frac{1}{4} \sum_{j=0}^3 (-1)^j |U_{m,k} + U_{m,l} e^{i\Phi_j}|^2 (m \leftrightarrow n),$$

where  $(m \leftrightarrow n)$  means that the same term as written before is repeated, but the indices  $m$  and  $n$  are exchanged. The phase of the entangled state  $\phi$  is contained in the phases between the classical beams  $\Phi_j$ , as defined in (3.8). Separating  $\phi$  from  $\Phi_j$  yields

$$4\Gamma_{m,n}^{(\text{int},\phi)} = \sum_{j=0}^3 (-1)^j \left[ |U_{m,k}|^2 + |U_{m,l}|^2 + \left( U_{m,k} U_{m,l}^* e^{i\frac{\phi}{2}} e^{-ij\frac{\pi}{2}} + \text{c.c.} \right) \right] (m \leftrightarrow n),$$

which can be reordered to

$$\begin{aligned} 4\Gamma_{m,n}^{(\text{int},\phi)} &= \sum_{j=0}^3 (-1)^j \underbrace{\left( |U_{m,k}|^2 + |U_{m,l}|^2 \right)}_{\equiv F_j^{(1)}} (m \leftrightarrow n) \\ &+ \sum_{j=0}^3 (-1)^j \underbrace{\left[ \left( |U_{m,k}|^2 + |U_{m,l}|^2 \right) \left( U_{n,k} U_{n,l}^* e^{i\frac{\phi}{2}} e^{-ij\frac{\pi}{2}} + \text{c.c.} \right) \right]}_{\equiv F_j^{(2)}} + (m \leftrightarrow n) \\ &+ \sum_{j=0}^3 (-1)^j \underbrace{\left( U_{m,k} U_{m,l}^* e^{i\frac{\phi}{2}} e^{-ij\frac{\pi}{2}} + \text{c.c.} \right)}_{\equiv F_j^{(3)}} (m \leftrightarrow n). \end{aligned} \quad (\text{A.1})$$

Clearly, the first terms  $F^{(1)}$  do not depend on  $j$ , hence this sum vanishes

$$\sum_{j=0}^3 (-1)^j F^{(1)} = 0.$$

Moreover, as each of the terms  $F_j^{(2)}$  contains a phase factor  $e^{-ij\frac{\pi}{2}}$ , one finds  $F_0^{(2)} + F_2^{(2)} = F_1^{(2)} + F_3^{(2)} = 0$ , such that also these terms do not contribute to the overall sum

$$\sum_{j=0}^3 (-1)^j F_j^{(2)} = F_0^{(2)} - F_1^{(2)} + F_2^{(2)} - F_3^{(2)} = 0.$$

Finally, in the terms  $F_j^{(3)}$ , the phase factor  $e^{-ij\frac{\pi}{2}}$  occurs twice, such that  $F_0^{(3)} = F_2^{(3)}$  and  $F_1^{(3)} = F_3^{(3)}$ , which yields

$$\sum_{j=0}^3 (-1)^j F_j^{(3)} = 2F_0^{(3)} - 2F_1^{(3)}.$$

With this, the expression (A.1) simplifies to

$$\begin{aligned} \Gamma_{m,n}^{(\text{int},\phi)} &= \frac{1}{2} \left[ \left( U_{m,k} U_{m,l}^* e^{i\frac{\phi}{2}} + \text{c.c.} \right) (m \leftrightarrow n) - \left( -i U_{m,k} U_{m,l}^* e^{i\frac{\phi}{2}} + \text{c.c.} \right) (m \leftrightarrow n) \right] \\ &= \frac{1}{2} \left[ \left( U_{m,k} U_{m,l}^* e^{i\frac{\phi}{2}} + \text{c.c.} \right) (m \leftrightarrow n) + \left( U_{m,k} U_{m,l}^* e^{i\frac{\phi}{2}} - \text{c.c.} \right) (m \leftrightarrow n) \right] \\ &= U_{m,k} U_{n,k} U_{m,l}^* U_{n,l}^* e^{i\phi} + \text{c.c.}, \end{aligned}$$

which is the result (3.10).

## A.2 Inequality for distinguishable photons

In this brief addendum, the inequality (4.1) relating on- and off-diagonal elements of the coincidence probability matrix of distinguishable photons will be derived. Moreover, a calculation for the statistical uncertainty of violations of this inequality will be provided. The correlation function of a distinguishable photon pair, propagating in a waveguide lattice after injection into guides  $k$  and  $l$  reads [71]:

$$\Gamma_{m,n}^{(\text{d})} = |U_{m,k} U_{n,l}|^2 + |U_{m,l} U_{n,k}|^2. \quad (\text{A.2})$$

The interpretation for the coincidence probability  $P_{m,n}^{(\text{d})} = \frac{1}{1+\delta_{m,n}} \Gamma_{m,n}^{(\text{d})}$  is quite obvious: The photon from  $k$  can go to  $m$  and the photon from  $l$  to  $n$  or vice versa. These probabilities add incoherently. In other words, the two photons evolve independently from each other

and there is no interference whatsoever.

The aim is to give a lower bound for the off-diagonal elements with respect to the on-diagonal terms. Such a bound can be obtained analogously to the derivation of a similar bound on classical intensity correlations [36, 141]. Here one expands

$$(\Gamma_{m,n}^{(d)})^2 = (|U_{m,k}U_{n,l}|^2 + |U_{m,l}U_{n,k}|^2)^2 = \underbrace{|U_{m,k}U_{n,l}|^4 + |U_{m,l}U_{n,k}|^4}_{\geq 2|U_{m,k}U_{n,l}U_{m,l}U_{n,k}|^2} + 2|U_{m,k}U_{n,l}U_{m,l}U_{n,k}|^2.$$

The lower bound on the first two terms can be conjectured directly from the binomial expansion of  $(|U_{m,k}U_{n,l}|^2 - |U_{m,l}U_{n,k}|^2)^2 \geq 0$ . With this, one obtains

$$(\Gamma_{m,n}^{(d)})^2 \geq 4|U_{m,k}U_{m,l}|^2|U_{n,k}U_{n,l}|^2 = \Gamma_{m,m}^{(d)}\Gamma_{n,n}^{(d)},$$

which turns into

$$\sqrt{\Gamma_{m,m}^{(d)}\Gamma_{n,n}^{(d)}} - \Gamma_{m,n}^{(d)} \leq 0,$$

after taking the square root of both sides. Hence, the coincidence probabilities must obey

$$2\sqrt{P_{m,m}^{(d)}P_{n,n}^{(d)}} - (1 + \delta_{m,n})P_{m,n}^{(d)} \leq 0,$$

which is trivially satisfied for  $m = n$  and exactly the inequality (4.1) for  $m \neq n$ .

In order to decide whether this inequality is significantly violated by a given count distribution  $\mathcal{N}_{m,n}$  one has to compare the left hand side of the inequality<sup>1</sup>  $\Delta_{m,n} \equiv 2\sqrt{\mathcal{N}_{m,m}\mathcal{N}_{n,n}} - \mathcal{N}_{m,n}$  with the uncertainty arising from the Poissonian counting statistics. The counts in each pair of channels obey a Poissonian distribution with mean  $\mathcal{N}_{m,n}$  and standard deviation  $\sqrt{\mathcal{N}_{m,n}}$  [54]. To simplify the calculation of the uncertainty propagation, one can approximate the Poissonians by Gaussian distributions. This is a reasonable approximation, as the typical count numbers are in the order of  $10^4$ . Then, the total uncertainty is

$$\begin{aligned} \sigma_{m,n} &\approx \sqrt{\left(\frac{\partial\Delta_{m,n}}{\partial\mathcal{N}_{m,m}}\sqrt{\mathcal{N}_{m,m}}\right)^2 + \left(\frac{\partial\Delta_{m,n}}{\partial\mathcal{N}_{n,n}}\sqrt{\mathcal{N}_{n,n}}\right)^2 + \left(\frac{\partial\Delta_{m,n}}{\partial\mathcal{N}_{m,n}}\sqrt{\mathcal{N}_{m,n}}\right)^2} \\ &= \sqrt{\mathcal{N}_{m,m} + \mathcal{N}_{n,n} + \mathcal{N}_{m,n}}. \end{aligned}$$

This is the standard deviation facilitated in the calculation of Figs. 4.7(c) and (f) in chapter 4.2.2.

---

<sup>1</sup>Clearly, a violation is only possible for  $m \neq n$ .

# Acknowledgements

I would like to express my sincere gratitude towards the people whose support throughout the last few years has made this work possible.

First and foremost there is my mentor and advisor Prof. Dr. Alexander Szameit. His enormous input of ideas, his encouraging feedback on my own ideas and his research spirit have helped me going to the very edge of scientific knowledge and - hopefully - also a bit beyond.

I am deeply indebted to my supervisor Prof. Dr. Stefan Nolte who has offered me good guidance as well as a highly productive environment for research in his group. His critical and pointed questions were always a big help in refining my ideas and their presentations.

I am very grateful to the people with whom I had the opportunity to cooperate on the various aspects of this work. In particular, I would like to name Dr. Armando Perez-Leija and Prof. Dr. Demetrios Christodoulides who are the smart theorists behind the Glauber-Fock lattices and who have worked with me on the disordered lattices as well as a number of other projects in planar waveguide arrays.

Then there are Konstantinos Poullos and Jasmin Meinecke who cooperated with me on the experimental implementation of the 2D quantum walk together with their colleagues from the group around Prof. Dr. Jeremy O'Brien. The fruitful discussions with them have thoroughly deepened my understanding of integrated photonic quantum walks.

Thanks goes also to Dr. Giovanni Di Giuseppe and Lane Martin for doing a meticulous job on the characterisation of the disordered lattices.

My long-term office mates Dr. Felix Dreisow and Dr. Matthias Heinrich deserve a big thank you for numerous fruitful discussions, their great lab expertise and countless joyful hours at work.

I feel obliged to express my gratitude towards my former students Markus Gräfe and Stefan Weimann who gave me the opportunity to pass on what I have learned and supported me on various tasks. Markus has developed into a knowledgeable expert of quantum random walks himself who is now extending the research field in new and exciting directions. Together with our colleague René Heilmann, whose unmatched inventiveness improved our work in the lab in many ways, he has also brought the SPDC setup to life.



Furthermore I would like to thank all my other colleagues from the Ultrafast Optics group for their permanent support, be it of scientific or morale-boosting kind.

I am also grateful to the Abbe School of Photonics for providing me with a formidable stipend which allowed to me to pursue my work without monetary concerns. Szilvia Mammel and Dr. Dorit Schmidt deserve my gratitude as they always took good and rapid care of my administrative enquiries.

Special thanks goes to Christiane Otto, for always finding a good solution even for the most impractical of my glass cutting requests, as well as to Bodo Martin and Dr. Holger Hartung for providing some extra computational power when I needed it.

I'm very indebted to my friends and family who have permanently given me great support and joyful times which has always helped to free my mind and gain new motivation.

Last and most importantly, I'm deeply grateful to my parents for caring for me all the time from the very beginning to this point, just like parents do.

# Zusammenfassung

Das Ziel dieser Arbeit bestand in der Untersuchung des Verhaltens von quantenmechanischen Zufallsbewegungen, sog. *quantum random walks* (*QRWs*), in Systemen aus transversal gekoppelten optischen Wellenleitern. Von besonderem Interesse sind hierbei *QRWs* mehrerer ununterscheidbarer Photonen. Die durch deren Austauschsymmetrie hervorgerufene Quanteninterferenz führt zu einer gegenseitigen Korrelation der Photonenpfade im System. Es zeigt sich, dass die Komplexität eines *QRW* exponentiell mit der Zahl der beteiligten Photonen zunimmt, was für Anwendungen in der Quanteninformationsverarbeitung von großer Wichtigkeit ist. Allerdings steigt auch der experimentelle Aufwand der Erzeugung von Mehrphotonenzuständen erheblich mit der Quantenzahl an.

Daher galt es in dieser Arbeit Wege aufzuzeigen, wie die Komplexität gegenüber *QRWs* in homogenen, eindimensionalen (1D) Arrays, gesteigert werden kann ohne die Anzahl der beteiligten Quanten zu erhöhen. Dies kann einerseits durch Inhomogenität erfolgen oder die zweite räumlich-transversale Dimension kann ausgenutzt werden. Beide Ansätze wurden im Rahmen dieser Arbeit verfolgt. Zu diesem Zweck wurden ein zweidimensionales (2D) Gitter, ein geordnetes spezielles 1D Array, sowie ein ungeordnetes planares Array konzipiert und mittels Femtosekundenlaserschreibtechnik in Glas realisiert.

Um eine schnelle und zuverlässige Charakterisierung der Wellenleitersysteme hinsichtlich der zu erwartenden *QRWs* von Photonenpaaren zu ermöglichen, wurde ein Verfahren entwickelt, das lediglich die Interferenz klassischen Lichts benötigt. Diese Methode wurde implementiert und ihre Wirksamkeit experimentell nachgewiesen. Ein weiterführendes Verfahren, das auch die Untersuchung pfadverschränkter Eingangszustände ermöglicht, wurde entworfen und vorgestellt.

Der Einfluss der Wellenleiteranordnung auf die Pfadkorrelation zweier Photonen wurde für alle Arraytypen numerisch und experimentell untersucht, einerseits mittels des klassischen Verfahrens, andererseits durch direkte Umsetzung von *QRWs*.

Die Korrelation im 2D System zeigt sowohl Charakteristika von Pfadverschränkung als auch von Unabhängigkeit der Photonen, wobei eine gezielte Modifikation des Gitters genutzt werden kann die Balance zwischen diesen Verhaltensweisen einzustellen. Im geordneten 1D Array ergibt sich eine deutliche Abhängigkeit des Ausgangszustandes von der Eingangsposition. Außerdem werden sowohl bosonische als auch fermionische Korrelationsmerkmale beobachtet, d.h. koaguliertes Auftreten der Photonen bzw. effektive Abstößung durch das Pauli-Prinzip. Im ungeordneten Fall wurde die Anderson Lokalisierung des Abstandes eines räumlich ausgedehnten verschränkten Photonenpaares nachgewiesen. Die beobachteten Korrelationen verfügen über keine Entsprechung in homogenen 1D Anordnungen und es zeigt sich eine deutliche Steigerung der Komplexität des *QRW*.

# Ehrenwörtliche Erklärung

Ich erkläre hiermit ehrenwörtlich, dass ich die vorliegende Arbeit selbständig, ohne unzulässige Hilfe Dritter und ohne Benutzung anderer als der angegebenen Hilfsmittel und Literatur angefertigt habe. Die aus anderen Quellen direkt oder indirekt übernommenen Daten und Konzepte sind unter Angabe der Quellen gekennzeichnet.

Bei der Auswahl und Auswertung des folgenden Materials haben mir die nachstehend aufgeführten Personen in der jeweils beschriebenen Weise unentgeltlich geholfen:

1. Die Messungen der Photonen-Koinzidenzen in Kapitel 4.2.2 (Daten zu Figs. 4.6 und 4.7) wurden von Konstantinos Poullos, University of Bristol, durchgeführt.
2. Die numerische Bestimmung der Parameter in Fig. 4.9(a) wurde von Jasmin Meinecke, University of Bristol, vorgenommen.
3. Die experimentellen Daten zu Figs. 6.3 und 6.5 wurden von Dr. Giovanni Di Giuseppe und Lane Martin, CREOL, gewonnen.

Weitere Personen waren an der inhaltlich-materiellen Erstellung der vorliegenden Arbeit nicht beteiligt. Insbesondere habe ich hierfür nicht die entgeltliche Hilfe von Vermittlungs- bzw. Beratungsdiensten (Promotionsberater oder anderen Personen) in Anspruch genommen. Niemand hat von mir unmittelbar oder mittelbar geldwerte Leistungen für Arbeiten erhalten, die im Zusammenhang mit dem Inhalt der vorgelegten Dissertation stehen.

Teile dieser Arbeit wurden aus Prioritätsgründen bereits veröffentlicht oder zur Veröffentlichung eingereicht [62, 72, 88, 96, 125, 127].

Die Arbeit wurde bisher weder im In- noch im Ausland in gleicher oder ähnlicher Form einer anderen Prüfungsbehörde vorgelegt.

Die geltende Promotionsordnung der Physikalisch-Astronomischen Fakultät ist mir bekannt.

Ich versichere ehrenwörtlich, dass ich nach bestem Wissen die reine Wahrheit gesagt und nichts verschwiegen habe.

Jena, den 1. November 2013

Robert Keil

# Lebenslauf

## Persönliche Daten

|                    |                  |
|--------------------|------------------|
| Name               | Robert Keil      |
| Geburtsdatum, -ort | 25.07.1984, Jena |

## Ausbildung

|                   |  |
|-------------------|--|
| 06/2003           | Abitur am Carl-Zeiss-Gymnasium Jena, mathematisch -naturwissenschaftlicher Spezialschulteil                  |
| 10/2003 – 07/2009 | Studium der Physik an der FSU Jena   |
| 02/2007 – 02/2008 | Auslandsstudium an der University of Auckland, Neuseeland; Abschluss mit dem postgraduate Diploma in Science |
| 07/2009           | Abschluss des Jenaer Physikstudiums mit dem Diplom   |

## Wissenschaftlicher Werdegang

|                   |   |
|-------------------|---|
| 09/2005 – 10/2005 | Forschungspraktikum bei der Carl-Zeiss Jena GmbH                  |
| 03/2006 – 01/2007 | Studentische Forschungsaufgaben an der FSU Jena und dem IPHT Jena |
| 06/2008 – 06/2009 | Diplomarbeit am Institut für Angewandte Physik                    |
| 11/2009 – 09/2013 | Promotion am Institut für Angewandte Physik                       |

Robert Keil